Effects of Moisture Variations on Snow Processes and Characteristics Inferred from S^{2}noCliME Observations

by

Sarah J. Phillips

A thesis submitted in partial fulfillment of
the requirements for the degree of

Master of Science
(Atmospheric and Oceanic Sciences)

at the
University of Wisconsin-Madison
2026

Abstract

Snowfall drives snowpack variability, a vital source of water and economic activity for midlatitude mountain communities. In mountainous regions, the multi-scale processes driving the amount, spatial distribution, and characteristics of snowfall remain not well understood. Through the duration of the 2024-2025 winter season, the NSF-funded field campaign *Snow Sensitivity to Clouds in a Mountain Environment* (S^{2}noCliME) was conducted in Steamboat Springs, Colorado, with the goal of improving our understanding of the causes of snowfall variability near complex terrain. Using observations from S^{2}noCliME, the influence of moisture on snow microphysical processes and characteristics is assessed through a comparison of two cases (IOPs 3 and 4) with different patterns of large-scale moisture transport (IVT). Particular focus is paid to the local influence of moisture availability in the context of flow near the mountains.

While snow-producing clouds in the low-IVT case ("IOP4") were often shallower, and resulted in substantially lower accumulations, both cases featured times of deep and intense snow production – particularly along the mountain slopes. Low-level flow direction preferential for orographic enhancement in the region may have contributed to these signatures. However, substantial variability in snow growth processes, and their spatial and temporal distribution, was observed between and within flow regimes during both cases. The observed variability included different avenues of supercooled liquid water production to support riming as well as the presence of distinct precipitation patterns. Some of the noted variability was tied to moisture distribution and subtle variations in local flow direction. Future work will include consideration of additional environmental parameters such as instability and wind speed as well as the incorporation of additional S^2noCliME datasets. Ultimately, these results emphasize the range of local factors influencing cold-season microphysical processes in the mountains with implications for further analysis of S^2noCliME data.

Acknowledgements

I am deeply grateful to all the wonderful professors, peers, and friends who have supported me through my time at UW-Madison. Most importantly, I want to thank my advisor, Dr. Angela Rowe, for providing me with this dream opportunity and for her incredible support, guidance, and humor. Her intelligence and unyielding passion for the science, and for her students, is truly inspirational and has shaped me into a better student and researcher than I thought possible. I would also like to thank my committee members, Marian Mateling, Dr. Andrea Lopez Lang, and Dr. Tristan L'Ecuyer for their invaluable insight and advice throughout my journey here.

In addition, I would like to thank everyone in the Rowe lab, past and present – Sam, Giselle, Ben, Ian, Anthony, Becca, Tyler, Night – for letting me look up to you and for being so welcoming. I am also incredibly thankful to my friends outside the 9th floor: Katie, Leo, Prem, and Matt most especially, for getting me through that first year in AOS, and for sticking with me since.

I furtherly grateful to all of those I have met outside of the AOS department, especially Astrid, Ally, and Annika for helping to make Madison home.

Of course, I would like to thank my friends from afar as well, especially Bella, Kate, and Tal, for visiting me here and never being more than a letter or phone call away. I am furtherly grateful to my family: my father, my mother, my brothers, my sister-in-law, Terry, Mackenzie, Rebecca, and Virginia for their seemingly endless love and support.

Lastly, I want to thank everyone involved in the S^{2}noCliME field campaign. It was a dream to be able to spend time in the field, and I feel truly honored to have been a part of such an incredible project.

This research is supported by the National Science Foundation (AGS-2348451).

Contents

Acronyms

AGL Above Ground Level

AMSL Above Mean Sea Level

CIP Cloud Imaging Probe

DWR Dual-Wavelength Ratio

ECMWF European Centre for Medium-Range Weather Forecasts

ERA5 ECMWF Reanalysis v5

IOP Intensive Observing Period

IVT Integrated Vapor Transport

LWP Liquid Water Path

MRR Micro Rain Radar

MWR Microwave Radiometer

NOAA National Oceanic and Atmospheric Administration

PIP Precipitation Imaging Probe

PPI Plan Position Indicator

RHI Range Height Indicator

S^{2}noCliME Snow Sensitivity to Clouds in a Mountain Environment

SGS Sleeping Giant School

SLW Supercooled Liquid Water

SPL Storm Peak Laboratory

SRTM Shuttle Radar Topography Mission

SWE Snow Water Equivalent

WBF Wegener-Bergeron-Findeisen process

WRF Weather Research and Forecasting Model

List of Figures

List of Tables

Chapter 1

Introduction

1.1 Motivation

Snow is an important resource for midlatitude mountain communities worldwide. Mountain snowpack drives tourist economies (Parthum and Christensen 2022) and is, crucially, an essential source of water (Serreze et al. 1999; Barros 2013; Li et al. 2017). Snowpack variability can be attributed to trends in both precipitation and temperature (Mote et al. 2005; Hamlet et al. 2005). At high elevations, it is primarily precipitation that drives changes in snowpack and snow water equivalent (SWE) (Scalzitti et al. 2016). Therefore, variations in snowfall can have important implications for snowpack and, consequently, water availability. Furthermore, winters with little snowfall, such as this past winter season, raise concerns about the vitality of mountain town economies (Hill 2026).

1.2 Snow Microphysics in a Mountainous Environment

The microphysical processes involved in the creation and growth of frozen hydrometeors within a cloud ultimately determine the rate, extent, and physical characteristics of snowfall at the surface. Understanding ice crystal properties is a critical part of modeling orographic precipitation and anticipating changes in snowpack (Sterzinger and Igel 2021; Korolev et al. 2017). These properties can change throughout the lifetime of falling snow, with remaining uncertainties in our understanding of multi-scale controls on that variability and challenges in direct measurements of the varying snowfall properties all contributing to difficulty in producing accurate weather and climate forecasts (Sterzinger and Igel 2021; Korolev et al. 2017; Lundquist et al. 2019; Morrison et al. 2020). Snow grows primarily through vapor deposition, aggregation, and riming at temperatures below 0 °C. Each route of snow growth influences hydrometeor shape and density, as well as their resulting fall speeds and water content (Mason et al. 2018; Matrosov et al. 2020).

Growth through vapor deposition occurs when water vapor deposes directly onto ice crystals. Crystals growing by vapor deposition do so preferentially towards high vapor density gradients, which are greatest at their more pointed edges. Therefore, these crystals tend to be of flat (e.g., tabular/plates, branched/dendrites) or elongated (e.g., needles, columns) shapes. Observed ice hydrometeor aspect ratios tend to be lower at temperatures warmer than -20 °C, particularly at temperatures between -17 and -15 °C, which suggests that these temperatures are favorable for depositional growth (Matrosov et al. 2020). Moreover, vapor deposition requires an environment which is supersaturated with respect to ice ($e > e_i$), with ice crystal shape, or *habit,* increasing in complexity with increasing supersaturation (Hueholt et al. 2022; Bailey and Hallet 2004). As noted in Figure 1.1, different combinations of temperature and supersaturation favor growth of distinct crystal habits through vapor deposition.

Particularly efficient growth by vapor deposition can occur through the Wegener-Bergeron-Findeisen process (WBF). The WBF is rapid vapor deposition at the expense of supercooled liquid water (SLW) drops (Wegener 1911; Bergeron 1935;

Findeisen 1938). The WBF occurs when the environment is supersaturated with respect to ice but not to water ($e_s > e > e_i$), and is maximized around -15 °C (Korolev 2007). The temperature in which the WBF is maximized is also that in which dendritic growth occurs (e.g., branched crystals in Fig. 1.1). Dendrites tend to fall horizontally, amplifying wind resistance, and have low densities overall, which can result in relatively slow falling precipitation.

Snow growth through vapor deposition can also influence growth by aggregation, where frozen hydrometeors interlock or stick together to create larger particles. The shapes and densities of aggregates, and their fall speeds, depend on the habit and characteristics of individual crystals which are determined through vapor deposition (Karrer et al. 2020). In addition, greater presence and size of dendrites can increase the rate of growth by aggregation (Schrom et al. 2015). In general, aggregate size increases as temperatures warm nearer to 0 °C, with aggregation efficiency reaching a maximum around -15 °C where the growth of branched crystals is also maximized (Brandes et al. 2008; Connolly et al. 2012). Aggregate aspect ratios tend to be lower, resulting in faster fall speeds than dendrites. However, the densities of aggregates are variable.

Riming occurs when SLW accretes directly onto ice crystals or aggregates. As a result, riming substantially increases the density, and thus fall speeds, of these hydrometeors (Brandes et al. 2008; Mason et al. 2018; Matrosov et al. 2020). In precipitating orographic clouds, riming contributes to a substantial portion of SWE (Borys et al. 2003). Furthermore, observations have indicated that precipitation rates are higher when riming is a contributor to snow growth, and there may be a correlation between rime fraction and precipitation accumulation (Borys et al. 2003; Moisseev et al. 2017). The creation and maintenance of SLW to support riming requires updrafts. In addition, riming becomes more prevalent with warmer temperatures – particularly around -7 °C – which corresponds to observations of increasing snow particle fall speeds with decreasing altitude that have been attributed to riming (Brandes et al. 2008; Mason et al. 2018; Kneifel and Moisseev 2020).

Vapor deposition, riming, and aggregation can all occur within a single storm, including at a single time so long as a widespread precipitating cloud extends through the conditions where each different growth process is favored to occur. The moisture available to support the different snow growth processes can be tied to large-scale moisture transport. Transport mechanisms include atmospheric rivers, narrow regions of enhanced water vapor transport, which can result in enhanced precipitation even in inland regions of the U.S. (Rutz et al. 2014; Mateling et al. 2021). However, local factors, such as terrain, influence the formation of and supersaturations within clouds as a result of the moisture transport, which ultimately determine the microphysical processes and precipitation characteristics.

Substantial moisture availability can manifest as widespread, or *stratiform*, snowfall where deposition, and often aggregation, take place. In orographic clouds, ice crystals accumulate the majority of their mass in the lower levels of the cloud through vapor deposition and riming (Lowenthal et al. 2016). As mentioned, riming requires additional upward motion to support the growth and maintenance of SLW, which can be provided by processes related to topography (Houze 2012). *Orographic lift*, the rising of air once it is blocked by a terrain barrier, as depicted in Figure 1.2, is a source of upward motion to support the SLW that can enhance snow growth through riming (Houze 2012). Additionally, weak upward motion resulting from low-level upslope flow can enhance stratiform precipitation through aggregation and vapor deposition in the case of strong, unblocked flow (Schrom et al. 2015). Enhanced snow growth through riming and aggregation is also associated with shear layers (Fig. 1.3) owing to air blocked by terrain (Houze 2012).

In general, the modification of precipitating systems due to topography is dependent on local atmospheric conditions and features of the terrain. Static stability influences whether incoming flow is blocked or lifted when it reaches a topographic barrier, as illustrated in Figure 1.3 (Houze 2012), and enhanced precipitation near terrain has been observed to be particularly prevalent during periods of neutral stability as well as high integrated vapor transport (IVT) (McMurdie et al. 2018). Orographic lift also tends to be maximized when incoming low-level flow is strong and oriented preferentially cross-barrier relative to terrain (Saleeby et al. 2007; Houze 2012; DeLaFrance et al. 2021; McMurdie et al. 2018). Furthermore, the height of terrain influences which side of the slopes maximum orographically-enhanced precipitation occurs: with taller slopes resulting in greater windward enhancement, and shorter slopes resulting in greater enhancement on the lee side (Houze 2012).

More specific patterns of precipitation enhancement can occur as a result of flow interactions with a local terrain barrier. For one, the orographic lift resulting from low-level blocking by terrain can support formation and maintenance of a low-level "feeder" cloud containing SLW (Ramelli et al. 2021). Snow growth through riming can be enhanced through the *seeder-feeder* process when pristine crystals from a "seeder" cloud located at a higher altitude, and which may be associated with generating cells, fall into the "feeder" cloud below (Ramelli et al. 2021). Generating cells are structures near cloud top often containing pockets of SLW that can aid in precipitation generation or growth (Kumjian et al. 2014; Han et al. 2025). Generating cells are a ubiquitous feature of winter storms in orographic environments, which are associated with atmospheric instability and have been linked to vertical windshear (Kumjian et al. 2014; Tessendorf et al. 2024).

With the complex relationships between airflow, moisture, terrain, and snow microphysical processes, there are multiple, varying controls on snow growth in a mountainous environment. Our current understanding of these snowfall processes is limited by the differing terrain profiles and different atmospheric environments encompassing them, as well as challenges in observing said processes (Lundquist et al. 2019; Morrison et al 2020). Uncertainties remain in the ultimate connection from moisture transport, to moisture availability, to resulting snow growth processes – including uncertain modifications due to topography, across all scales (Sterzinger and Ignel 2021). For one, some studies have suggested that there is not necessarily a clear correlation between enhanced precipitation and upward motion due to terrain forcing (e.g., Kingsmill et al. 2015). Furthermore, there are uncertainties regarding the formation and maintenance of clouds containing SLW, including uncertainties in and controls on the ratio of liquid and ice essential for the different snow growth processes (Korolev et al. 2017). To investigate and improve our understanding of the factors and processes linked to snowfall in regions of complex topography, further observations are necessary. Because snow microphysical processes occur aloft and in-cloud, observations from remote sensing instrumentation are particularly valuable towards this goal.

1.3 Remote Sensing

Weather radar is a useful remote sensing tool for furthering our understanding of these many microphysical processes influenced by orography. Radar reflectivity (Z) is dependent, in part, on the dielectric constant of a target, which is greater for liquid water than for ice. Furthermore, radar reflectivity is directly dependent on the number of particles (N(D)) in a radar volume and the sixth power of their diameters (D), and can be expressed as:

$$Z = \sum_{Volume} D_i^6 = \int N(D) D^6 \, dD \tag{1.1}$$

Since radar reflectivity is dependent on the composition, concentration, and size of particles in a radar volume, further information is necessary to constrain the ambiguities in the characteristics of snow particles that are associated with the different avenues of snow growth. What will be referred to as "reflectivity" or "Z" from this point forward is the logarithmic value in units of decibels. Dual-polarization radar, where horizontally and vertically oriented waves are transmitted and received, is used to infer bulk microphysical characteristics and potential processes occurring within a cloud by providing information about the shapes, sizes, and concentration of hydrometeors making up a radar volume. For example, differential reflectivity (Z_{DR}) is the ratio of horizontally (Z_h) and vertically (Z_v) received power that provides additional information about the shapes of hydrometeors in a radar volume and is expressed as:

$$Z_{DR}\ (dB) = 10 \log_{10}\left(\frac{Z_h}{Z_v}\right) \tag{1.2}$$

Additional dual-polarization variables include the co-polar correlation coefficient (ρ_{HV}); the correlation between the horizontally and vertically polarized signals, indicating similarity of hydrometeors in the volume. Specific differential phase (K_{DP}) is a derived dual-polarization variable that describes the change in phase shift between the horizontal and vertical pulses. Changes in K_{DP} can indicate changes in the size and concentration of hydrometeors.

Radar reflectivity values in the context of snow tend to be less than 45 dBZ (Straka et al. 2000). A radar volume dominated by pristine crystals growing through vapor deposition is associated with reflectivity values between 5 and 30 dBZ in conjunction with Z_{DR} values in the range of 0.4 to 3.0 dB (Straka et al. 2000; Thompson et al. 2014). In a radar volume dominated by pristine dendrites, Z_{DR} has been observed to reach higher values, nearing 6 dB – often when Z_h falls between -10 and 10 dBZ (Schrom et al. 2015; Matrosov et al. 2020). An active region of dendritic growth can be inferred through Z_{DR} enhancements within a region of favorable temperatures (e.g., ~-15 °C), as well as local K_{DP} enhancements (Oue et al. 2021; Schrom et al. 2015; Matrosov et al. 2020; Kennedy and Rutledge 2011).

As particles in a radar volume aggregate, Z_{DR} values decrease to near-zero while Z_h increases substantially – generally to values greater than 20 dBZ (Thompson et al. 2014; Kumjian et al. 2022; Matrosov et al. 2020). The presence of aggregation can thus be inferred when enhanced Z_h occurs at temperatures slightly warmer than those associated with dendritic growth and just below a region of enhanced Z_{DR} (DeLaFrance et al. 2021). In the warmer temperatures, "wet" aggregates, aggregates with higher water content, result in particularly high Z_h values of 30 to 45 dBZ (Straka et al. 2000). Z_{DR} signatures associated with aggregation can depend on the stage of aggregation, with early aggregates being more oblate and conducive to Z_{DR} values greater than 0 dB (Moisseev et al. 2015). K_{DP} values associated with aggregates are very low (Thompson et al. 2014).

Like with aggregation, riming tends to increase Z_h and decrease Z_{DR} in a radar volume (Matrosov et al. 2020; Kumjian et al. 2022). However, Z_h may increase to a lesser extent than in the case of aggregation because the size of particles tends to change less dramatically through riming (Kumjian et al. 2022). Z_{DR} can also increase with riming: particularly in the case of rime on aggregates, where initial shape may not change but there is an increase in size and/or water content, or in an early stage of riming (Moisseev et al. 2017; Oue et al. 2021). Ultimately, though, ambiguities remain in interpreting snow growth and characteristics from dual-polarization radar signatures. Differentiating between aggregates and rimed particles is particularly ambiguous as both are associated with Z_h greater than 20 dBZ and Z_{DR} near 0 dB, and can occur concurrently. Interpreting dual-polarization signatures from radar volumes mixed with aggregated and pristine crystals can also be deceptive due to the values' D^6 dependency (Straka et al. 2000).

Since riming requires SLW, and generally results in denser, faster falling particles than unrimed aggregates, the noted ambiguities from observations using scanning radar can be diminished with instrumentation measuring SLW or fall speeds. For one, liquid water path (LWP) retrieved from a microwave radiometer (MWR) can be used as a proxy for riming to distinguish between snow composed of unrimed aggregates, rimed aggregates, and graupel (Mason et al. 2018). High LWP has been attributed to riming: LWP in unrimed snow is generally < 0.1 kg/m^3, but is between 0.1 and 0.3 kg/m^3 in cases of rimed snow, and greater than 0.3 kg/m^3 for heavily rimed snow (Kneifel et al. 2015; Mason et al. 2018). Secondly, fall speeds can be estimated through velocity measurements ($|V_R|$) from a vertically pointing radar. Increasing $|V_R|$ towards the surface indicate hydrometeors accumulating ice water content, which can distinguish growth by riming or vapor deposition from aggregation (Schrom and Kumjian 2016). Utilizing multiple wavelengths of radar can help to diminish ambiguity even further by exploiting the variant scattering of differently sized particles at different wavelengths of radar. As expressed in Figure 1.4, dual-frequency analysis can help to provide more concrete information about particle concentration, density, and ice water content (Grasmick et al. 2022; Matrosov et al. 2019; Oue et al. 2021). Dual-wavelength ratio (DWR) represents the difference in reflectivity at two wavelengths, relying on the smaller wavelength to begin to deviate from

Rayleigh scattering such that increasing DWRs specifically indicate increasing mean particle size in a volume (von Terzi et al. 2022).

Much of the knowledge supporting microphysical inferences from remote sensing observations has been gained through scattering simulations or by verifying inferences with in-situ data. Aircraft-based studies have been instrumental toward this effort of verifying inferences with in-situ data (e.g., that in Schrom et al. 2015, DeLaFrance et al. 2021), but they are limited in samples and have known issues in collecting fully accurate in-situ measurements. A larger sample size than feasible in an airborne study, as viewed in particular by multi-frequency radar in a region with frequent snowfall, could capture greater variability and strengthen microphysical inferences from remote sensing observations.

1.4 S²noCliME

The NSF-funded *Snow Sensitivity to Clouds in a Mountain Environment* (S²noCliME) field campaign aims to further our understanding of the processes impacting snowfall variability in mountainous regions with a rich combination of remote and in-situ observations from over an entire winter season. S²noCliME was conducted from December 2024 to April 2025 in the Park Range of Colorado (Fig. 1.5), with in-situ measurements based around Storm Peak Laboratory (SPL); a mountaintop research facility at 3220 m above mean sea level (AMSL).

In the Rocky Mountains of Colorado, snowpack is a primary source of water, but the complex topography makes for difficulty in forecasting for and observing snowfall (Rudisill et al. 2024; Bytheway et al. 2024). Numerous previous field efforts aiming to improve our understanding of cold-season precipitation processes near mountainous terrain were coastal (e.g., Cordeira et al. 2017, McMurdie et al. 2018, Cann and White 2021), while Colorado is inland and thus far from a moisture source. Past inland campaigns, including the *Surface Atmosphere Integrated Field Laboratory* (SAIL), *Study of Precipitation, the Lower Atmosphere and Surface for Hydrometeorology* (SPLASH), and *Sublimation of Snow* (SOS) campaigns in Colorado (Feldman et al. 2023, Boer et al. 2023, Lundquist et al. 2024), either lacked detailed in-situ measurements or utilized airborne instrumentation which limited observations of the variability which is necessary to fully understand the causes of, and constraints on, the different microphysical processes (Morrison et al. 2020; Rudisill et al. 2024). S^{2}no-CliME captured season-long variability, including long term stationary in-situ measurements from SPL which is often in-cloud during precipitation events (Borys and Wetzel 1997). SPL is located within Steamboat Springs Ski Resort, which sees around 289” of snow per year on average, the snowmelt of which feeds into the local Yampa Valley River which connects to the greater Colorado River System (Steamboat Ski and Resort Corp. 2025; Mastin et al. 2011).

SPL is at a particularly unique location because of the ubiquitous presence of liquid clouds, which occur around 90% of the time during precipitation or when SPL is in-cloud, and the terrain’s generally perpendicular orientation to the largely westerly incoming winds (Borys and Wetzel 1997). These conditions make the lab ideal for studying the influence of orographic lift and the presence of SLW on snowfall. As such, IFRACS (*Isotopic Fractionation in Snow*) and StormVEx (*Storm Peak Lab*

Cloud Property Validation Experiment) are previous campaigns out of SPL in which some analysis was focused on the presence and impact, including on riming processes, of SLW at SPL (Lowenthal et al. 2016; Lowenthal et al. 2019). S^{2}noCliME improves on such snowfall-focused past campaigns out of SPL by incorporating sufficient radar coverage and appropriate frequencies, including enabling dual-frequency analysis, for studying snowfall processes.

1.5 Research Goal

Moisture is important in supporting different microphysical processes, and mountainous terrain can modify precipitating systems within the context of this moisture, particularly through enhanced SLW and riming. While these characteristics have been previously observed at SPL, this study aims to better understand the influence of the flow and magnitude of moisture on snow characteristics and processes within this inland mountain region using observations from S^{2}noCliME.

Since the enhancement of snowfall due to orographic lift has been observed to be greatest during periods of cross-barrier flow, this study hypothesizes that subtle variations in flow direction may hold particular influence over the impact of local terrain features on how available moisture translates to snowfall in the region around SPL and Steamboat Springs. Two S^{2}noCliME *intensive observing periods* (IOPs), each associated with different local wind regimes and magnitudes of moisture transport, will be compared to address the following:

a. To what extent does the total magnitude of moisture determine snow characteristics?

b. How does the varying direction of local flow influence the impact of moisture on snow growth processes, particularly near a local terrain barrier?

The selected IOPs are *IOP3,* which occurred from 2000 UTC 10 January 2025 through 0000 UTC 12 January 2025, and *IOP4*, which occurred from 2000 UTC 17 January 2025 through 0000 UTC 19 January 2025. For continuity and clarity in analysis, only the initial portion of each IOP where some precipitating cloud near the terrain barrier is continuously observed, with no breaks greater than a half hour, is included in this study. The precipitation of interest associated with IOP3 spanned the 11th and 12th of January 2025 (UTC). The precipitation of interest associated with IOP4 spanned the 17th and 18th of January 2025 (UTC). The specific times of analysis for each IOP are:

- **IOP3**: 0330 UTC 11 January 2025 through 0900 UTC 12 January 2025
- **IOP4**: 1830 UTC 17 January 2025 through 0830 UTC 18 January 2025

The following chapter will discuss the data sources and methods used in this analysis to assess the impact of moisture magnitude and flow variation on snowfall processes observed during these events. Chapter 3 will provide an overview of the two cases, including specific differences in the large-scale evolution, local moisture availability, local winds, and snowfall accumulations associated with each IOP. Chapter 4 will note the results, with focus on those which are flow-dependent. Chapter 5 will discuss results in the context of literature as well as provide additional considerations. Chapter 6 will include a summary of this analysis and point towards avenues for future work.

1.6 Figures

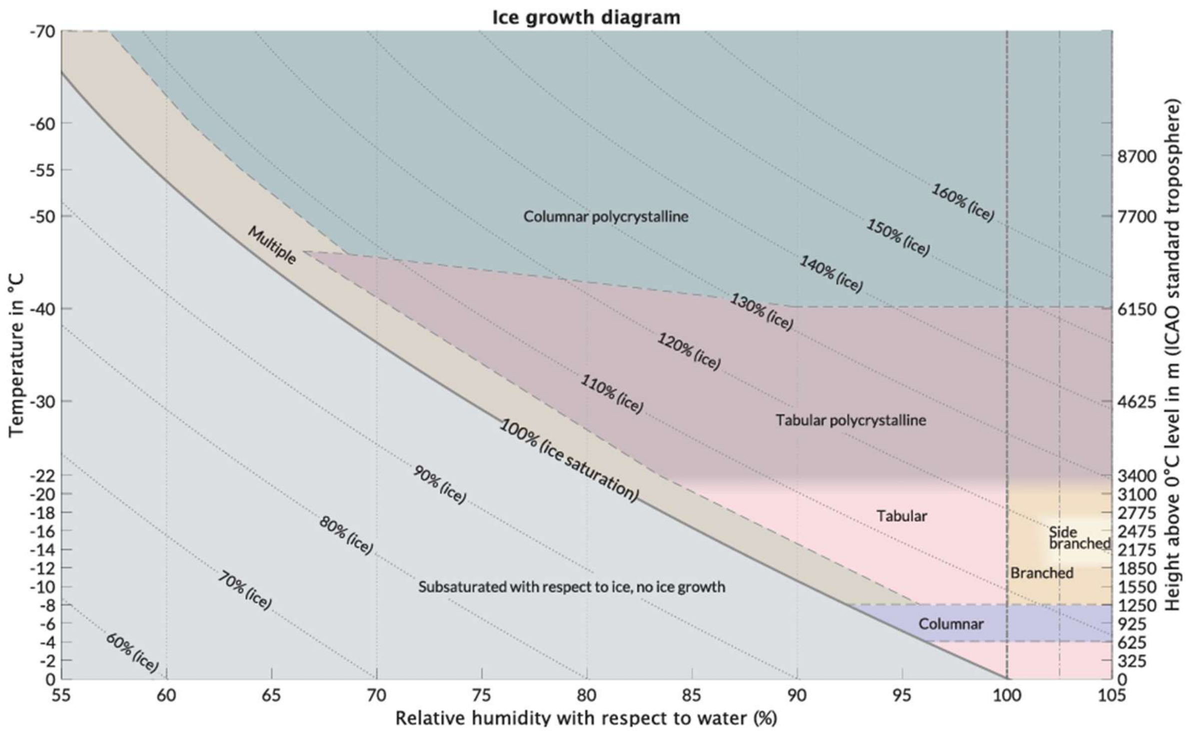

Figure 1.1: Ice growth habit diagram as related to relative humidity with respect to water (%) and temperature (°C), with contours of relative humidity with respect to ice (%) overlaid. Blurred lines depict zones of transition between ice growth forms. Dashed lines indicate uncertain boundary between ice growth forms conditions. From Hueholt et al. (2022).

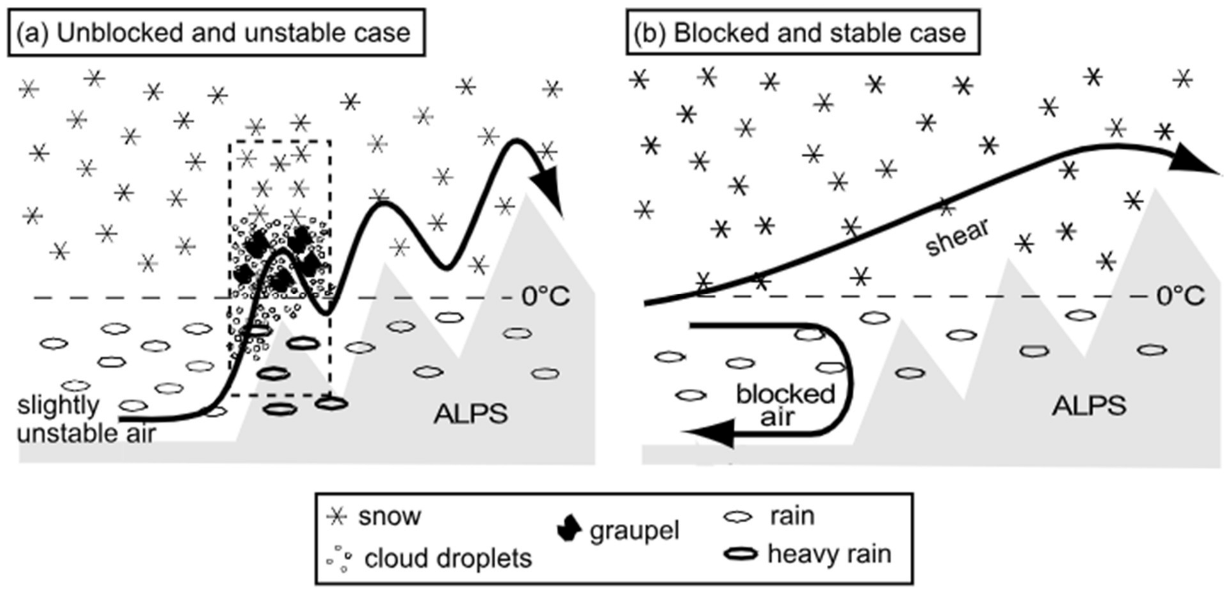

Figure 1.2: Conceptual representation of orographic precipitation mechanisms owing to the terrain impact on airflow of (a) unblocked and unstable low-level flow and (b) stable and blocked low-level flow. Processes and conditions above dashed line are within temperatures below 0 °C. From Houze (2012), adapted from Medina and Houze (2003).

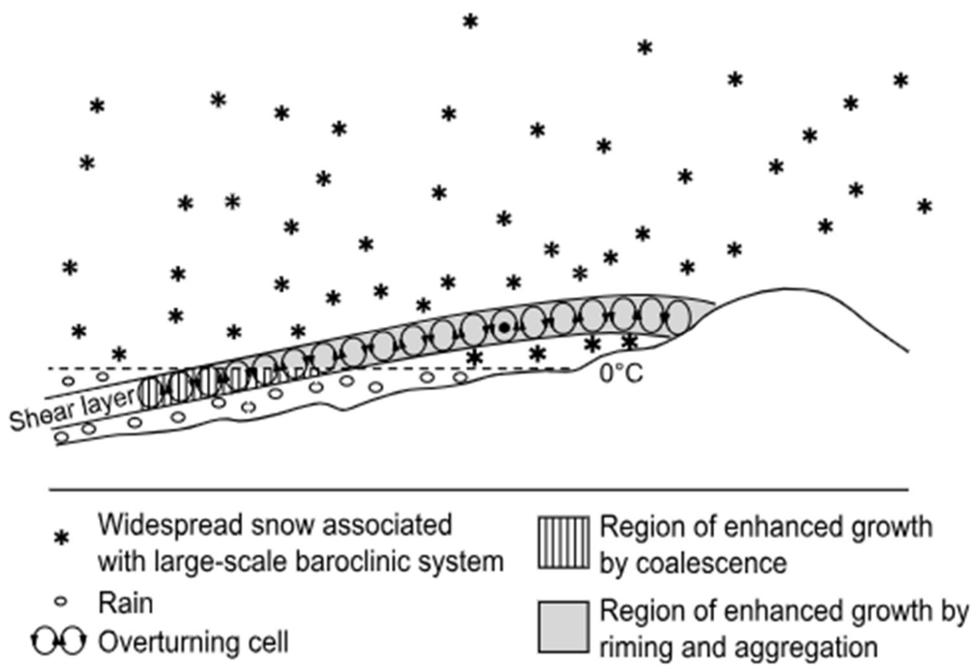

Figure 1.3: Conceptual representation of mechanisms resulting in orographic enhancement of precipitation (snowfall above dashed line) during stably stratified conditions. From Houze and Medina (2005).

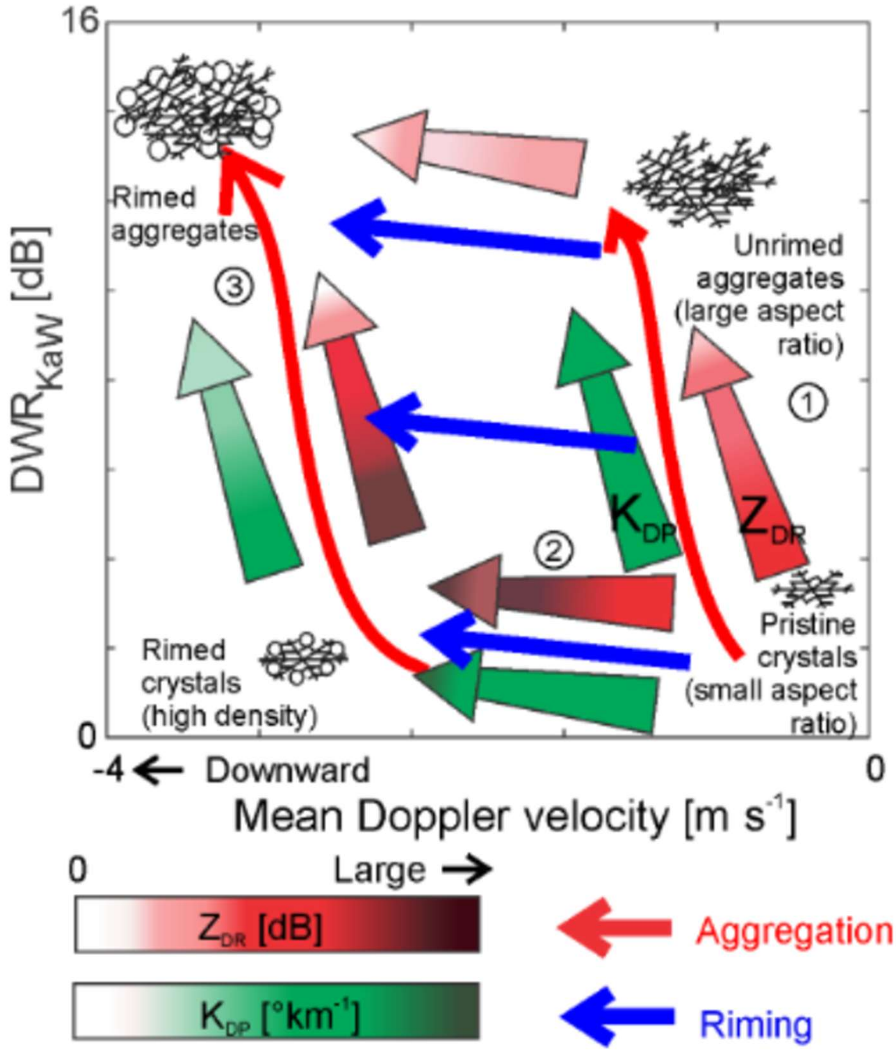

Figure 1.4: A schematic of DWR and mean doppler velocity changes with Z_{DR} and K_{DP} depicting how the corresponding changes in the polarimetric variables connect to inferences in riming and aggregation for the observations analyzed in Oue et al. (2021). From Oue et al. (2021).

Figure 1.5: Map of the continental United States depicting the geographic location of Steamboat Springs and SPL, and nearby topography. From Hallar et al. (2025).

Chapter 2

Data and Methods

2.1 S^{2}noCliME Datasets

2.1.1 Instrumentation Overview

A wide array of remote and in-situ instruments were deployed during S^{2}no-CliME to create a comprehensive dataset that captured, and enables the study of, snowfall variability. There were three main sites in which S^{2}noCliME instruments were hosted: SPL on the top of Mt. Werner (at 40.455 °N, -106.744 °W, and 3220 m AMSL), the mid-mountain site located about halfway down the mountain (at 40.461 °N, -106.762 °W, and at 2756.6 m AMSL), and the Sleeping Giant School (SGS) site in the adjacent valley (at 40.506 °N, -106.902 °W, and around 2020 m AMSL).

S^{2}noCliME deployed dual-polarization radars of different wavelengths: Stony Brook University's KASPR Ka-band (35.29 GHz) radar at SGS and Colorado State University's SEA-POL C-band (5.6 GHz) radar near the Yampa Valley Regional airport – about 40 km west of SPL (40.470 °N, -107.199 °W, and 2032 m AMSL). Both radars scanned toward SPL to enable dual-frequency analysis. In addition to long-term trace gas, aerosol, and surface measurements, SPL hosted in-situ microphysical instrumentation for S^{2}noCliME, including a Cloud Imaging Probe (CIP), a Precipitation Imaging Probe (PIP), and a Cloud Condensation Nuclei Counter (CCN-DMT). Micro Rain Radars (MRRs) were located at SPL (3 MMR2s), mid-mountain (MMR-

Pro), and SGS (MRR-Pro). Mid-Mountain also hosted a MP-3000A Profiling MWR and a CL61 ceilometer/lidar. Rawinsondes were launched at SGS. Of the full suite of S^2noCliME instrumentation, the following subset are used in this study, with locations of the instrument sites as pictured in Figure 2.1: SEA-POL, MWR at mid-mountain, and Rawinsondes at SGS.

2.1.2 SEA-POL Radar

Reflectivity from SEA-POL plan position indicator (PPI) scans are used to assess the presence and spread of precipitation. Dual-polarization radar variables (Z_h, Z_{DR}, ρ_{HV}) and radial velocity from SEA-POL range height indicator (RHI) scans are used to infer precipitation characteristics and processes. Because this study focuses on snowfall near the terrain barrier, only RHI angles facing east towards the Park Range are analyzed. These angles are 60°, 120°, 80.4°, 80.6°, 80.8°, 81.0°, 81.2°, 91.9°, 92.1°, 92.3°, 92.5°, and 93.7° as indicated by the colored lines in Figure 2.1. SEA-POL measures over a range of 120 km, but due to decreased confidence with distance from beam broadening and blockage, only RHI data up to 60 km from the radar is analyzed. SEA-POL operated with a beam width of 1°, sensitivity of -7 dBZ at 100 km, 100 m gate spacing out to 120 range, and 31.8 m/s Nyquist velocity.

SEA-POL RHI scans were executed on 20 minute cycles, but not every angle was executed with the same repeat time interval. In each cycle, RHIs at the five angles centered on SPL (91.9°, 92.1°, 92.3°, 92.5°, 93.7°) were performed in the first two minutes. RHIs towards cardinal directions and towards KASPR and SPL were performed from the :09 through the :12 minute marks (including 60°, 80.8°, 92.3°, and

120°). From :13 to through :16, 8 scans towards KASPR and SPL were executed (92.1°, 92.3°, 92.5°, 80.4°, 80.6°, 80.8°, 81.0°, 81.2°).

This study uses the first version of the quality-controlled SEA-POL radar data (V0.1), which includes IOP-specific corrections to Z_{DR} biases. Non-meteorological echo was also removed for this version of the data, including clutter mitigation. However, the quality control process for this data is iterative and ongoing, including removing remaining clutter and determining the final derived version of K_{DP}, so the data used in this study may not be the final version. Note that the lowest unblocked elevation angle over SPL is 1.5°. For ease of statistical analysis, gridded versions of SEA-POL RHIs, on a 0.25 horizontal x 0.25 km vertical grid, are used in this study to create 2D histograms using NumPy (Harris et al. 2020) and to infer specific microphysical processes at individual times. Furthermore, echo-top heights across each IOP are defined as the highest altitude AMSL in which a reflectivity of 10 dBZ is reached, plotted as distributions using the Matplotlib histogram function (Hunter 2007).

2.1.3 Rawinsondes

To obtain vertical profiles of the atmospheric environment, Rawinsondes were launched from SGS during daylight hours during IOPs, with options of 15, 18, 21, and 00 UTC. The Version 1.0 quality controlled iMet-4 Rawinsonde data provides measurements of temperature (°C), relative humidity (%), wind speed (m/s), wind direction (°), height above ground level (AGL; m), and atmospheric pressure (hPa). For this study, Rawinsonde data is visualized on Skew-T diagrams using MetPy (May et al. 2022), in which wind speeds are converted to knots (kts) and dewpoint temperature values are calculated from the temperature and relative humidity fields using built-in MetPy functions. Due to concerns over reliability, the surface data point is not included on the Skew-Ts. Furthermore, unrealistic dewpoint observations were occasionally captured in the stratosphere, including in data from the 01-11 1800 UTC launch during IOP3, but do not impact the analysis for this study. Added to the Skew-T diagrams is the approximate pressure level of SPL as the atmospheric pressure associated with the height AGL closest to 1200 m, which is the height of SPL above the height of SGS (3220 m AMSL - 2020 m AMSL).

2.1.4 SPL Anemometer

Point wind observations at SPL are used as a measure of local flow variability at a higher temporal resolution than provided by the Rawinsondes. Wind data was obtained courtesy of SPL and MesoWest, from a 12-m anemometer located at SPL, where wind speed (mph) and direction (°) are measured every five minutes. When displaying and analyzing the flow variability across IOP3 and IOP4, wind speed is converted to kts using the built-in MetPy function (May et al. 2022). The anemometer data is collected at 3210 m AMSL.

2.1.5 Mid-Mountain MWR

Retrieved integrated vapor (cm) and LWP (mm) from the mid-mountain MP-3000A MWR Version 1.0 dataset are used as continuous observations of local, on-mountain, moisture content. The MWR uses passive brightness temperature observations at frequencies between 22 and 30 GHZ for water vapor profiling. The noted column integrated values are based on measurements from the surface to 10 km above the ground, with data frequency of 1 minute, using the Radiometrics neural network approach (Solheim et al. 1998).

2.2 Supplemental Datasets

2.2.1 Shuttle Radar Topography Mission (SRTM)

SRTM 1-arc second global data is used for terrain elevation profiles associated with the chosen SEA-POL RHI angles. The SRTM data was converted to a 250 m spatial resolution matched along each selected SEA-POL RHI.

2.2.2 Snow Accumulation Data

The National Atmospheric and Oceanic Administration (NOAA)'s Gridded Snowfall Analysis was used to obtain 48-hr snowfall accumulations associated with each IOP (NOAA 2022). The 48-hr analyses are aggregated from 24-hr analyses which are generated for 00 and 12 UTC. The observations in these analyses are obtained from numerous observing networks, including COOP, CoCoRaHS, ASOS, FAA, and NWS spotters. For plotting purposes, data is converted from meters to inches. Further accumulation data is obtained from the Steamboat Springs Ski Patrol's daily reports which note new mid-mountain and summit snowfall (in).

2.2.3 ECMWF Fifth Generation Reanalysis (ERA5)

The European Centre for Medium-Range Weather Forecasts (ECMWF) Reanalysis v5 (ERA5) is used to analyze the large-scale environment associated with each IOP. The ERA5 data is hourly and gridded to a grid of 0.25° latitude and longitude (Hersbach et al. 2023). ERA5 data was downloaded from the Copernicus Climate

Change Service's Climate Data Store for each hour across the IOPs. ERA5 geopotential heights (m) at 500 hPa and absolute vorticity at 500 hPa, calculated as the sum of ERA5 relative vorticity (s^{-1}) at 500 hPa and planetary vorticity at each data point's latitude, as described in equations 2.1 and 2.2, are plotted to analyze the synoptic environment throughout each IOP.

$$Planetary\ Vort.(lat.) = 2\ x\ (7.27\ x\ 10^{-5})\ x\ \sin\left(deg.lat\ x\ \frac{\pi}{180}\right) \tag{2.1}$$

$$Abs.Vort.(lat.) = Planetary\ Vort.(lat.) + 500 - hPa\ Rel.Vort.(lat) \tag{2.2}$$

ERA5 vertical integrals, for a column of air from Earth's surface to the top of the atmosphere, of eastward and northward water vapor flux (kg m^{-1} s^{-1}) are used to calculate IVT as:

$$IVT = \sqrt{(eastward\ water\ vapor\ flux)^2 + (northward\ water\ vapor\ flux)^2} \tag{2.3}$$

ERA5 IVT is visualized on spatial maps to analyze the amount and direction by which moisture is flowing into the region during an IOP.

2.2.4 Weather Research and Forecasting Model (WRF)

Because rawinsondes were not launched overnight or more than four times during the day, and because ERA5 has limited spatial and temporal resolution compared to that of the SEA-POL RHIs, the Weather Research and Forecasting (WRF) model is used to obtain high-resolution details of the atmospheric environment. A season-long WRF simulation, the domain and parameterizations of which are shown in Figure 2.2 and Table 2.1, respectively, was run to encompass the entirety of

S^2noCliME. Cross-sections within the 0.5-km domain (Fig. 2.2) are matched to SEA-POL RHI angles for direct comparison of environmental variables to SEA-POL variables to enable comprehensive microphysical inferences. The closest WRF cross-section output time for each east-facing RHI angle is matched to the corresponding gridded SEA-POL RHI file. To match the WRF cross-sections to the gridded files, WRF variables are binned for each RHI longitude point and the binned values are averaged for each WRF cross-section height. The result is then interpolated onto the heights of the SEA-POL RHI grid.

The matched output is used to create 2D histograms using NumPy (Harris et al. 2020), which display the distribution of SEA-POL variables (Z_h and Z_{DR}) with environmental variables from WRF. The WRF variables used for these histograms are temperature (°C), water vapor mixing ratio (q_v; g/kg), and relative humidity with respect to ice (RH_i; %). The matched output is also used for environmental context in plots of SEA-POL RHIs. WRF variables used to contextualize individual RHIs are temperature (°C), q_v (g/kg), cloud water mixing ratio (q_c; g/kg), wind speed (kts), and wind direction (°). The WRF output uses the Thompson microphysics scheme, in which number and droplet number concentration of cloud water is explicitly predicted (Thompson and Eidhammer 2014).

2.3 Flow Regime Framework

2.3.1 Flow Regime Definitions

To analyze the impact of the subtle variations in local flow on precipitation characteristics, three flow regimes are defined: *north-westerly, westerly,* and *south-*

westerly (Table 2.2) based on wind direction as measured by the SPL anemometer during times of precipitation as indicated in the terrain-facing SEA-POL RHIs. As briefly noted in Section 1.5, these times are: 0330 UTC 11 January 2025 through 0900 UTC 12 January 2025 for IOP3, and 1830 UTC 17 January 2025 through 0830 UTC 18 January 2025 for IOP4. Windroses were created from SPL wind data across each of these time ranges, using the Python Matplotlib and NumPy windrose library (Hunter 2007; Harris et al. 2020). The results revealed largely westerly winds across both cases, and so a narrow range of wind directions were defined as *westerly* flow (260-280°), with *north-westerly* defined as any more northerly angle (> 280°) and *south-westerly* as more southerly flow (< 260°), in order to assess the impact of subtle changes in flow.

2.3.2 Data Subdivision

To isolate the impact of flow direction on inferred microphysical processes, SEA-POL data is subdivided by flow regime during the times noted in Section 2.3.1. Because there are brief periods of time with missing wind data, as well as periods in which flow regime varies between neighboring data points, a time range was defined as a given flow regime when wind observations fell within the angle range of that regime for two or more consecutive data points (spans 10 minutes or longer). SEA-POL data is subdivided by flow regime through grouping RHIs where the scan was executed within a time range associated with the flow regime.

2D histograms are created from the SEA-POL RHI files grouped to each flow regime using NumPy (Harris et al. 2020). The histograms display distributions of Z_h

and Z_{DR} with altitude using data from all RHI files that fall within time ranges associated with each flow regime.

2.4 Figures and Tables

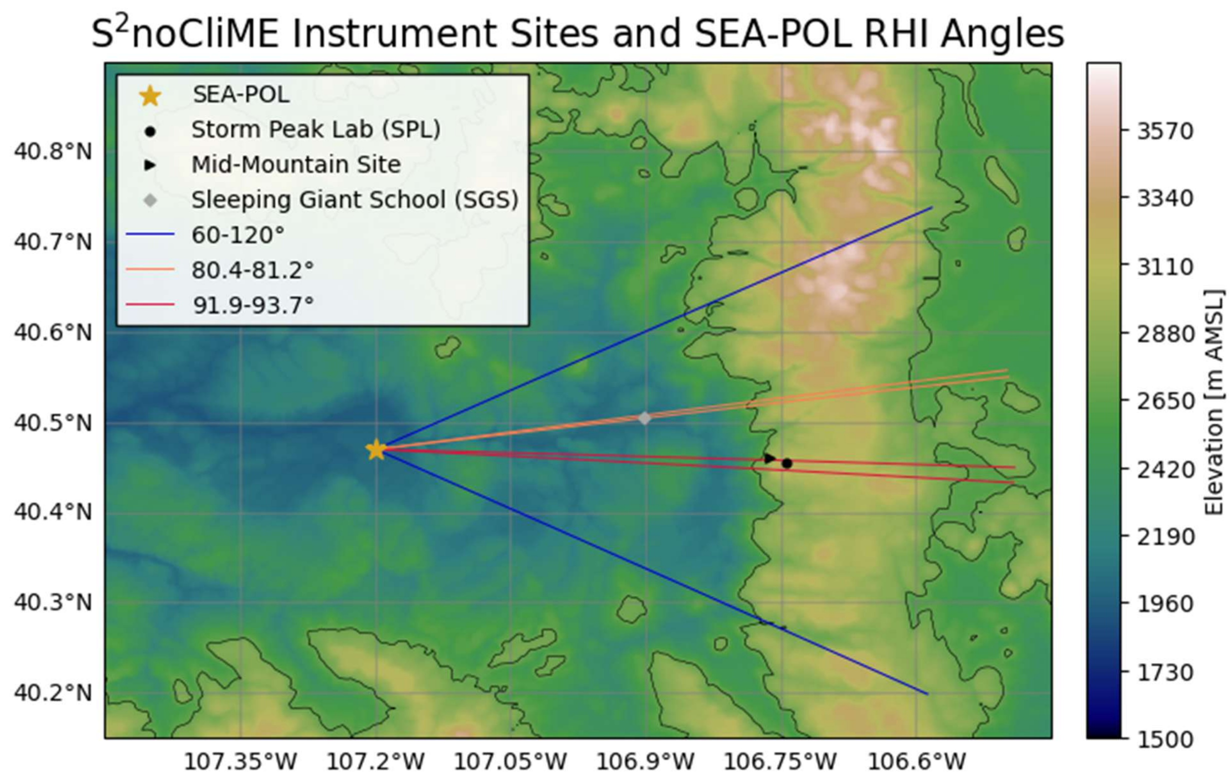

Figure 2.1: Terrain elevation map near S2noCliME instrument sites. Star indicates location of SEA-POL radar; gray diamond indicates location of SGS; black diamond indicates location of mid-mountain site; black circle indicates location of SPL. Colored lines indicate range of selected SEA-POL RHI angles, through 60 km from the radar. Thin black line depicts 2670 m elevation contour.

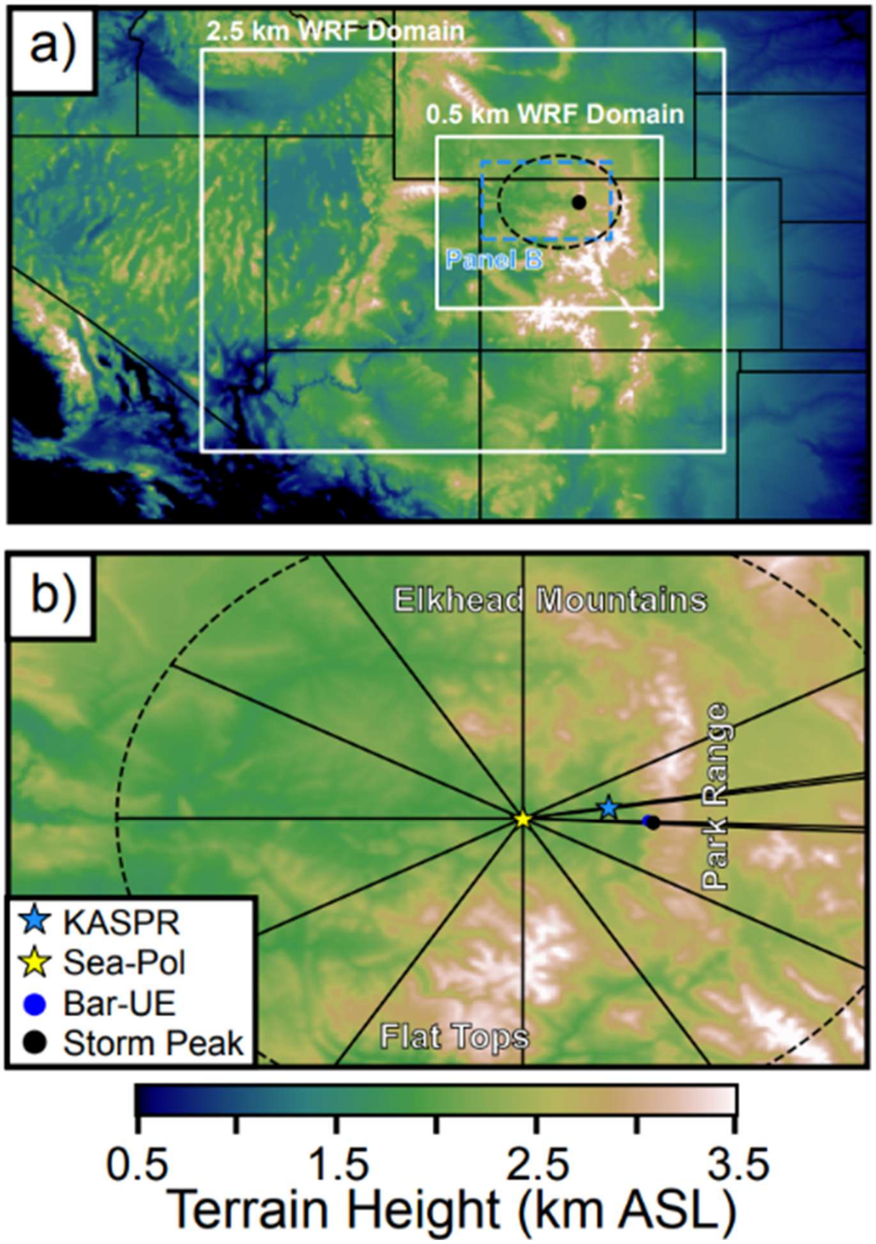

Figure 2.2: (a) 2.5 km and 0.5 km WRF domains for 2024-25 seasonal simulations, with Steamboat Springs, Colorado marked by black circle and (b) range and angles of RHI-matched WRF output. Figure courtesy of Troy Zaremba at the University of Washington.

	2500 m Domain	500 m Domain
Model Version	WRF version 4.6.1	WRF version 4.6.1
Horizontal Grids	540 x 360	450 x 300
Time Step	15 s	3 s
Driving Data	ERA5	One-way nest from 2.5 km domain WRF outputs
Vertical Coordinate	120 terrain-following eta levels	
Land Surface Model	Noah MP	
Radiation	RRTMG LW & SW	
Planetary Boundary Layer Scheme	MYNN	
Microphysics	Thompson-Eidhammer (TE Thompson and Eidhammer 2014)	

Table 2.1: Table noting key details of WRF configuration and parameterizations for 2024-25 seasonal simulations. Table adapted from Troy Zaremba at the University of Washington.

North-Westerly Flow	> 280°
Westerly Flow	260-280°
South-Westerly Flow	< 260°

Table 2.2: Flow regime definitions for IOP3 and IOP4. Regime title on left; associated range of wind direction as measured at SPL on right.

Chapter 3

Overview of Cases

The two selected cases, IOP3 (0330 UTC 11 January 2025 through 0900 UTC 12 January 2025) and IOP4 (1830 UTC 17 January 2025 through 0830 UTC 18 January 2025), were chosen for this analysis because they are associated with different large-scale patterns of moisture transport. Specifically, IOP4 was associated with minimal moisture transport while IOP3 was associated with a greater magnitude of moisture transport. This section will provide an overview of the large-scale dynamical and moisture transport evolution, local wind patterns and moisture availability, and the resulting snowfall associated with each case.

3.1 Large-Scale Evolution

The large-scale evolution of each case is evaluated through analysis of geopotential heights and absolute vorticity at 500 hPa, to assess the strength and stability associated with mid-level flow, and IVT, to assess the total transport of vapor.

Snowfall during IOP3 is associated with the passage of an upper-level shortwave (Fig. 3.1). Near Steamboat Springs, ahead of the onset of precipitation east of SEA-POL, 500-hPa absolute vorticity is minimal, around 10^{-4} s^{-1}, and 500-hPa geopotential heights are around 5620 m (Fig. 3.1a). As the event progresses, just after IVT values reach their maximum in the region during IOP3 (0700 UTC 11 January 2025 and 0800 UTC 11 January 2025; between Fig. 3.2a, b) and precipitation becomes widespread (Fig. 3.3c), the gradient in the 500-hPa geopotential height field intensifies (Fig. 3.1b). Later in the event, magnitudes of 500-hPa absolute vorticity reach a maximum of around 2.5 x 10^{-4} s^{-1}, the 500-hPa geopotential heights decrease to around 5460 m, and a tilted trough passes over the region (Fig. 3.1c). Near the end of the event, absolute vorticity magnitudes reach back to low values around 10^{-4} s^{-1}, the 500-hPa geopotential height contours space out again (Fig. 3.1d), and precipitation is less widespread (Fig. 3.3h).

During IOP4, snowfall is associated with less prominent change in the 500-hPa absolute vorticity magnitudes and gradients in 500-hPa geopotential height (Fig. 3.4). Ahead of the start of widespread precipitation, near the location of Steamboat Springs, 500-hPa geopotential heights sit around 5510 m and absolute vorticity magnitudes are near 10^{-4} s^{-1} (Fig. 3.4a). After the onset of precipitation (Fig. 3.6a, b, c), 500-hPa absolute vorticity reaches maximum values near 1.5 x 10^{-4} s^{-1} (Fig 3.4c) and precipitation is most widespread (Fig. 3.6d). 500-hPa absolute vorticity values drop back to around 10^{-4} s^{-1} near the end of the event (Fig. 3.4d) as precipitation becomes less widespread (Fig. 3.6f). Through the duration of the event, 500-hPa geopotential heights decrease near Steamboat Springs (Fig. 3.4b, c, d).

Both IOP3 and IOP4 feature greater magnitudes of moisture transport ahead of the time of maximum observed 500-hPa absolute vorticity (Fig. 3.2a, b; Fig. 3.5a, b). However, the magnitude and direction of moisture transport varies between the IOPs. During IOP3, IVT reaches magnitudes near 150 kg m^{-1} s^{-1} (Fig. 3.2b) during widespread precipitation (Fig. 3.3c). The large-scale moisture transport is also oriented from the north-west (Fig. 3.2a, c, d) multiple times during precipitation in IOP3 (Fig. 3.3a, c, f). During IOP4, IVT magnitudes do not reach much above 70 kg m^{-1} s^{-1} (Fig. 3.5) and the link between IVT and precipitation coverage is unclear (Fig. 3.6d; Fig. 3.5c). Moisture transport is also more visibly westerly through the duration of IOP4 (Fig. 3.5). The moisture transport is tied to large-scale flow and integrated over the entire depth of the atmosphere. However, to assess the impact of the local moisture distribution and transport relative to terrain, further investigation into the evolution of how greater transport is imprinted on local winds, relative to terrain, and how the large-scale moisture is distributed in the vertical and with respect to temperature is necessary.

3.2 Local Winds and Moisture Availability

Rawinsonde observations of wind, dewpoint, and temperature profiles during times of precipitation depict different local environments between the two events. During IOP3, tropospheric temperature and dewpoint profiles show consistently minimal (< 3 °C) dewpoint depressions – suggesting deeply moist conditions through a range of temperatures (Fig. 3.7) while precipitation is likely occurring over SGS (Fig. 3.3e, f, g). There is some variation in wind direction, from westerly to north-westerly to south-westerly, through the troposphere (Fig. 3.7a, b) until after 1800 UTC 11 January 2025 (Fig. 3.3f) in which winds become consistently north-westerly throughout the vertical, as illustrated by the 0000 UTC 12 January 2025 skew-T (Fig. 3.7c), and IVT is minimal but north-westerly oriented (Fig. 3.2c). Through this sampled portion of IOP3, rawinsonde profiles depict SPL to be within temperatures of -12 to -14 °C, and at a level of north-westerly flow (Fig. 3.7). During IOP4, low-level (surface to 680 hPa) conditions are consistently drier (dewpoint depressions > 6 °C) and warmer (near-surface temperatures close to 0 °C) than in IOP3 (Fig. 3.8) for the times sampled by rawinsondes (2100 UTC 17 January 2025 and 0000 UTC 18 January 2025), although there is likely no precipitation occurring at the sonde launch site (Fig. 3.6b, c). Moist conditions are present aloft during these times, which are around the times in which IOP4 IVT is maximized (2000 UTC 17 January 2025 through 2300 UTC 17 January 2025; Fig. 3.5a, b). At 2100 UTC 17 January 2025, there are two moist layers where dewpoint depressions are less than 3 °C: one centered at 500 hPa and around temperatures colder than -20 °C, and one just above the height of SPL within temperatures between -12 and -15 °C (Fig. 3.8a). At 0000 UTC 18 January 2025, there is a deeper moist layer from 620 to 520 hPa within -15 to -25 °C (Fig. 3.8b). Furthermore, the rawinsonde profiles for this case depict little change in wind direction through the vertical and temperatures consistently around -10 °C near the height of SPL, which are conditions that would support the riming or aggregation of pristine particles near SPL.

While rawinsonde observations hint at the evolution and distribution of winds and moisture during IOP3 and IOP4, the observations are temporally limited and may not capture variability in winds crucial to investigating the impact of local flow on precipitation processes. This variability may include variation of winds tied to changes in the large-scale evolution of these cases described in Section 3.1, such as maximum IVT in IOP3 (Fig. 3.2b) and maximum vorticity in IOP4 (Fig. 3.4c). Wind observations at SPL are therefore utilized to extend the picture of wind variability in the two IOPs.

On-mountain, at SPL, 12-m surface wind direction varies between true south-westerly and north-westerly during precipitation associated with IOP3, with winds being most commonly *north-westerly* as the regime is defined in Section 2.3.1 (Fig. 3.9a). Windspeeds at SPL during IOP3 vary greatly, from around 4 to greater than 20 kts, with the weakest (< 8 kt) winds present during *south-westerly* and *westerly* flow as the regimes are defined in Section 2.3.1 (Fig. 3.9a). The greatest proportion of strong (> 12 kt) winds are present during north-westerly flow. During times of precipitation associated with IOP4, winds at SPL vary between true west-south-west and west-north-west, and are most commonly *westerly* as the regime is defined in Section 2.3.1 (Fig. 3.9b), which aligns with the rawinsonde observations. Winds at SPL during IOP4 are not weaker than 8 kts, and winds weaker than 12 kts are only present during north-westerly flow (Fig. 3.9b).

Overall, there is greater wind variability present in IOP3, in both direction and speed, which may be associated with changes resulting from the shortwave passage and evolution of the 500-hPa geopotential height gradient noted in Figure 3.1 and Section 3.1. In IOP4, more consistently strong and westerly-oriented winds are observed, which could be associated with the more static pattern, and tighter gradient, in 500-hPa geopotential heights noted in Figure 3.3 and described in Section 3.1. Like in case of the winds, assessing the imprint of large-scale moisture transport on local moisture availability is necessary to understand the impact of moisture variability on precipitation processes in IOP3 and IOP4. Observations of local moisture availability are obtained from the mid-mountain MWR.

While exact magnitudes may be biased high during IOP3, there are multiple time ranges of relatively enhanced integrated water vapor and liquid water, which is inferred to be SLW due to the consistent temperatures below 0 °C across both IOPs, measured on-mountain (Fig. 3.10). As visible in Figure 3.10, there are notable peaks in liquid water from 0300 to 0600 UTC 11 January 2025 during south-westerly flow at SPL, between 0700 and 0800 UTC 11 January 2025 during north-westerly flow at SPL and near maximum IVT (Fig. 3.2), between 0930 and 1100 UTC 11 January 2025 during westerly flow at SPL and near maximum IVT (Fig. 3.2), around 1130 UTC 11 January 2025 during north-westerly flow at SPL, and from around 1700 to 2030 UTC 11 January 2025 during north-westerly and westerly flow at SPL – around the time of shortwave passage (Fig. 3.1). There are also peaks of smaller magnitude and duration present during times of lingering precipitation (beyond 2100 UTC 11 January 2025; Fig. 3.3g, h) – particularly during north-westerly and south-westerly flow at SPL (Fig. 3.10).

There are also time periods of relative peaks in magnitude of water vapor and liquid water during the duration of IOP4 precipitation (Fig. 3.11). As visible in Figure 3.11, there are notable peaks in liquid water and water vapor from 0100 through 0200 UTC 18 January 2025 during maximum absolute vorticity (Fig. 3.4) and westerly and north-westerly flow at SPL, between 0230 and 0430 UTC 18 January 2025 during variable flow at SPL, and around 0500 UTC 18 January 2025 during variable flow at

SPL. There is a smaller, but present, relative peak in liquid water and water vapor around 1900 UTC 17 January 2025 associated with south-westerly and westerly flow at SPL, as well as towards the end of the event, after around 0600 UTC 18 January 2025 associated with variable or north-westerly flow at SPL (Fig. 3.11). Furthermore, a notable dip in liquid water during IOP4 occurs between 2330 UTC 17 January 2025 and 0100 UTC 18 January 2025 during north-westerly and westerly flow at SPL. Relatively high magnitude peaks in liquid water, around 1900 UTC 17 January 2025, around 0100 to 0130 UTC 18 January 2025, and near 0315 UTC 18 January 2025 are associated with westerly flow (Fig. 3.11). Overall, there is evident temporal variability in local moisture despite the consistently minimal IVT noted in Figure 3.5.

Although peaks in liquid water largely correspond to those in water vapor (Fig. 3.10; Fig. 3.11), there are moments in which the relative magnitudes of water vapor and liquid water peaks vary. In particular, during IOP3, the peak in liquid water with the transition from south-westerly to north-westerly flow around 0730 UTC 11 January 2025 is greater than the peaks in liquid water from 0300 to 0600 UTC 11 January 2025, but the corresponding peak in water vapor around 0730 UTC 11 January 2025 is of a smaller magnitude than the corresponding peaks from 0300 to 0600 UTC 11 January 2025 (Fig. 3.10). This pattern is also present between the corresponding liquid water and water vapor peaks during north-westerly flow around 1130 UTC January 2025 and those during westerly flow between 0930 and 1100 UTC 11 January 2025 (Fig. 3.10). Furthermore, the onset of liquid water peaks from 1700 to 2030 UTC 11 January 2025 begins just ahead of the corresponding water vapor peaks

(Fig. 3.10). There are also occasional moments of anti-correlation between the peaks beyond 2100 UTC January 2025 (Fig. 3.10). During IOP4, the most notable difference between peaks in liquid water and water vapor is the slight decrease in magnitude of the difference between water vapor and liquid water between 0600 and 0730 UTC 18 January 2025. Differences between the timing of high vapor and high liquid content could tie to differences in snowfall characteristics, where high vapor availability would be expected of pristine crystal growth and the presence of liquid water could support riming. In general, the considerable variation in moisture, as well as local flow, suggest variability in the type, and extent, of snow growth that could be supported at different times throughout each IOP beyond what can be tied back solely to IVT.

It is also worth noting that there are conditionally unstable layers present within the IOP4 rawinsonde observations: from about 720 to 590 hPa and 550 to 540 hPa at 2100 UTC 17 January 2025, and from 780 to 500 hPa at 0000 UTC 18 January 2025. These layers may further influence snow growth and resulting characteristics during IOP4.

3.3 Snow Impacts

Precipitation east of SEA-POL occurred over the course of around 29.5 hours during IOP3, and around 14 hours during IOP4. IOP3 is associated with greater snowfall in the region encompassing Steamboat Springs and SPL than IOP4 (Fig. 3.12; Fig. 3.13). Snowfall accumulations resulting from IOP3 are particularly high on the mountains north of SPL (around 40.79°N, 106.9°W) and south-west of SPL (around 40.2°N, 107.3°W) where accumulations reached 24-28” according to the NOAA National Gridded Snowfall Analysis (Fig. 3.12). IOP4 is associated with similarly located relative peaks in snow accumulations over the mountains, but with less snowfall reported north of SPL (Fig. 3.13). Maximum accumulations resulting from IOP4 in the region are located on the peaks south-west of SPL (around 40.2°N, 107.3°W) which saw 8-10” of snow (Fig. 3.13). At the lower elevations of Steamboat Springs and the nearby valley, including the location of SGS, accumulations of 6-14” are reported to result from IOP3 (Fig. 3.12) while 0-2” are reported to result from IOP4 (Fig. 3.13). At the Steamboat Springs Ski Resort, ski patrol noted summit accumulations of 34” and mid-mountain accumulations of 20” associated with IOP3. For IOP4, summit and mid-mountain accumulations were noted to be 5” and 3”, respectively.

As might be expected, IOP3, which was associated with substantially greater IVT than IOP4 and was about twice the duration, correlated to substantially greater snowfall accumulations. However, accumulations over the mountains during IOP4 were non-zero, and the varying distribution of snowfall, along with variations in local winds and moisture availability, hint at controls over snowfall beyond IVT and event duration which warrant an in-depth look at the snow growth processes, and associated local flow and moisture conditions, that occurred through the duration of IOP3 and IOP4.

3.4 Figures

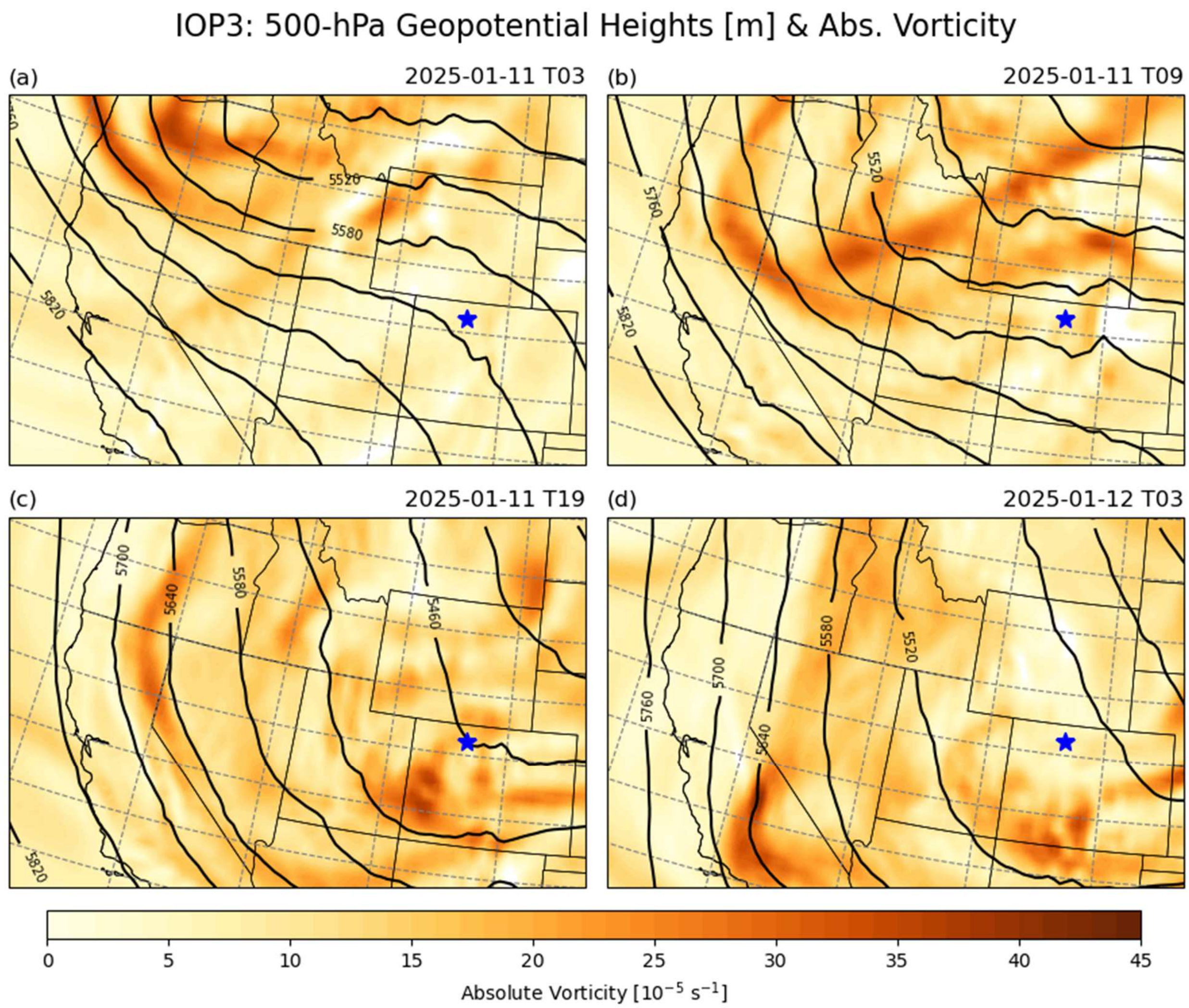

Figure 3.1: Evolution of 500-hPa geopotential heights in m (contours) and absolute vorticity in 10^{-5} s^{-1} (shading) for (a) 0300 UTC 11 January 2025, (b) 0900 UTC 11 January 2025, (c) 1900 UTC 11 January 2025, and (d) 0300 UTC 12 January 2025. Blue star indicates the location of Steamboat Springs. Fields calculated from ERA5 data.

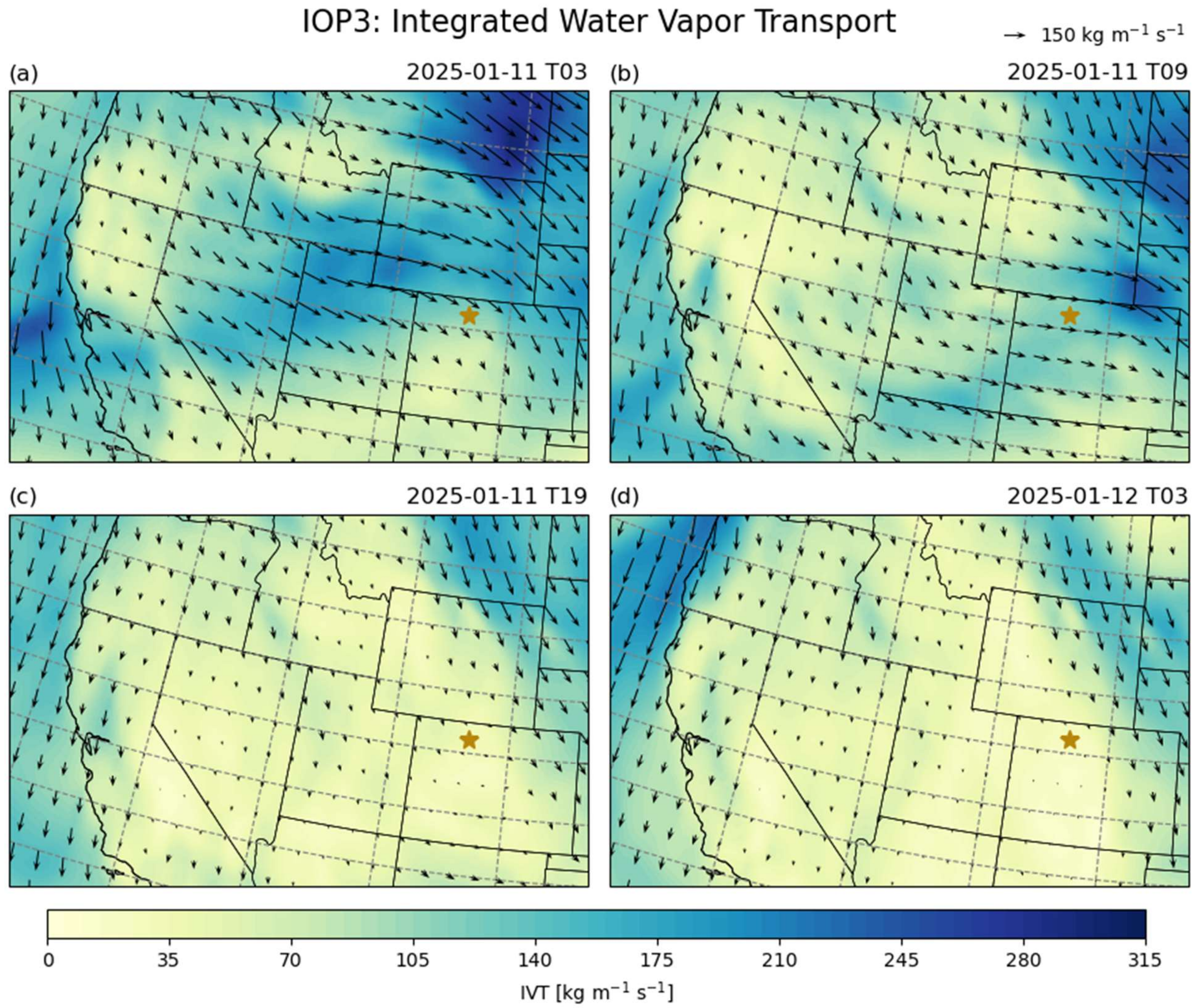

Figure 3.2: Evolution of ERA5 IVT in kg m^{-1} s^{-1} for (a) 0300 UTC 11 January 2025, (b) 0900 UTC 11 January 2025, (c) 1900 UTC 11 January 2025, and (d) 0300 UTC 12 January 2025. Gold star indicates the location of Steamboat Springs.

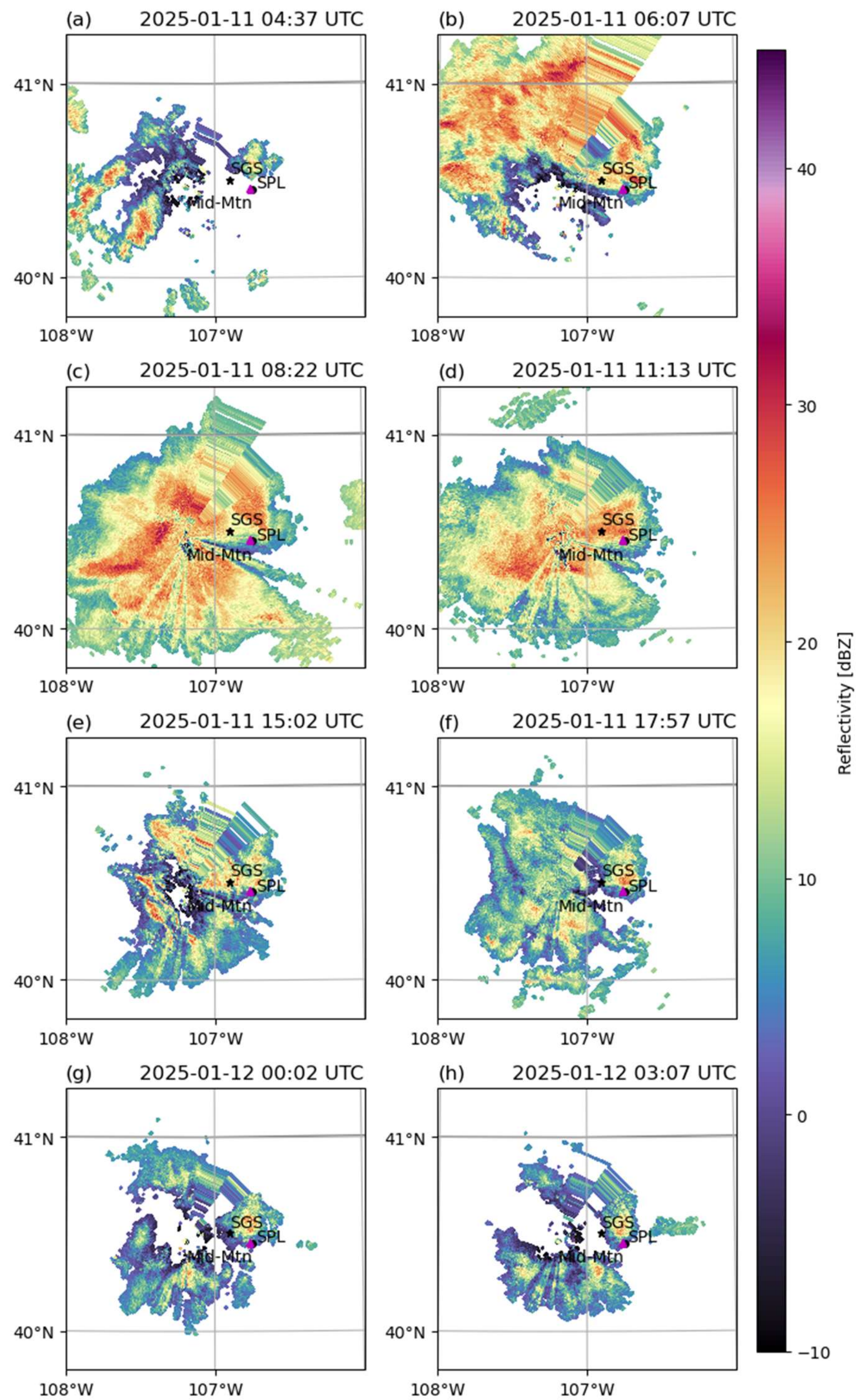

Figure 3.3: SEA-POL 2° PPIs at (a) 0437 UTC 11 January 2025, (b) 0607 UTC 11 January 2025, (c) 0822 UTC 11 January 2025, (d) 1113 UTC 11 January 2025, (e) 1502 UTC 11 January 2025, (f) 1757 UTC 11 January 2025, (g) 0002 UTC 12 January 2025, and (h) 0307 UTC 12 January 2025. Black star indicates location of SGS; black circle indicates location of SPL; magenta triangle indicates location of mid-mountain.

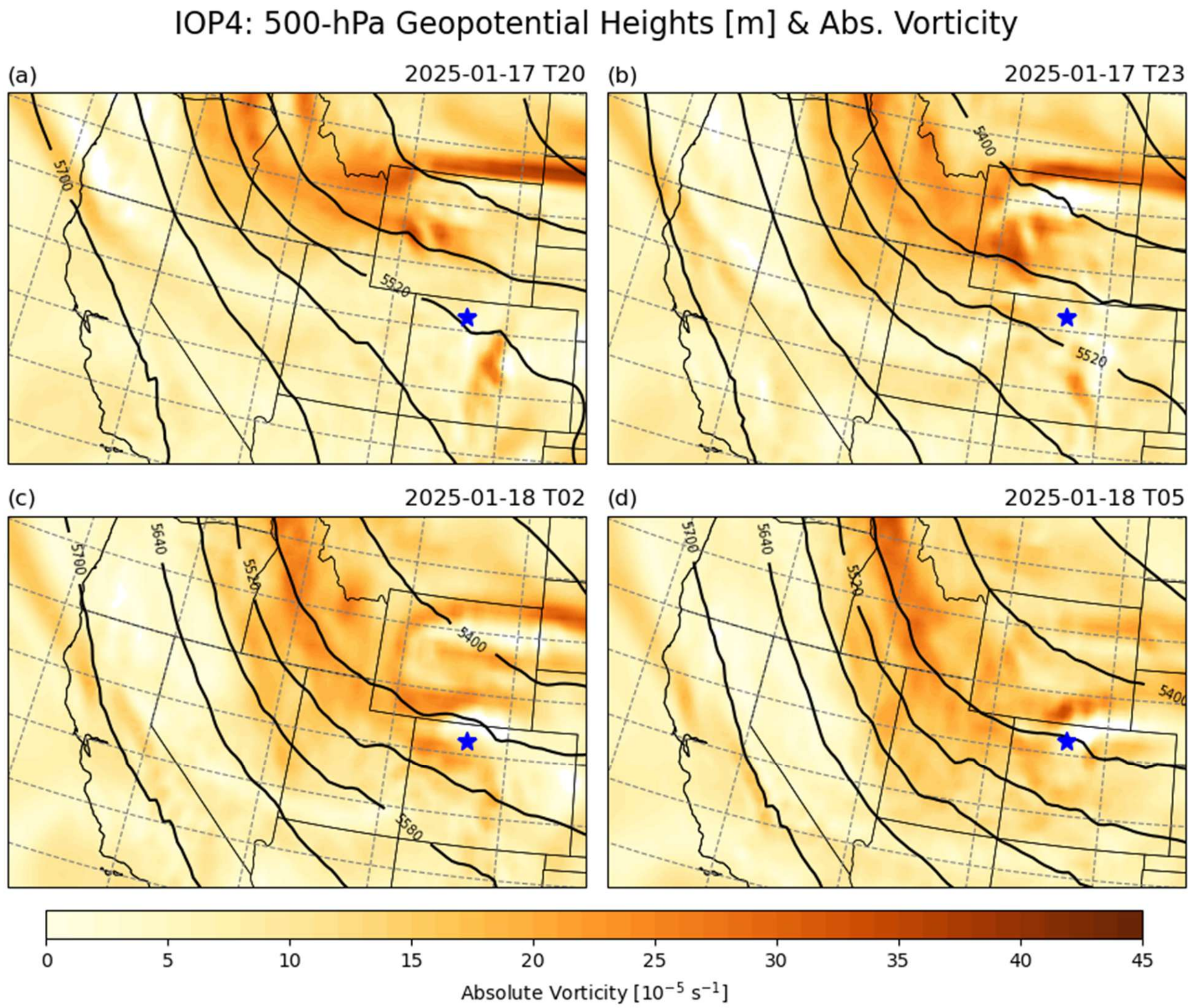

Figure 3.4: As in Figure 3.1, but for (a) 2000 UTC 17 January 2025, (b) 2300 UTC 17 January 2025, (c) 0200 UTC 18 January 2025, and (d) 0500 UTC 18 January 2025.

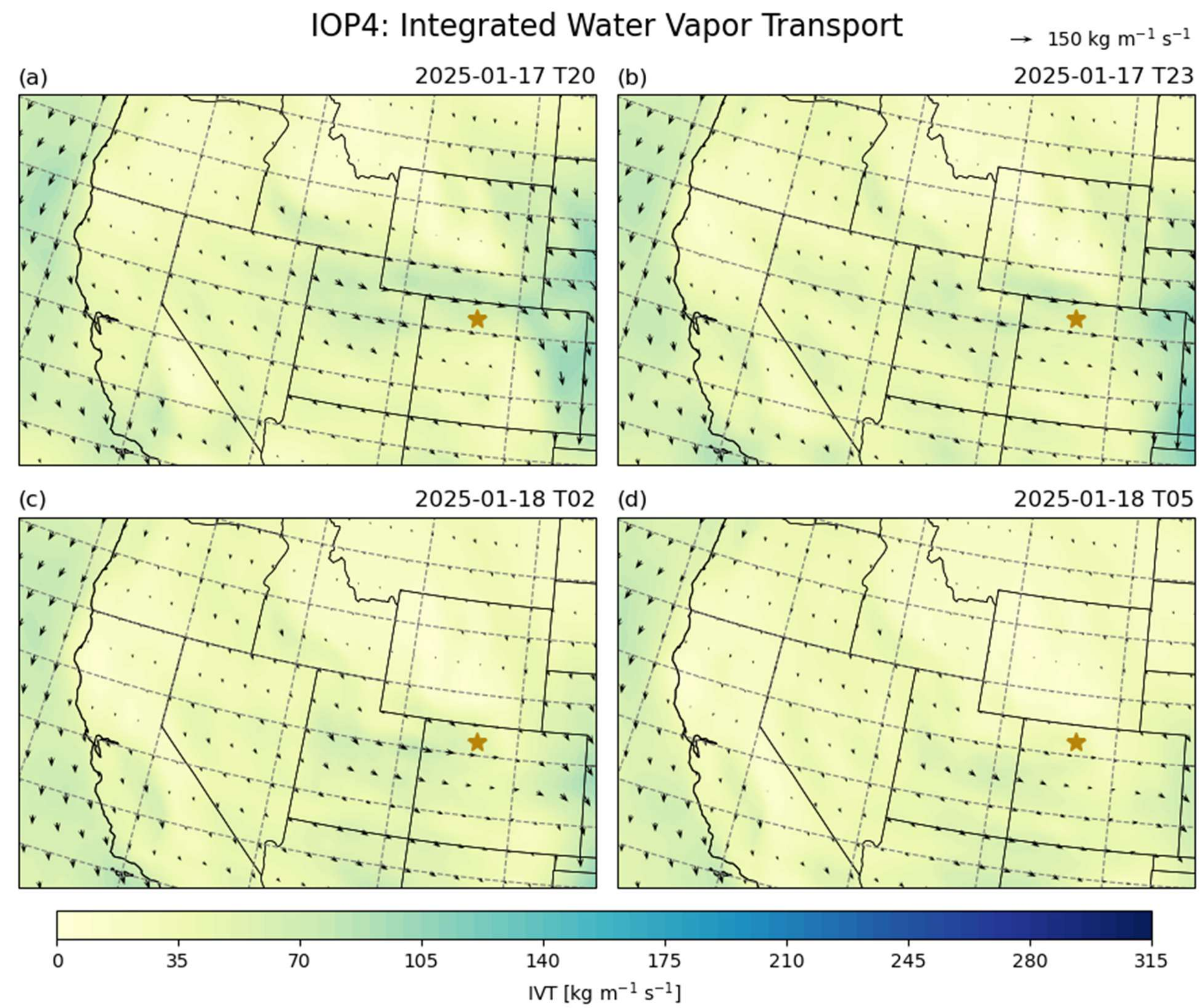

Figure 3.5: As in Figure 3.2, but for (a) 2000 UTC 17 January 2025, (b) 2300 UTC 17 January 2025, (c) 0200 UTC 18 January 2025, and (d) 0500 UTC 18 January 2025.

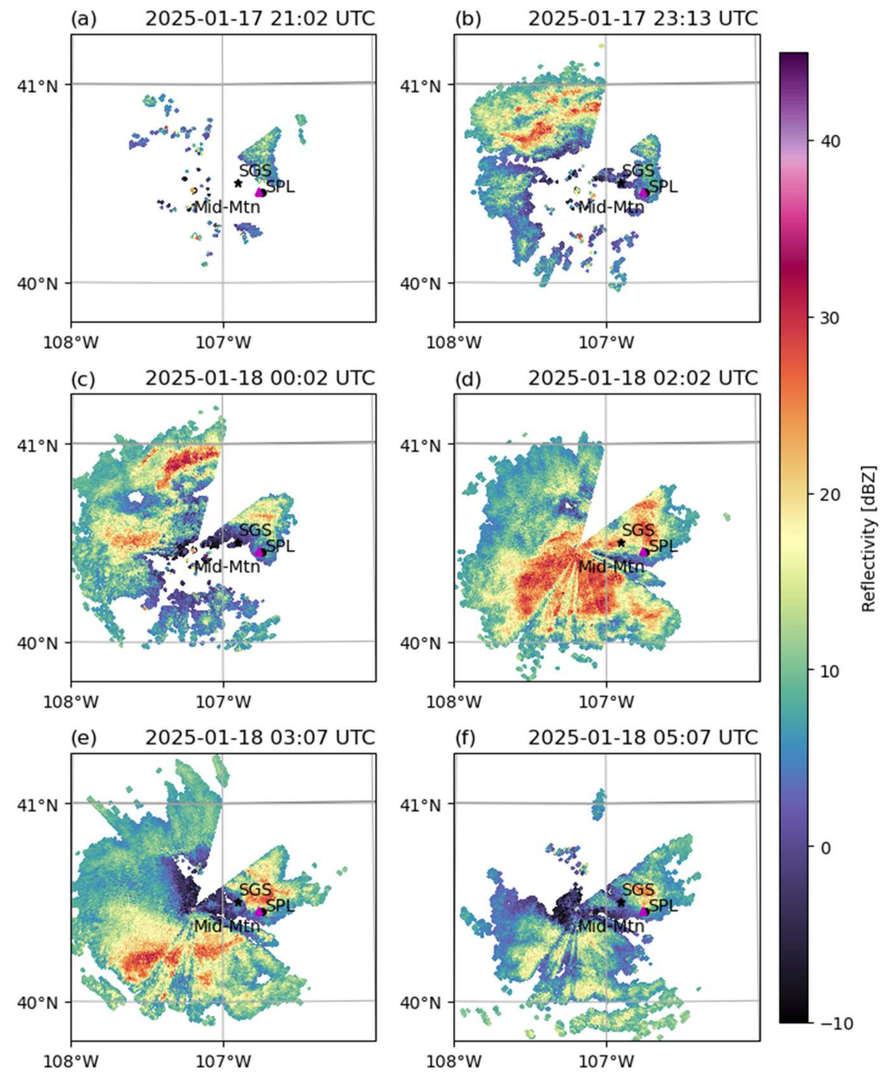

Figure 3.6: As in Figure 3.3, but for (a) 2102 UTC 17 January 2025, (b) 2313 UTC 17 January 2025, (c) 0002 UTC 18 January 2025, (d) 0202 UTC 18 January 2025, (e) 0307 UTC 18 January 2025, and (f) 0507 UTC 18 January 2025.

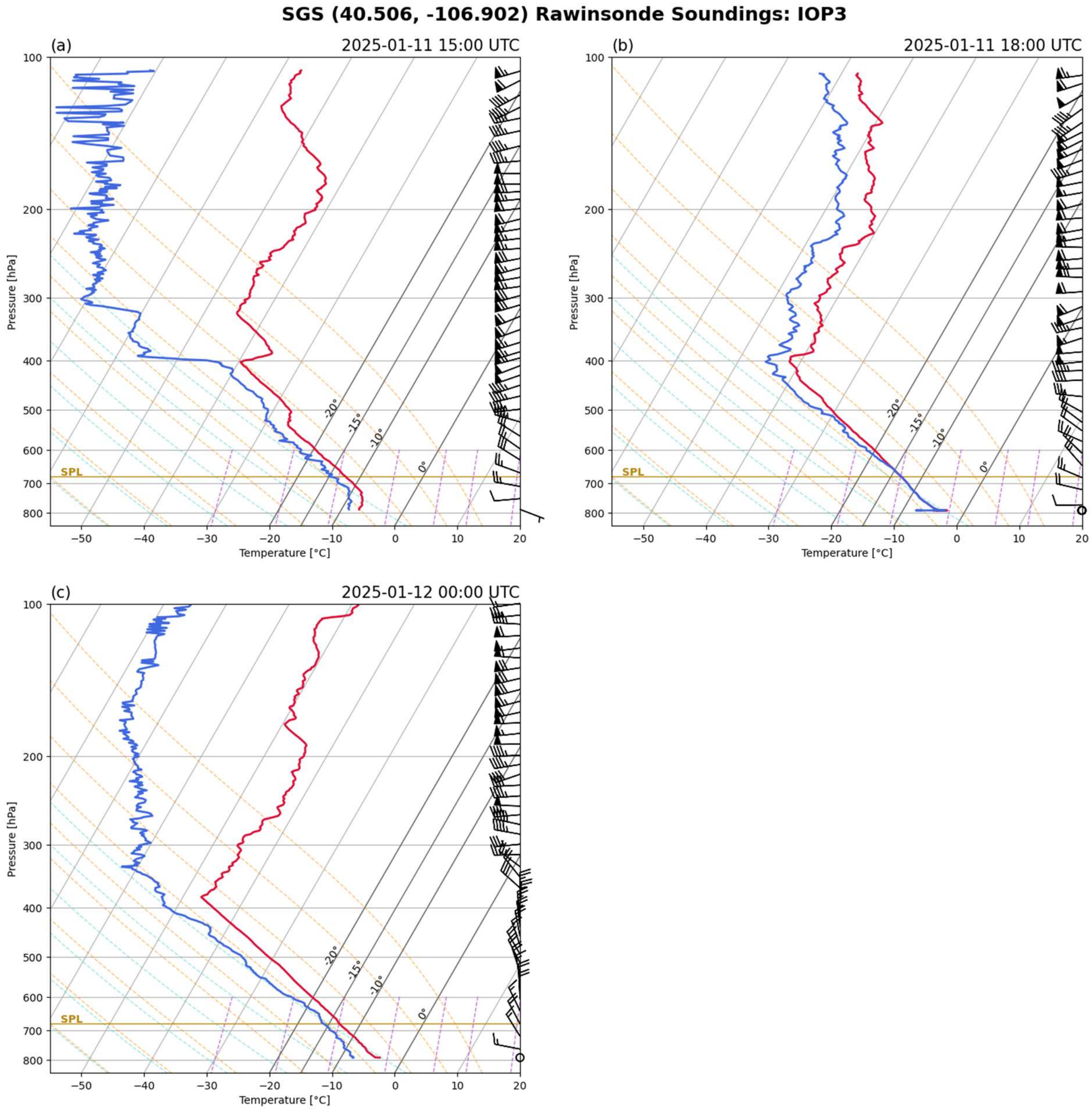

Figure 3.7: Skew-T diagrams depicting temperature in °C (red line), dewpoint temperature in °C (blue line), and winds in kts from SGS rawinsonde launches for (a) 1500 UTC 11 January 2025, (b) 1800 UTC 11 January 2025, and (c) 0000 UTC 12 January 2025. Gold line denotes the approximate pressure level of SPL.

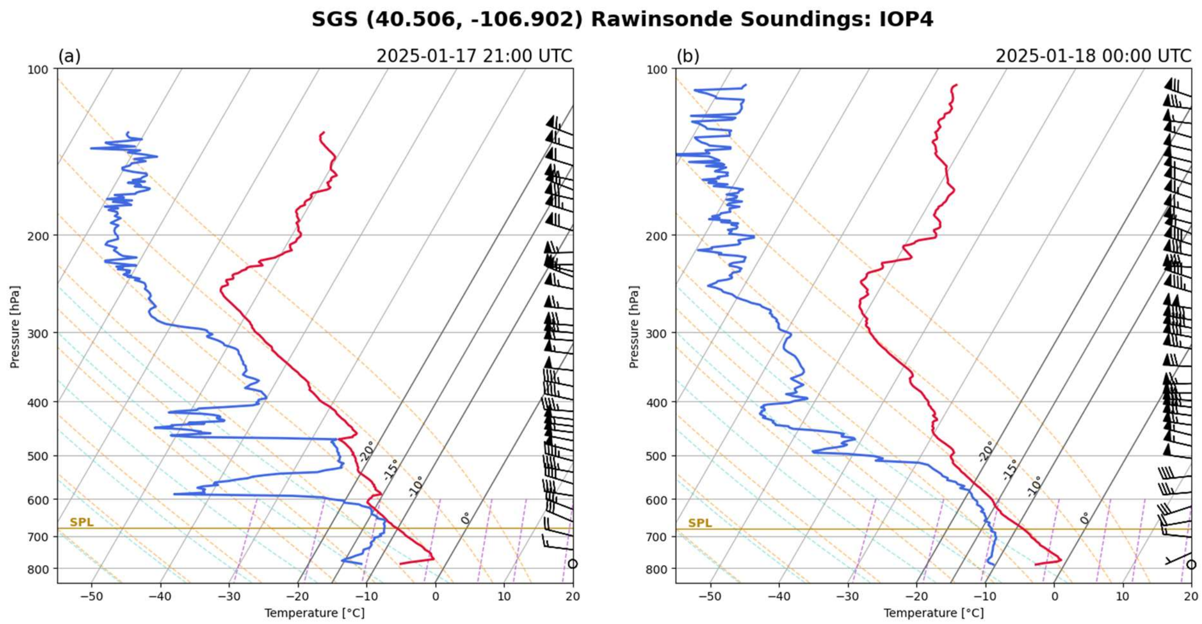

Figure 3.8: As in Figure 3.7, but for (a) 2100 UTC 17 January 2025 and (b) 0000 UTC 18 January 2025.

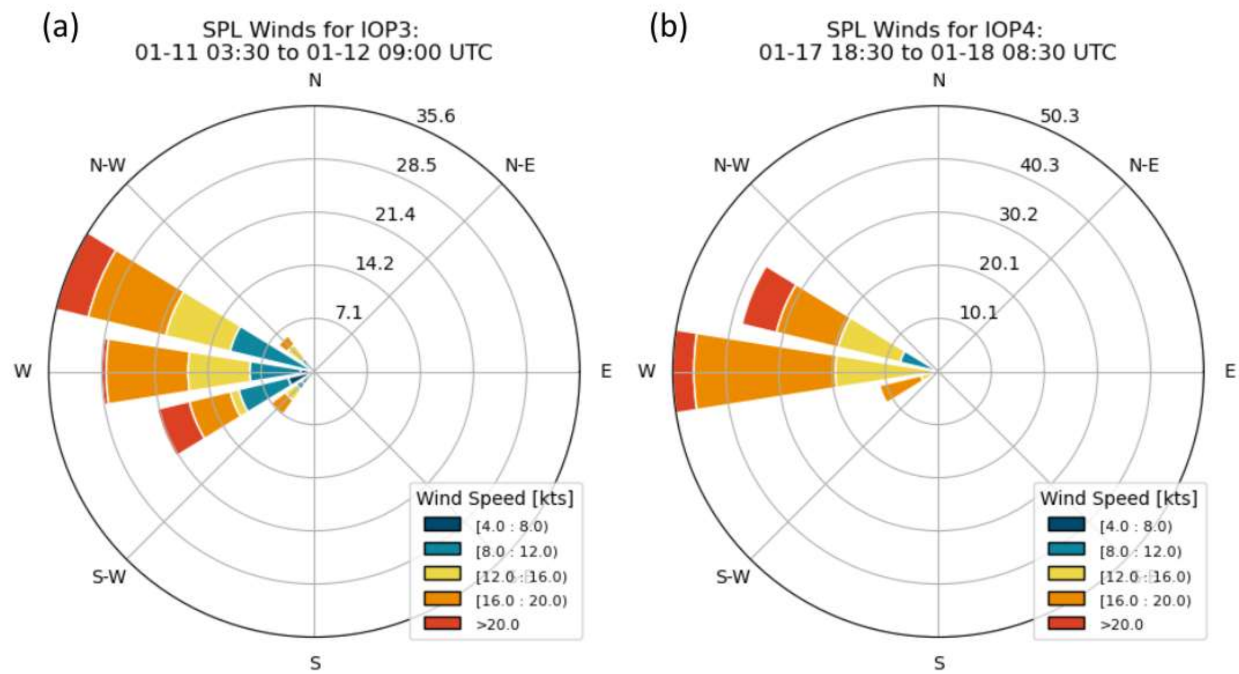

Figure 3.9: Wind roses depicting the direction and strength, in kts, of winds as measured at SPL during precipitation for (a) IOP3 (0330 UTC 11 January 2025 through 0900 UTC 12 January 2025) and (b) IOP4 (1830 UTC 17 January 2025 through 0830 UTC 18 January 2025).

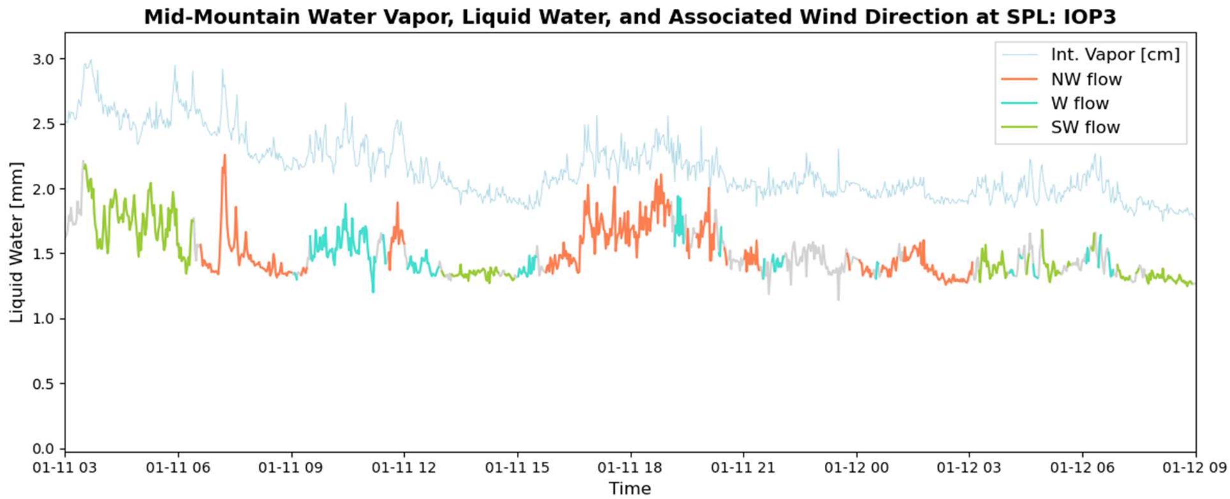

Figure 3.10: Liquid water path in mm (gray line with colors overlaid) and precipitable water vapor in cm (thin blue line) from the mid-mountain MWR for 0330 UTC 11 January 2025 through 0900 UTC 12 January 2025. Colors overlaid indicate time ranges corresponding to *north-westerly*, *westerly*, and *south-westerly* winds at SPL as defined in Section 2.3.1.

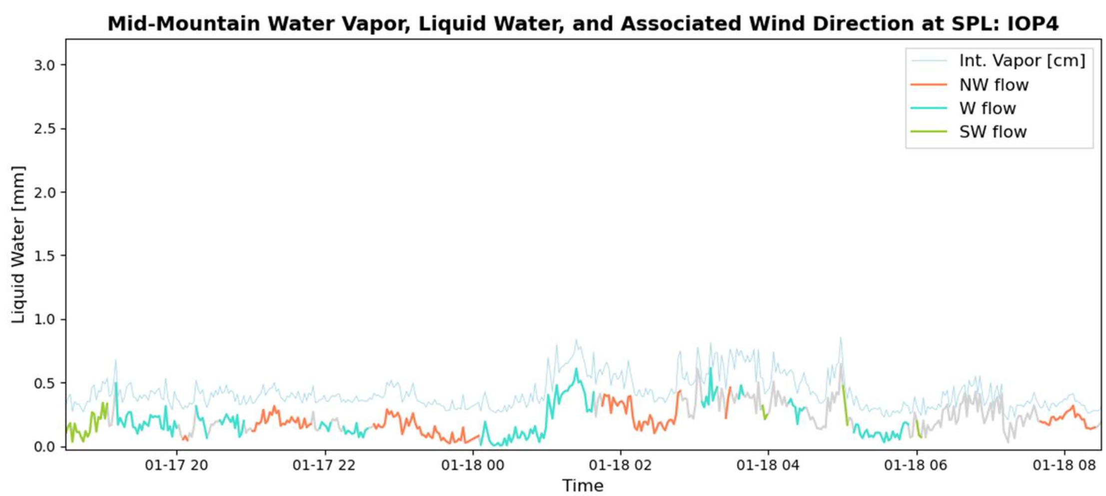

Figure 3.11: As in Figure 3.10, but for 1830 UTC 17 January 2025 through 0830 UTC 18 January 2025.

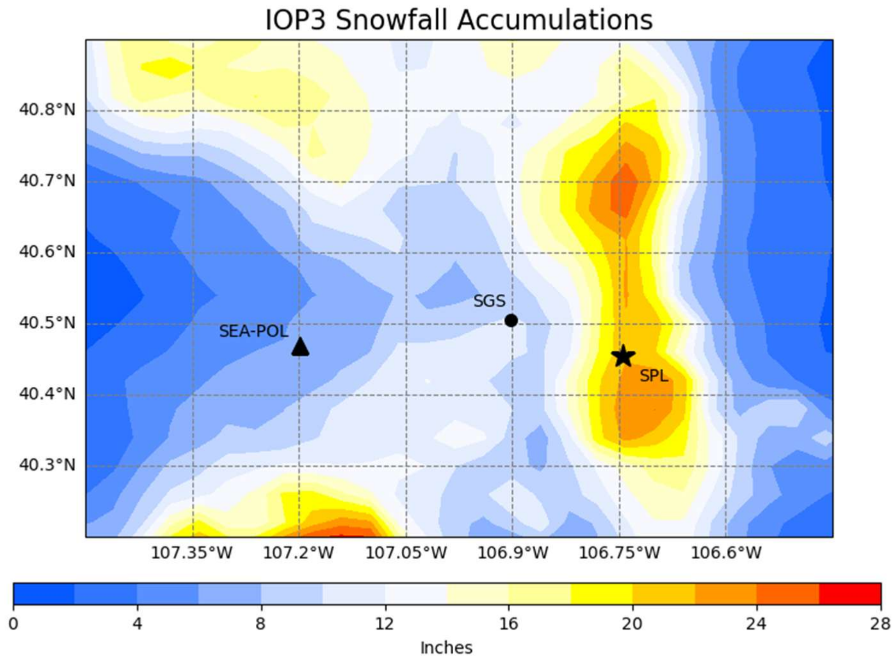

Figure 3.12: Snowfall accumulations in inches from the NOAA National Gridded Snowfall Analysis for the 48-hour period ending on 1200 UTC 12 January 2025. Black star indicates the location of SPL; black circle indicates the location of SGS; black triangle indicates the location of SEA-POL.

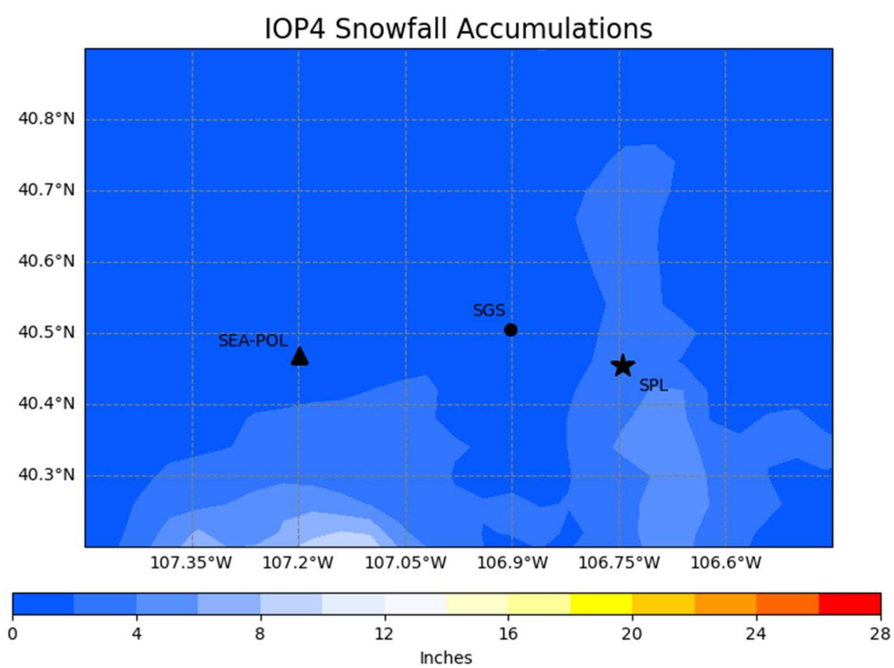

Figure 3.13: As in Figure 3.12, but for the 48-hour period ending on 1200 UTC 18 January 2025.

Chapter 4

Radar Echo Variations with Moisture and Flow

IOP3 and IOP4 are associated with different magnitudes of moisture transport (Fig. 3.2; 3.5), as well as different local wind patterns. These distinctions manifest as differences in the accumulation and distribution of snowfall (Fig. 3.12; Fig. 3.13), where accumulations from IOP3, which is associated with greater IVT and more variable winds than observed during IOP4, are greater and more widespread. However, there is variation in local moisture availability and flow regime throughout the two IOPs (Fig. 3.10; Fig. 3.11). To fully assess the impact of moisture and flow on snowfall during these cases, an in-depth look into how the cloud structure and microphysical characteristics differ between the IOPs and between different local flow conditions is necessary.

4.1 Impact on Precipitating Cloud Structure

To assess how the differences in IVT between the two cases impact precipitating cloud depth, probability density functions of *echo-top heights*, the highest altitudes in which a reflectivity of 10 dBZ is reached along the length of each RHI scan, are created for the duration of IOP3 and IOP4 and are overlaid (Fig. 4.1). The distribution of precipitating cloud depth, as indicated by the echo top heights of east-facing SEA-

POL RHIs, is wider for IOP3 than for IOP4, hinting at the presence of greater variability in precipitating cloud depth as well as deeper precipitating clouds during IOP3 (Fig. 4.1). In IOP3, precipitating cloud depths range from 2.25 to nearly 8 km AMSL (Fig. 4.1). In IOP4, precipitating cloud depths range from 2.25 to near 6 km AMSL (Fig. 4.1). The mean precipitating cloud depth is around 4.20 km AMSL and 3.97 km AMSL during IOP3 and IOP4, respectively (Fig. 4.1). The median precipitating cloud depth is similar, but greater for each IOP: around 4.25 km AMSL and 4.00 km AMSL during IOP3 and IOP4, respectively (Fig. 4.1). The echo-top heights are generally greater for the high-moisture case (IOP3), but the strength of precipitation within the cloud is not depicted. Therefore, it is of interest to assess full reflectivity distributions with height. The wider distribution in depth associated with IOP3 (Fig. 4.1) may also be connected to the greater variability in wind direction at SPL during that case (Fig. 3.9), which warrants further division by flow regime to assess the impact of flow direction on the snowfall characteristics.

Because persistent south-westerly flow at SPL occurred infrequently during IOP4 (see Fig. 3.9, 3.11), the impact of flow in IOP3 and IOP4 is assessed with a focus on north-westerly and westerly flow. Both IOP3 and IOP4 contain periods of north-westerly and westerly flow, but the extent of orographic influence may differ between these regimes, particularly near the terrain around SPL, which appears cross-barrier to north-westerly winds (Fig. 2.1). Differing orographic influence could result in different distributions of reflectivity, which is indicative of snow particle size and precipitation intensity, beyond what is discussed in relation to echo-top height distributions. Furthermore, differing extent of the various snow growth processes can be indicated through distributions of Z_{DR}, which is more positive for more horizontally elongated hydrometeors, thus providing an inference of resulting snow characteristics.

During periods with westerly and north-westerly winds at SPL, maximum reflectivity values near 25 to 30 dBZ are located primarily from the surface to 4 km AMSL in IOP3 (Fig 4.2a, b). In IOP4, maximum reflectivity values near 25 to 30 dBZ during these flow regimes are elevated, located primarily above the surface from 3 to 4 km AMSL (Fig. 4.2c, d). The most positive Z_{DR} values (> 0.5 dB) are present predominately between 4.5 and 2.5 km AMSL during westerly and north-westerly flow in IOP3 (Fig 4.2a, b), while maximum values are reached higher aloft, 3 through 5.5 km AMSL, during westerly and north-westerly flow in IOP4 (Fig 4.2c, d). The majority of Z_{DR} values range from a minimum of -0.5 dB to maximum near 2.0 dB (Fig 4.2a, b) or 3.5 dB (Fig 4.2c, d) during westerly and north-westerly flow in IOP3 and IOP4, respectively.

Westerly flow at SPL during IOP3 features a pattern of slight increasing Z_h from 0 to 8 dBZ from the top of the precipitating cloud, around 6.5 km AMSL, to 4.5 km AMSL that is associated with near-zero Z_{DR} through the same altitude ranges (Fig. 4.2a). This pattern is a singular growth mode similar to what is expected of an increase in size or concentration of small pristine crystals of a mix of ice crystal habits and orientation. From 4.5 to 4 km AMSL, Z_{DR} values greatly increase from 0 to 1-1.5 dB, as Z_h nears 15 dBZ, which could be due to depositional growth (Fig. 4.2a). Just below 4 km AMSL, Z_{DR} values decrease towards 0.25 dB with decreasing altitude as reflectivity magnitudes increase substantially with decreasing altitude – reaching the maximum values of around 25 dBZ (Fig. 4.2a) – a signature generally associated with aggregation. Below 3.5 km, there is little change to reflectivity values, but Z_{DR} values continue decreasing towards 0 dB (Fig. 4.2a). This pattern may be due to increasingly random orientation of aggregated particles, or growth by aggregation or riming. There is also an increase in spread of reflectivity values below 4 km AMSL as Z_{DR} decreases (Fig. 4.2a), suggesting that snow particle size near the surface (below 4 km AMSL) is driven by the extent of further growth of pristine particles by aggregation or riming.

During north-westerly flow in IOP3, the precipitating cloud depth where reflectivity values are greater than 0 dBZ reaches above 7.75 km AMSL (Fig. 4.2b) – a much deeper profile than was associated with westerly flow (Fig. 4.2a). IOP3 north-westerly flow also features a wide spread of reflectivity values above 4.5 km AMSL (Fig. 4.2b), suggesting no prominent singular growth mode aloft. However, Z_{DR} values above 4.5 km are largely greater than 0 dB during this regime in IOP3 (Fig. 4.2b), indicating more horizontally-oriented particles aloft. Between 3.5 and 4.5 km, there are two reflectivity frequency hotspots visible in Figure 4.2b: a high magnitude hotspot, around 0-10 dBZ, and a low magnitude hotspot, around 20 dBZ. During north-westerly flow, there is also a more even spread in reflectivity values between 0 and 28 dBZ below 3.25 km AMSL than was seen during westerly flow (Fig. 4.2b; Fig. 4.2a), while Z_{DR} values are most concentrated around 0 to 0.25 dB at these altitudes

(Fig. 4.2b). This pattern suggests a greater variety in the extent of snow growth by riming or aggregation during north-westerly flow, either due to spatial heterogeneity in snow growth processes or temporal differences in patterns of snow growth, than was present during periods of westerly flow. Z_{DR} values also reach higher magnitudes, the maximum being near 2 dB, from 3 to 5 km AMSL, while still being near 0 dB towards the surface (Fig. 4.2b), indicating that north-westerly flow in IOP3 includes moments of particularly efficient snow growth through aggregation or riming of initially more horizontally-oriented particles.

During westerly flow in IOP4, maximum cloud depth of reflectivity values greater than 0 dBZ is around 6.25 km AMSL (Fig. 4.2c). There is one dominant mode of snow growth from around 4.5 to 4 km visible in Figure 4.2c. Here, Z_h increases from around 3 to 8 dBZ with decreasing height. This increase in reflectivity corresponds to heights where there is a slight increase in Z_{DR} values from -0.5 to 0.5 dB, to a range of around -0.25 to 0.75 dB (Fig. 4.2c), which could be attributed to the growth of small, randomly oriented pristine particles to slightly larger crystals. From 4 to 3.5 km AMSL, there is a slight increasing trend in Z_h from 10 to 18 dBZ, corresponding to Z_{DR} values approaching 0 dB (Fig. 4.2c), which corresponds to further growth of snow particles by aggregation or riming. Like in IOP3, there is an increase in spread of reflectivity values at low levels, below 3.75 km AMSL, as Z_{DR} decreases (Fig. 4.2c), suggesting that snow particle size near the surface is driven by the extent of further growth of pristine particles by aggregation or riming.

During north-westerly flow in IOP4, the precipitating cloud depth, or altitude of reflectivity values greater than 0 dBZ, is similar to that during westerly flow (Fig. 4.2d). Like in IOP3, there appears to be two reflectivity frequency hotspots: a low magnitude hotspot of around 5 dBZ centered just below 4 km AMSL, and a high magnitude hotspot of around 8 to 15 dBZ centered around 4.5 km AMSL (Fig. 4.2d). The frequency hotspots correspond to heights of relatively high Z_{DR} magnitudes, around 0 to 3.5 dB, while reflectivity values increase and Z_{DR} values decrease at altitudes beneath – particularly below 3.25 km AMSL (Fig. 4.2d). This pattern suggests that the frequency hotspots during IOP4 north-westerly flow are associated with more pristine or horizontally-oriented snow particles than observed at altitudes closer to the surface. There is also a greater spread in Z_h below 4.5 km AMSL during north-westerly flow than during westerly flow in IOP4, while Z_{DR} values vary minimally – are concentrated near 0 dB – closer to the surface (Fig. 4.2d). The increased spread in reflectivity values below 4.5 km AMSL during north-westerly flow could correspond to differences in whether or not growth is dominated by vapor deposition: with the low reflectivity values between -10 to 10 dBZ indicating small particles that are pristine enough to contribute to high (> 0.5 dB) Z_{DR} signatures aloft but infrequently make it to the surface, and the greater Z_h signatures, nearing 20 dBZ, indicating larger particles that do reach altitudes below 3 km AMSL, but are aggregated or rimed to result in the concentrated near-0 dB Z_{DR} signatures close to the surface.

4.2 Impact on Microscale Properties

While different modes of reflectivity, and associated Z_{DR} patterns, are visible in the north-westerly histograms from those in the westerly histograms and seem to differ between IOP, large-scale forcing (Fig. 3.1; Fig. 3.4) and local temperature profiles (Fig. 3.7; Fig. 3.8) have been noted to vary between the IOPs, along with local moisture availability within (Fig. 3.10; Fig. 3.11). Therefore, context of temperature and moisture, or supersaturation, is necessary to attribute the observed trends in reflectivity and Z_{DR} with altitude to specific microphysical characteristics and processes. In the following section, histograms taking further environmental context into account, using WRF temperature, q_v, and RH_i matched to SEA-POL RHIs as the y-axis of the distributions, are analyzed to more concretely assess the connection between the observed patterns in Z_h and Z_{DR} to microphysical characteristics and processes.

During times of westerly flow in IOP3, reflectivity values are concentrated between -10 and -20 °C (Fig. 4.3a). As seen in Figure 4.3a, Z_h notably increases with increasing temperature for temperatures warmer than around -20 °C: from about 5 to 25 dBZ between -20 and -8 °C. Reflectivity values above 15 dBZ occur most frequently at temperatures warmer than -14 °C, indicating dominant growth by either riming or aggregation. Z_{DR} values peak around -15 °C, which is indicative of depositional (horizontally oriented, potentially dendritic) growth, and the majority of the increase in reflectivity occurs between -15 and -12 °C as Z_{DR} values rapidly decrease to 0 dB with increasing temperature (Fig. 4.3a), suggesting that the dominant snow growth process associated with the snow growth mode noted in section 4.1 for IOP3 westerly flow is aggregation. However, reflectivity values increase from 20 to 25 dBZ at temperatures warmer than -12 °C where Z_{DR} values remain near 0 dB, but reaching slight (> -0.25 dB) negative values, which could suggest that riming is a factor in the most intense precipitation during this regime (Fig. 4.3a). During westerly flow in IOP3, reflectivity values above 10 dBZ are associated with increasing water vapor above 1.5 g/kg, which could indicate that greater moisture is available to create initial pristine particles or to condense into SLW for riming (Fig. 4.3b). However, Z_{DR} values where between 1.5 and 2.25 g/kg q_v are greatly spread, from around -0.25 to 1 dB, as reflectivity values are generally increasing from 10 to 20 dBZ with increasing q_v (Fig. 4.3b). The spread could be indicating snow growth with aggregation in a dendritic growth zone or processes occurring at different times: one where the presence of vapor grows pristine particles through deposition, and one where the vapor is condensed into SLW to grow particles through riming.

During north-westerly flow in IOP3, the aforementioned reflectivity frequency modes (Fig. 4.2b) are temperature dependent: with the low magnitude, 0-10 dBZ, mode corresponding to temperatures around -20 °C, and the high magnitude, around 20 dBZ, mode corresponding to temperatures largely warmer than -16 °C (Fig. 4.3d). The temperature-dependent modes support the inference that high reflectivity during this regime is tied most to riming or aggregation processes at low altitudes. The decreasing Z_{DR} signature with decreasing altitude is most prominent at temperatures warmer than -14 °C (Fig. 4.3d), which is consistent with growth by either riming or aggregation. In IOP3, the trend in reflectivity with q_v is less prominent during north-westerly flow than during westerly flow, particularly for reflectivity values below 15 dBZ (Fig. 4.3e), which suggests a less definitive connection between increasing moisture availability and snow growth.

Because ice crystal habits are linked to supersaturation (Fig. 1.1), assessing the distribution of reflectivity and Z_{DR} with RH_i provides inferences about the complexity of crystals growing through vapor deposition, which impact particle fall speeds as well as aggregation efficiency. In IOP3, the most supersaturated conditions with respect to ice are associated with near 0 dB Z_{DR} during westerly flow (Fig. 4.3c), and either low (0 to 0.5 dB) or high (up to 2.5 dB) Z_{DR} during north-westerly flow (Fig. 4.3f). These relationships suggest more complex pristine crystal habits are present during north-westerly flow in IOP3, in which high Z_{DR} is present largely at 5 to 15% supersaturations with respect to ice (Fig. 4.3f). These values correspond to habits ranging from tabular to branched at the temperatures which correspond to those Z_{DR} values in IOP3 (between -8 and -22 °C; Fig. 4.3b). There is also a greater spread in reflectivity values observed within subsaturated conditions with respect to ice during north-westerly flow (Fig. 4.3f) than during westerly flow (Fig. 4.3c) in IOP3. In particular, reflectivity values in subsaturated conditions with respect to ice reach greater than 10 dBZ (Fig. 4.3f) which is not observed during westerly flow (Fig. 4.3c).

In IOP3, the two reflectivity modes observed during north-westerly flow are most associated with differences in temperature. Moderate to high moisture availability indicated by q_v is associated with the high Z_{DR} signatures during westerly flow, while those during north-westerly flow are spread out among the whole range of simulated values. In addition, both greater supersaturations associated with reflectivity values less than 10 dBZ, and greater subsaturations associated with reflectivity values greater than 10 dBZ are noted during north-westerly flow – which would be expected to be the case in IOP4 as well since there was an increase in reflectivity and Z_{DR} variability for north-westerly flow (Fig. 4.2). However, the two reflectivity modes associated with north-westerly flow may not be tied to differences in temperature in IOP4 since the separation of the modes was less distinct (Fig. 4.2).

During westerly flow in IOP4, reflectivity increases from -2 to 18 dBZ with increasing temperature from -24 to -12 °C (Fig. 4.4a). The trend of decreasing Z_{DR} with decreasing altitude is prominent at temperatures warmer than -16 °C (Fig. 4.4a), which aligns with potential production of small aggregates within or just below regions of depositional growth. Below -10 °C, Z_{DR} values remain near-zero, but reach slightly negative, while the spread in reflectivity is substantial (Fig. 4.4a). This result does not suggest one dominant path of snow growth at low altitudes, but could be attributed to rimed aggregates. As expected, and observed during IOP3, increasing Z_h beyond 10 dBZ is associated with increasing q_v above 1.5 g/kg (Fig. 4.4b). However, there are two extents of q_v magnitudes associated with 0.5 dB or greater Z_{DR}: both lower, around 1 g/kg, and higher, around 1.5 to 1.75 g/kg, magnitudes (Fig. 4.4b). Supersaturations with respect to ice reach greater values, and greater instances of high reflectivity values are associated with low RH_i conditions, during westerly flow in IOP4 than was observed for the same flow regime in IOP3 (Fig. 4.4c). The greater supersaturations suggest a larger presence of branched crystals growing through vapor deposition (Fig. 1.1). High reflectivity associated with low RH_i conditions could be indicative of snow growth concentrated aloft, with large hydrometeors falling into subsaturated conditions, further growth through aggregation occurring as these hydrometeors fall, or turbulent motions moving hydrometeors between subsaturated and supersaturated regions.

During north-westerly flow in IOP4, there is a notable 0-15 dBZ mode located in temperatures between -17 and -23 °C and associated with near-zero Z_{DR} (Fig. 4.4d). At warm temperatures, at and below a second relative Z_{DR} peak reaching 1.5 dB around -12 °C, reflectivity magnitudes are either high, near 20 dBZ, or low, from -10 to 10 dBZ (Fig. 4.4d). Figure 4.5e reveals that the low magnitude reflectivity is either associated with low q_v around 0.5 to 1.0 g/kg, or higher values between 1.5 and 2 g/kg. All Z_{DR} values above 0.75 dB are associated with q_v between 1.5 and 2 g/kg (Fig. 4.4e) and temperatures between -12 to -18 °C (Fig. 4.4d) and could thus be attributed to a period of efficient growth by vapor deposition. The supersaturations with respect to ice associated with these high Z_{DR} values also reach large magnitudes, 15 to 20% (Fig. 4.4f), signifying the presence of complex branched crystals such as dendrites. Unlike in IOP3, there are notably less instances of substantially subsaturated (< 90% RH_i) conditions contributing to high reflectivity signatures during north-westerly flow (Fig. 4.4f) compared to westerly flow (Fig. 4.4c). This result suggests a different microphysical growth process is contributing to the largest crystals during north-westerly flow than that during westerly flow in IOP4.

4.3 Microscale Processes and Variability

A wide variety of microphysical characteristics are observed during both westerly and north-westerly flow in IOP3 and IOP4. However, it is uncertain whether the variability observed is tied to temporal variability, given the changing conditions through each IOP and flow regime (e.g., Fig. 3.10, 3.11), or spatial variability given that the RHIs included in figures from Section 4.2 cover 60 km from SEA-POL with changes in elevation towards SPL (e.g., Fig. 2.1), or a combination of both given how the direction and moisture content of flow can impact how, or to what extent, snowfall processes are modified by terrain. To investigate the variability in inferred characteristics as they relate to different environmental factors and microphysical processes, select RHIs from SEA-POL representative of patterns observed throughout north-westerly and westerly flow during IOP3 and IOP4, with WRF variables (temperature, q_v, q_c, and 2D winds) overlaid, are discussed in this section.

4.3.1 IOP3 Westerly and North-Westerly Flow

At 1355 UTC 11 January 2025, during the IOP3 westerly flow regime and ahead of the short-wave passage (Fig. 3.1), the mid-mountain MWR does not indicate a relative peak in liquid water or water vapor (Fig. 3.10), but the WRF cross-section profile suggests there are relatively high (> 2.5 g/kg) q_v values concentrated in temperatures warmer than -12 °C and at altitudes below the top of the nearby terrain barrier located around -107° longitude (Fig. 4.5a). At this time, reflectivity values reaching 25 dBZ are present at low elevations near the radar (west of -106.95° longitude), within temperatures warmer than -16 °C, as well as at high elevations near the terrain (east of -106.85° longitude), within temperatures reaching -20 °C (Fig. 4.5b). The high reflectivity values near the radar correspond to near 0 dB Z_{DR} (Fig. 4.5c). The temperature range, reflectivity values, and Z_{DR} signature near the radar at this time are indicative of snow growth dominated by aggregation.

The high reflectivity values near the terrain correspond to high Z_{DR} values above 1.5 dB between -16 and -22 °C, decreasing to values near 0.5 dB within the spot of enhanced reflectivity (Fig. 4.5c). This signature is more indicative of snow growth through the riming of pristine crystals, but aggregation could still be contributing to the radar signatures. The high reflectivity values near terrain are also within a region of positive WRF-simulated q_c – suggesting the presence of SLW and supporting the inference that riming contributes to precipitation intensity at this location (Fig. 4.5b). There is also a strip of reflectivity values near 15 dBZ around 5 km AMSL (Fig. 4.5b) that is associated with 0.5 to 1.0 dB Z_{DR} (Fig. 4.5c) and vertical wind shear (Fig. 4.5e). The thin cloud of moderately enhanced reflectivity may thus consist of small pristine particles that grow by depositional growth and riming from SLW present over the terrain. This inference of a potential seeder-feeder mechanism is supported by decreased correlation coefficients below 0.98 present over the terrain (Fig. 4.5d).

In IOP3 from 0930 to 1100 UTC 11 January 2025, during westerly flow and ahead of the shortwave passage (Fig. 3.1), but near maximum IVT (Fig. 3.2), there is a relative peak in mid-mountain integrated water vapor and liquid water (Fig. 3.10). At 1009 UTC 11 January 2025, the presence of SLW, as inferred through the presence of WRF q_c, is associated with some near-zero Z_{DR} values which indicates riming near the terrain east of -106.8° longitude (Fig. 4.6). At this time, west of -106.8° longitude, high reflectivity values are located in a region of near-zero Z_{DR} just below a region of high Z_{DR} around 1.5 to 1.7 dB (Fig. 4.6b; Fig. 4.6c). Here, snow growth is likely dominated by aggregation. The reflectivity enhancement at this time is less intense and more heterogeneous than was seen in Figure 4.5 and is largely constrained within temperatures warmer than -14 °C, with the exception of cloud-top generating cells located from 4 to 6 km AMSL (Fig. 4.6b). At this time, the reflectivity values are slightly greater west of -106.8° longitude, east of which is the primary terrain barrier where WRF q_c values are greater (Fig. 4.6b). Therefore, riming is likely not a substantial contributor to snow growth at this time.

At 0720 UTC 11 January 2025, during north-westerly flow in IOP3, near maximum IVT (Fig. 3.2), weaker absolute vorticity than associated with the previous examples (Fig. 3.1), and a relative peak in on-mountain integrated liquid water and water vapor (Fig. 3.10), a 5 km AMSL deep precipitating cloud constrained within a region of high, greater than 2 g/kg, q_v and temperatures warmer than -14 °C is present (Fig. 4.7b, a). A layer of enhanced WRF q_v near 2.9 g/kg, just below a region of relatively high (> 3 dB) Z_{DR} is present at this time (Fig. 4.7a, c). Below this enhancement are reflectivity values around 20 dBZ where Z_{DR} is near 0 dB. While there is some heterogeneity in this pattern, the consistent low-elevation near-0 dB Z_{DR} values at temperatures warmer than -12 °C and lack of modeled SLW suggest snow growth is being driven by widespread aggregation at this time. During north-westerly flow in IOP3 at 1957 UTC 11 January 2025, near the time of shortwave passage and maximum absolute vorticity (Fig. 3.1), but past times of high IVT (Fig. 3.2), there is also a relative peak in MWR-retrieved liquid water and water vapor (Fig. 3.10), but WRF q_v is constrained to low altitudes below the main terrain peak and temperatures warmer than -12 °C (Fig. 4.8a). This time corresponds to relatively high SLW, as suggested by the presence of WRF q_c magnitudes approaching 0.2 g/kg, on the western edge of a terrain barrier (from around -106.65° to -106.8° longitude) directly outlining an area of high Z_h around 25 dBZ reaching from -10 to -20 °C (Fig. 4.8b). Z_{DR} values are below 0.5 dB where the highest reflectivity values are located (Fig. 4.8c), and ρ_{HV} is smaller (< 0.98) across the terrain (Fig. 4.8d). Here, high reflectivity reaching into cold temperatures (-20 °C) is not a function of the q_v present within those temperatures. Furthermore, while the relative peak in MWR-retrieved liquid water and water vapor is lower, and the precipitating cloud is shallower and less widespread, reflectivity values are substantially greater over terrain at 1957 UTC 11 January 2025 (Fig. 4.8) than was observed in the 0720 UTC 11 January 2025 RHI (Fig. 4.7).

The signatures observed in the noted RHIs do not stray from patterns inferred from the histograms, but similar signatures did not always indicate the same snow growth processes were occurring. For example, similar enhancements in Z_{DR} around 4 km and -14 to -16 °C during westerly flow in IOP3 (as noted in Fig. 4.2, Fig. 4.3a) were associated with stratiform depositional growth in Figure 4.6 and orographic enhancement near terrain in Figure 4.5. Furthermore, the high reflectivity magnitude mode associated with temperatures around -14 °C during north-westerly flow (Fig.

4.3d) is tied to orographic enhancement and riming in Figure 4.8, but deep, widespread precipitation and aggregation in Figure 4.7.

4.3.2 IOP4 Westerly and North-Westerly Flow

Like in IOP3, a variety of microphysical characteristics were observed, including inferences of characteristics associated with depositional growth and aggregation or riming, during both westerly and north-westerly flow in IOP4. In IOP4, north-westerly flow exhibited particularly compelling signatures of depositional growth (Fig. 4.4d, e), as well as two modes of similarly frequent low (below 10 dBZ) and high (near 20 dBZ) reflectivity magnitudes within temperatures warmer than -14 °C (Fig. 4.4d). This section explores the observed microphysical processes attributed to the variability in the histogram signatures noted in Section 4.2, like in Section 4.3.1, with particular interest in exploring whether the frequent variety in signatures across flow regimes in IOP4 (Fig. 4.4) corresponds to a spatial separation in snow growth processes influenced by the topography, or not.

At 0136 UTC 18 January 2025, during westerly flow, maximum absolute vorticity (Fig. 3.4), and a relative peak in on-mountain liquid water and water vapor (Fig. 3.11), but past the time of maximum IVT (Fig. 3.5), relatively large reflectivity values near 30 dBZ are present at and below 4 km AMSL (Fig. 4.9b). At this time, WRF q_v magnitudes greater than 2 g/kg, but slightly smaller than those noted in the IOP3 examples, are fairly evenly distributed below 4 km AMSL and in a region of temperatures warmer than -14 °C (Fig. 4.9a, b). Associated Z_{DR} values are near 0 dB below 4 km AMSL, and high, between 1.1 and 1.7 dB, at and just above 4 km AMSL (Fig.

4.9c). The noted RHI signature suggests snow growth primarily through aggregation at this time. However, further enhancement due to riming near terrain is plausible, as the higher elevations (from around -106.65° to -106.8° longitude) is where the WRF-suggested presence of SLW reaches to the surface, ρ_{HV} dips near and below 0.98, and the reflectivity on the western side of the terrain appears enhanced (Fig. 4.9a, d, b). Furthermore, WRF output suggests SLW at cloud top, around the altitude of peak Z_{DR}, across the horizontal, which could be enhancing depositional growth through the WBF since Z_{DR} is highly positive (> 1.5 dB) and in a region around -15 °C at the same location as widespread SLW.

At 2349 UTC January 17 2025, during a moment of north-westerly flow and minimal on-mountain water vapor and liquid water (Fig. 3.11), just after the time of maximum IVT (Fig. 3.5) but at a time of deep conditional instability (Fig. 3.8), reflectivity values between 12 and 18 dBZ and Z_{DR} values between 1.1 and 1.7 dB are present beneath cloud-top generating cells (Fig 4.10). According to the modeled q_v, the present moisture is distributed through an altitude of 4 km AMSL (Fig. 4.10a). The presence of cloud-top generating cells is suggested by the presence of WRF q_c, or SLW, relatively enhanced reflectivity values, greater than 6 dBZ in this case, and associated near-0 dB Z_{DR} (Fig. 4.10b, c). The generating cells are located at the edge of a q_v gradient (Fig. 4.10a), atop a shear layer (Fig. 4.10e), and within a conditionally unstable region (Fig. 3.8b). For the portion of echo near the radar, west of -106.9° longitude, vapor deposition is likely driving the snow growth. For the portion of echo further from the radar, east of -106.8° longitude, reflectivity values near 15 dBZ reach to the surface of terrain, there is a greater presence of SLW, and ρ_{HV} is reduced compared to those values associated with the near-radar echo (west of -106.9° longitude) – indicating riming could be a greater factor in snow growth. The generating cells noted here may have been a factor in the cloud-top SLW presence noted at 0136 UTC 18 January 2025 (Fig. 4.9).

During north-westerly flow in the beginning of IOP4, near maximum IVT (Fig. 3.5) but ahead of absolute vorticity maxima (Fig. 3.4), at a time with stratified moist layers (Fig. 3.8), there are also moments of relatively high Z_{DR}, reaching greater than 3 dB, in a region of temperatures centered around -12 °C. This signature is observed at 2140 UTC 17 January 2025 (Fig. 4.11). The radar echo at this time is elevated, located from 3 to 4 km AMSL, but constrained within temperatures where q_v is greater than around 1.5 g/kg (Fig. 4.11b, c). Reflectivity values associated with the very high Z_{DR} signature during IOP4 north-westerly flow are largely between -10 and 10 dBZ (Fig. 4.11), indicating a dominant presence of small, pristine crystals.

Like in IOP3, the signatures observed in the noted IOP4 RHIs expand on the characteristics reflected in the corresponding histograms by depicting considerably variable dominant snow growth processes, including within the same flow regime. There were both instances of spatial heterogeneity that likely contributed to the histogram signatures (e.g., Fig. 4.9), as well as substantial temporal variety (Fig. 4.9, 4.10, 4.11).

4.4 Figures

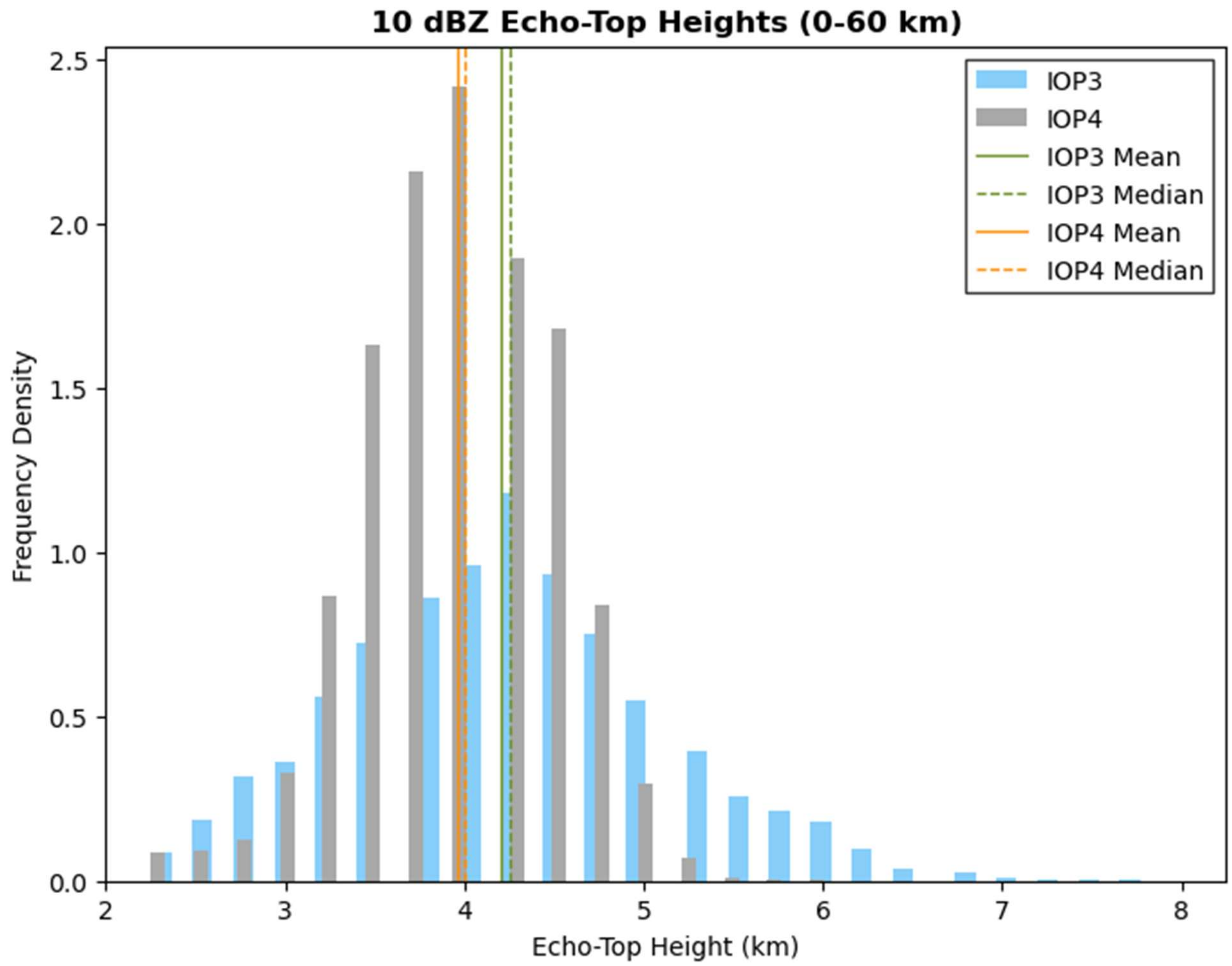

Figure 4.1: Probability density functions of echo-top heights in km AMSL at a 10 dBZ threshold across 0-60 km from the radar in 60-120° SEA-POL RHIs. Light blue bars depict echo-top height distribution for 0330 UTC 11 January 2025 through 0900 UTC 12 January 2025.

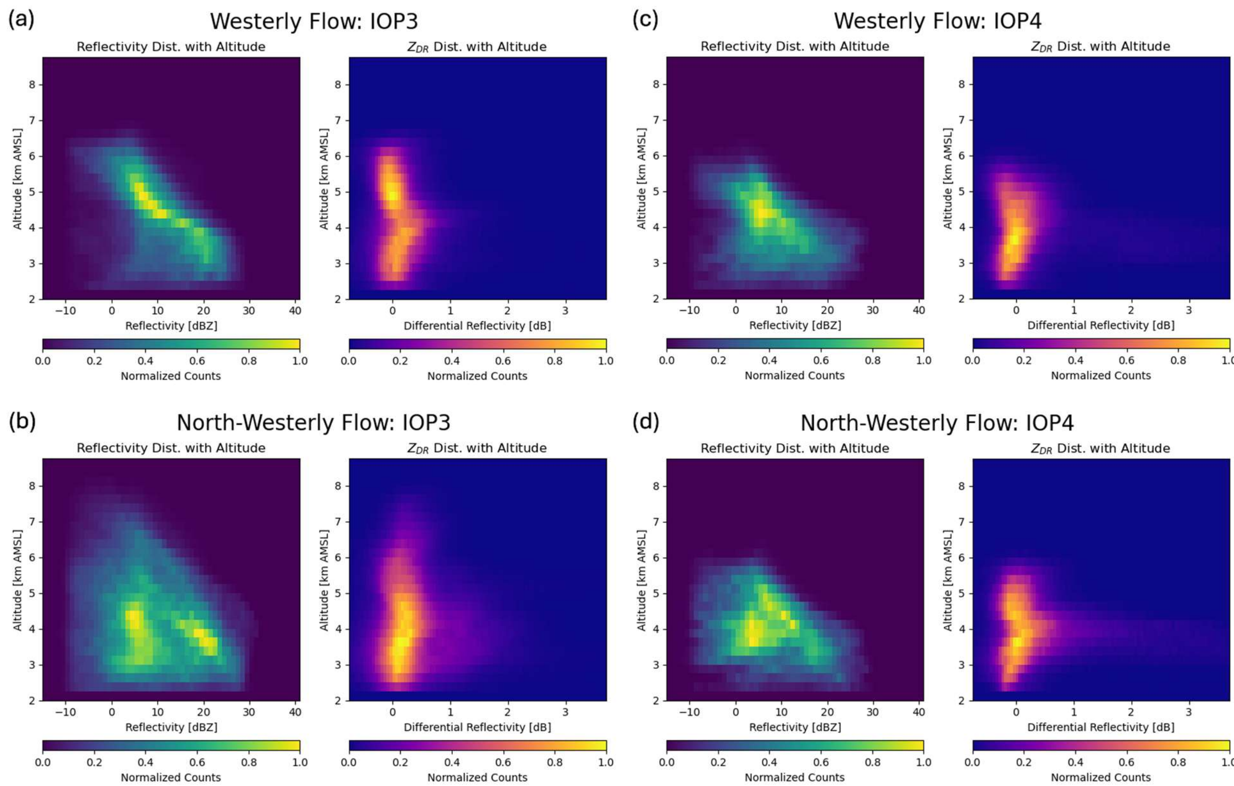

Figure 4.2: 2D histograms of reflectivity in dBZ (left columns) and Z_{DR} in dB (right columns) with altitude in km AMSL from SEA-POL 60-120° RHIs during time ranges corresponding to westerly flow at SPL in (a) IOP3 and (c) IOP4, and during time ranges corresponding to *westerly* flow at SPL in (a) IOP3 and (c) IOP4, and during time ranges corresponding to *north-westerly* flow at SPL in (b) IOP3 and (d) IOP4 as the flow regimes are defined in Section 2.3.1. Histograms are normalized by maximum count in any bin.

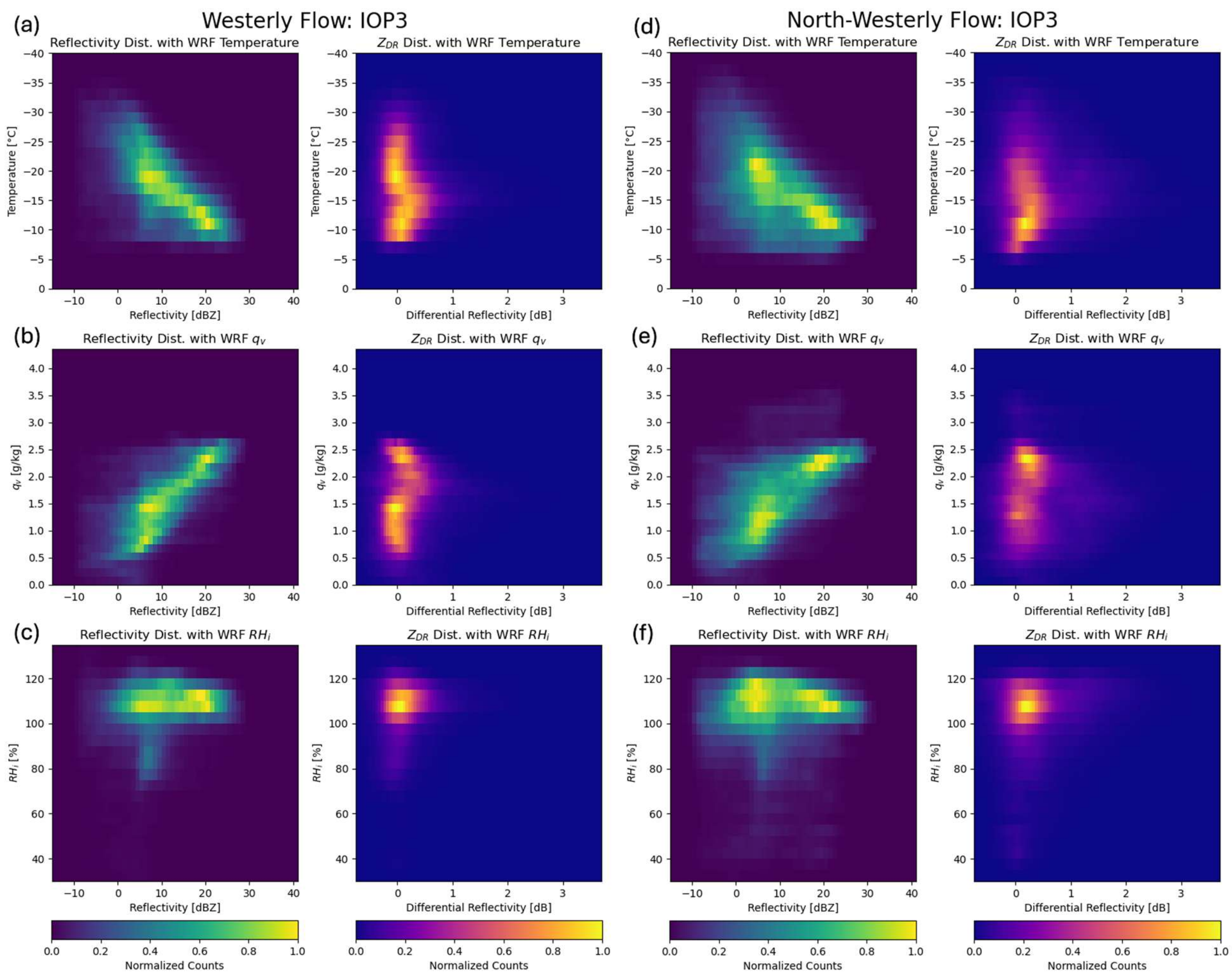

Figure 4.3: 2D histograms of reflectivity in dBZ (left columns) and Z_{DR} in dB (right columns) from SEA-POL 60-120° RHIs with: temperature in °C from WRF for (a) westerly flow and (d) north-westerly flow, q_v in g/kg from WRF for (b) westerly flow and (e) north-westerly flow, and relative humidity with respect to ice in % for (c) westerly flow and (f) north-westerly flow during IOP3. Flow regimes are as defined in Section 2.3.1. Histograms are normalized by maximum count in any bin.

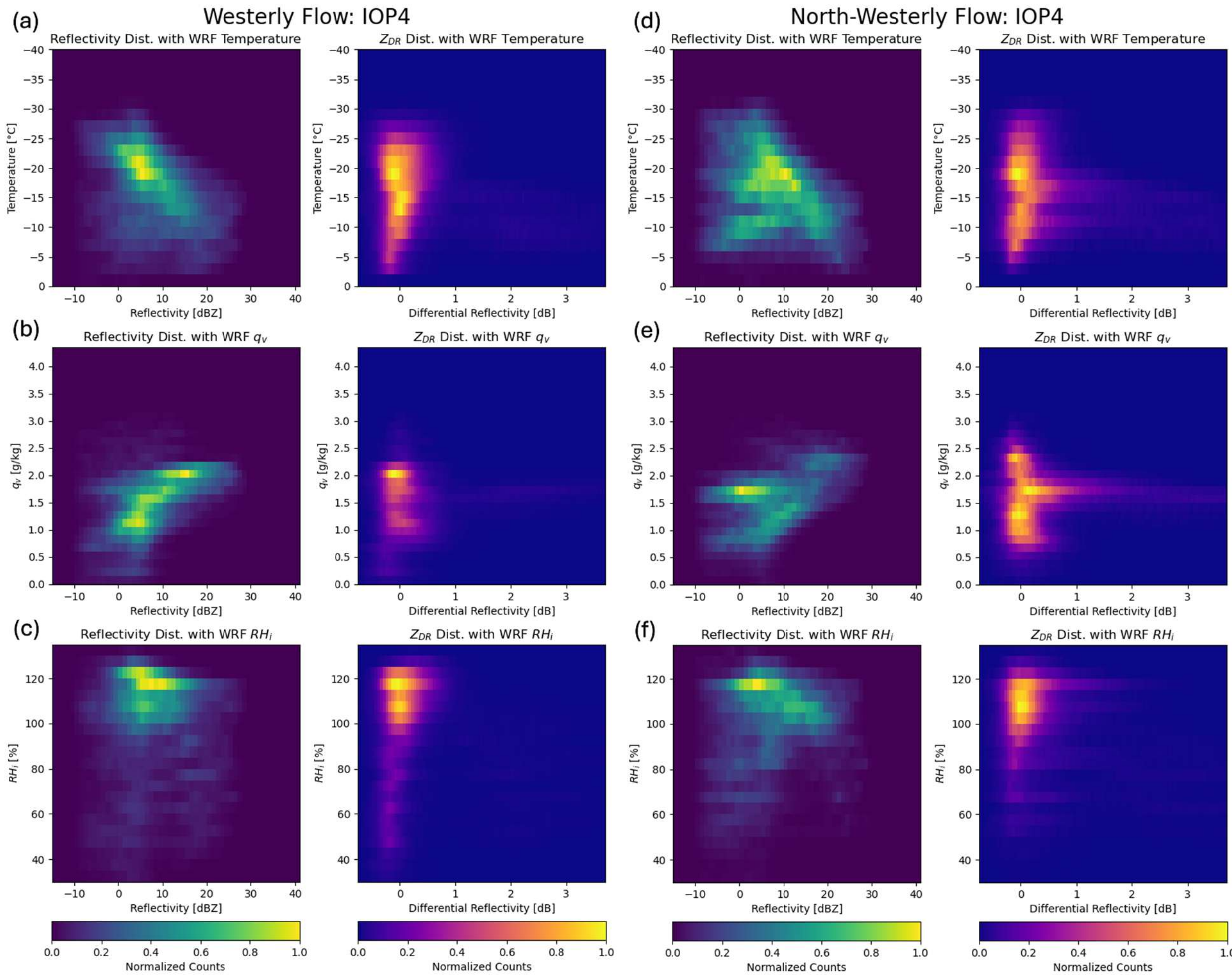

Figure 4.4: As in Figure 4.3, but for IOP4.

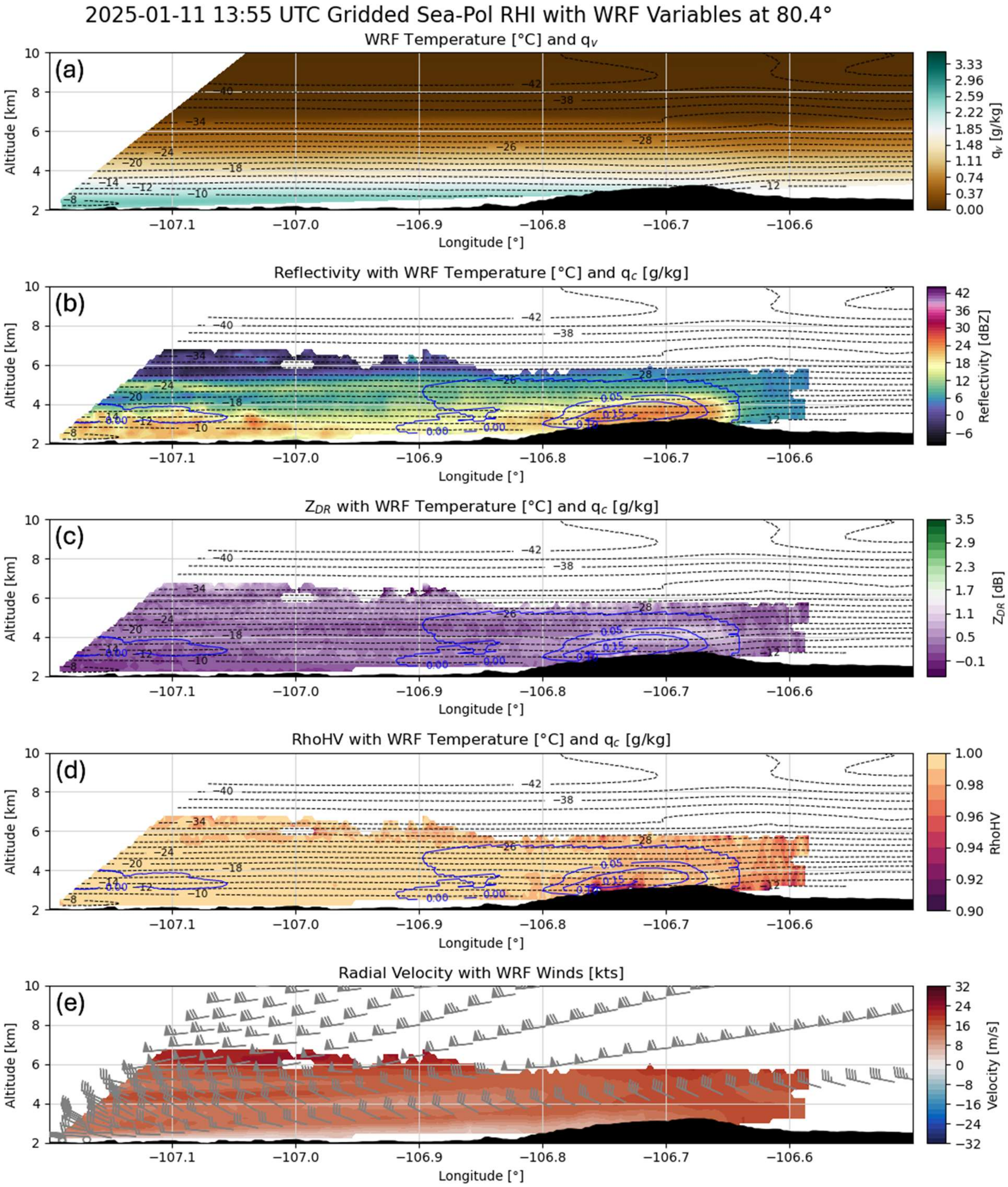

Figure 4.5: SEA-POL 80.4° RHI and environmental context from WRF for 1355 11 January 2025 depicting (a) q_v in g/kg and temperature in °C from WRF, (b) reflectivity in dBZ with WRF temperature in °C and q_c in g/kg overlaid, (c) Z_{DR} in dB with WRF temperature in °C and q_c in g/kg overlaid, (d) ρ_{HV} with WRF temperature in °C and q_c in g/kg overlaid, and (e) radial velocity in m/s with WRF 2D wind barbs in kts overlaid. Filled black contour depicts terrain profile in km from SRTM elevation.

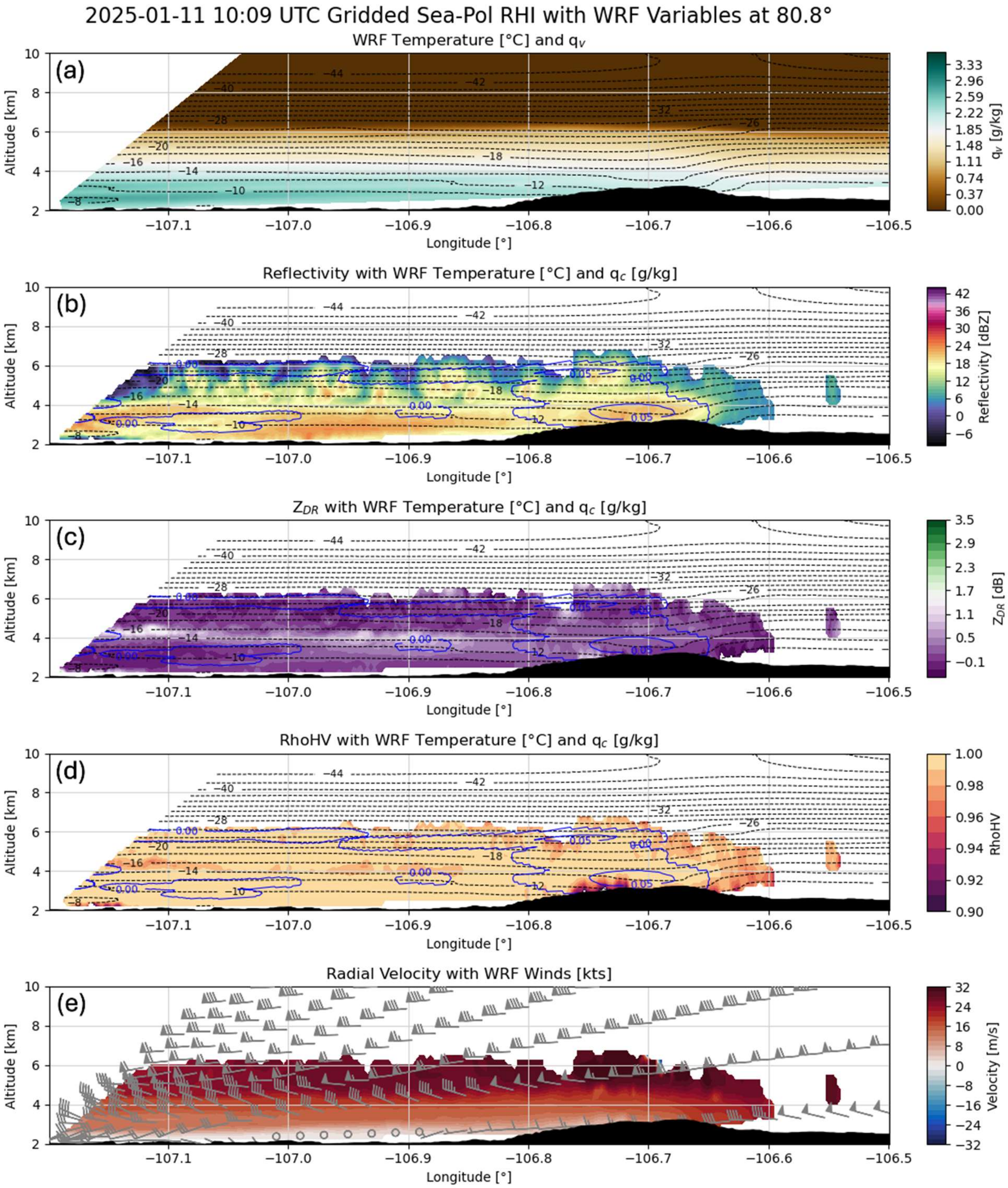

Figure 4.6: As in Figure 4.5, but for 1009 UTC 11 January 2025 and an 80.8° RHI scan.

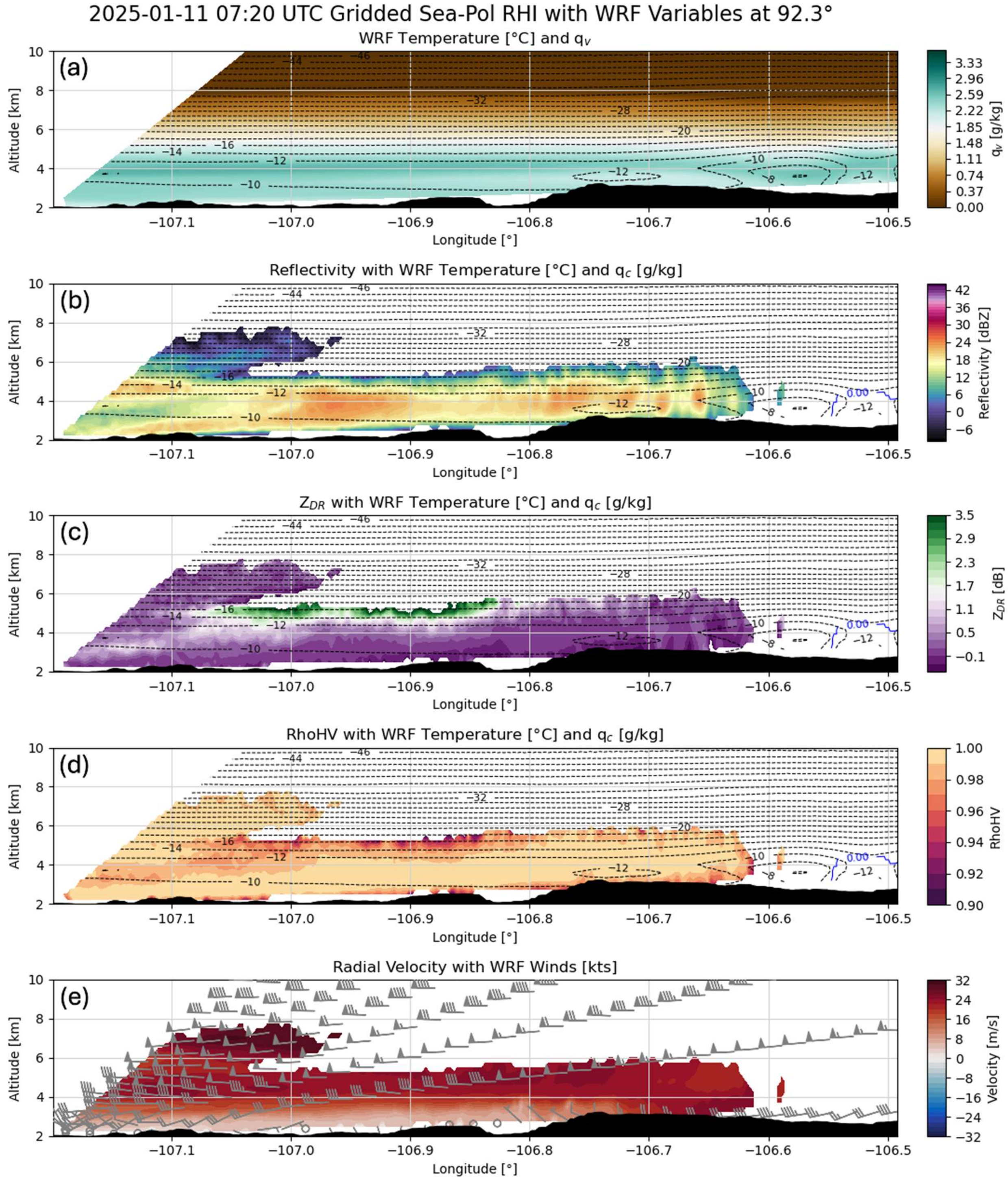

Figure 4.7: As in Figure 4.5, but for 0720 UTC 11 January 2025 and a 92.3° RHI scan.

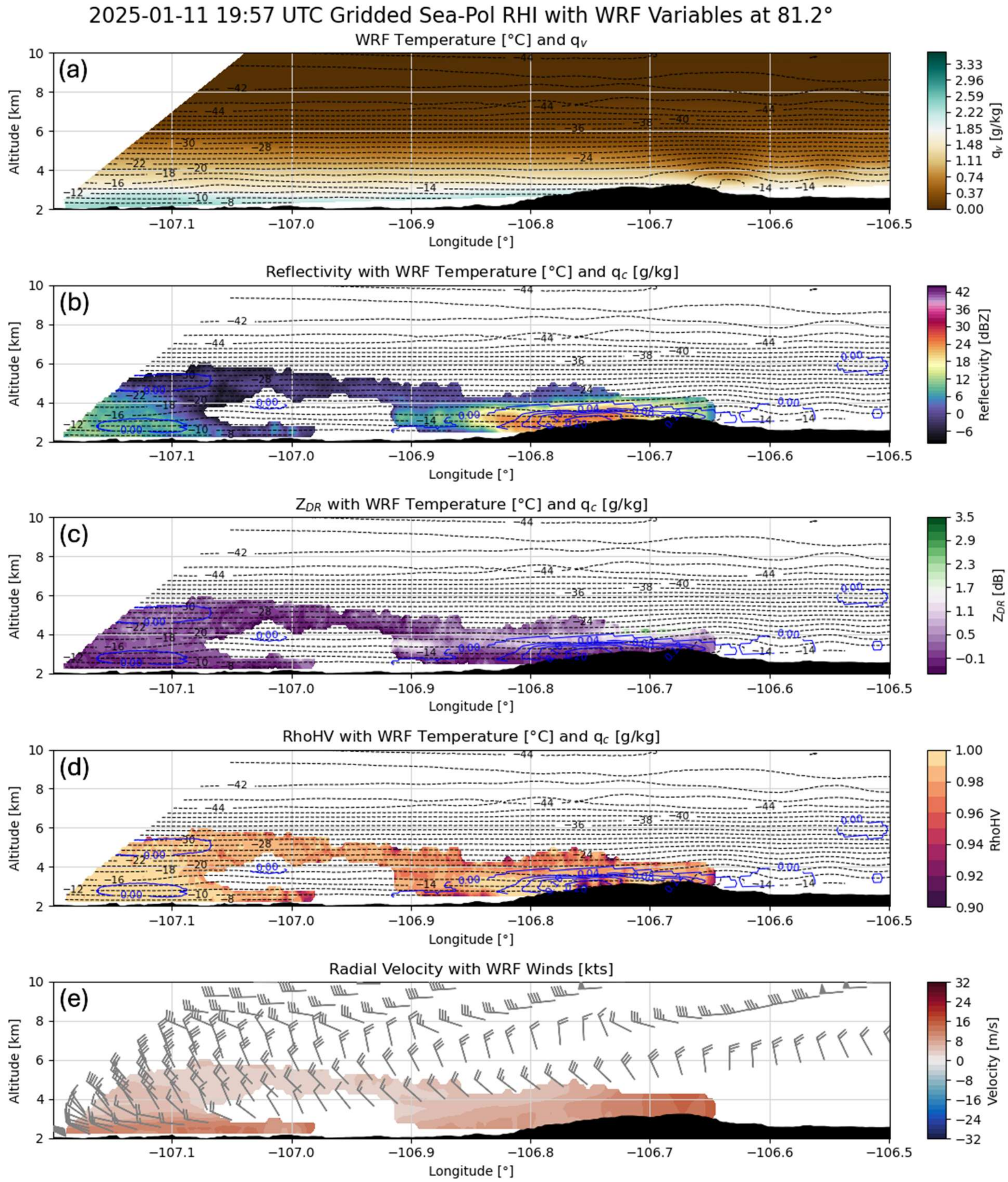

Figure 4.8: As in Figure 4.5, but for 1957 UTC 11 January 2025 and an 81.2° RHI scan.

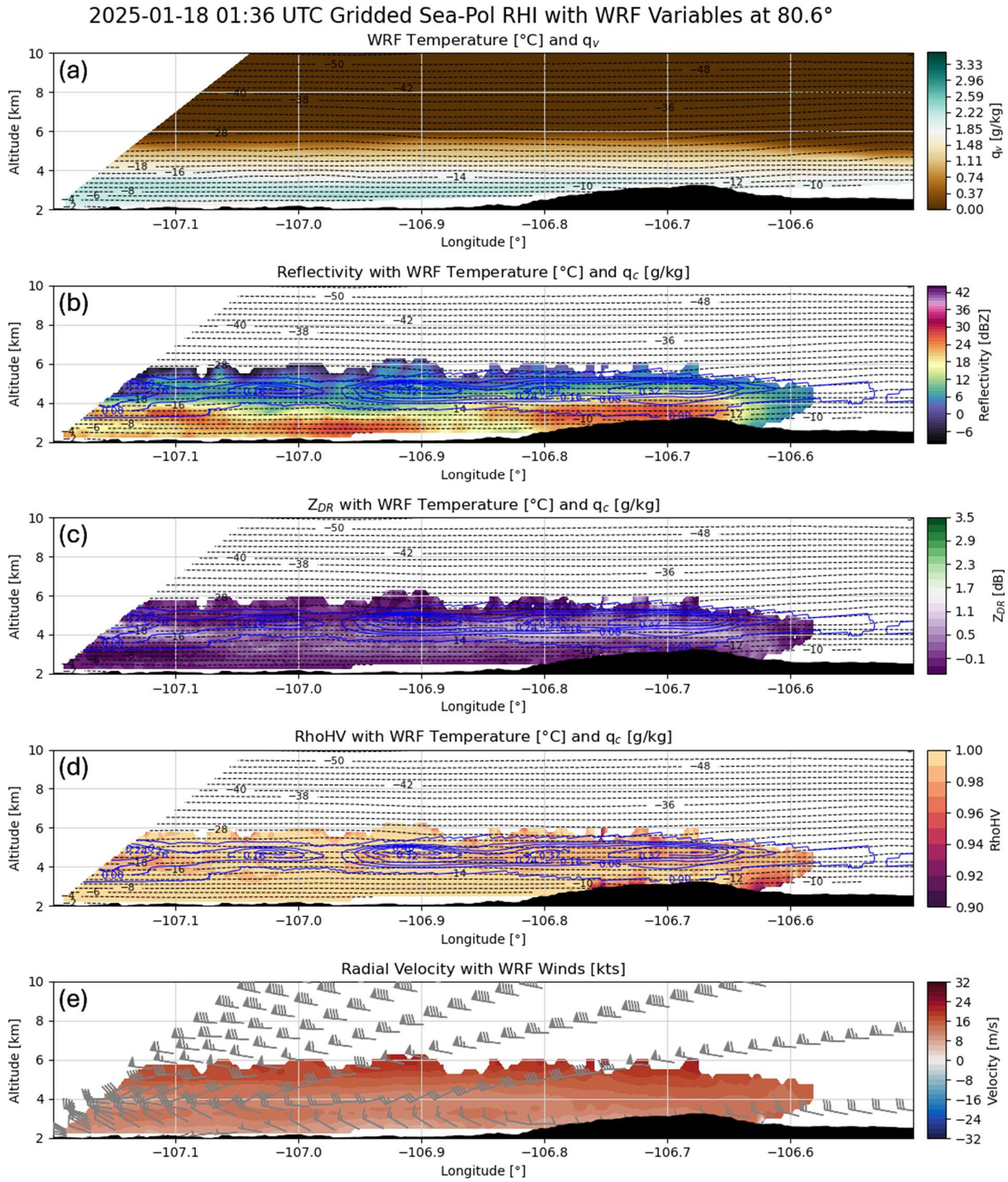

Figure 4.9: As in Figure 4.5, but for 0136 UTC 18 January 2025 and an 80.6° RHI scan.

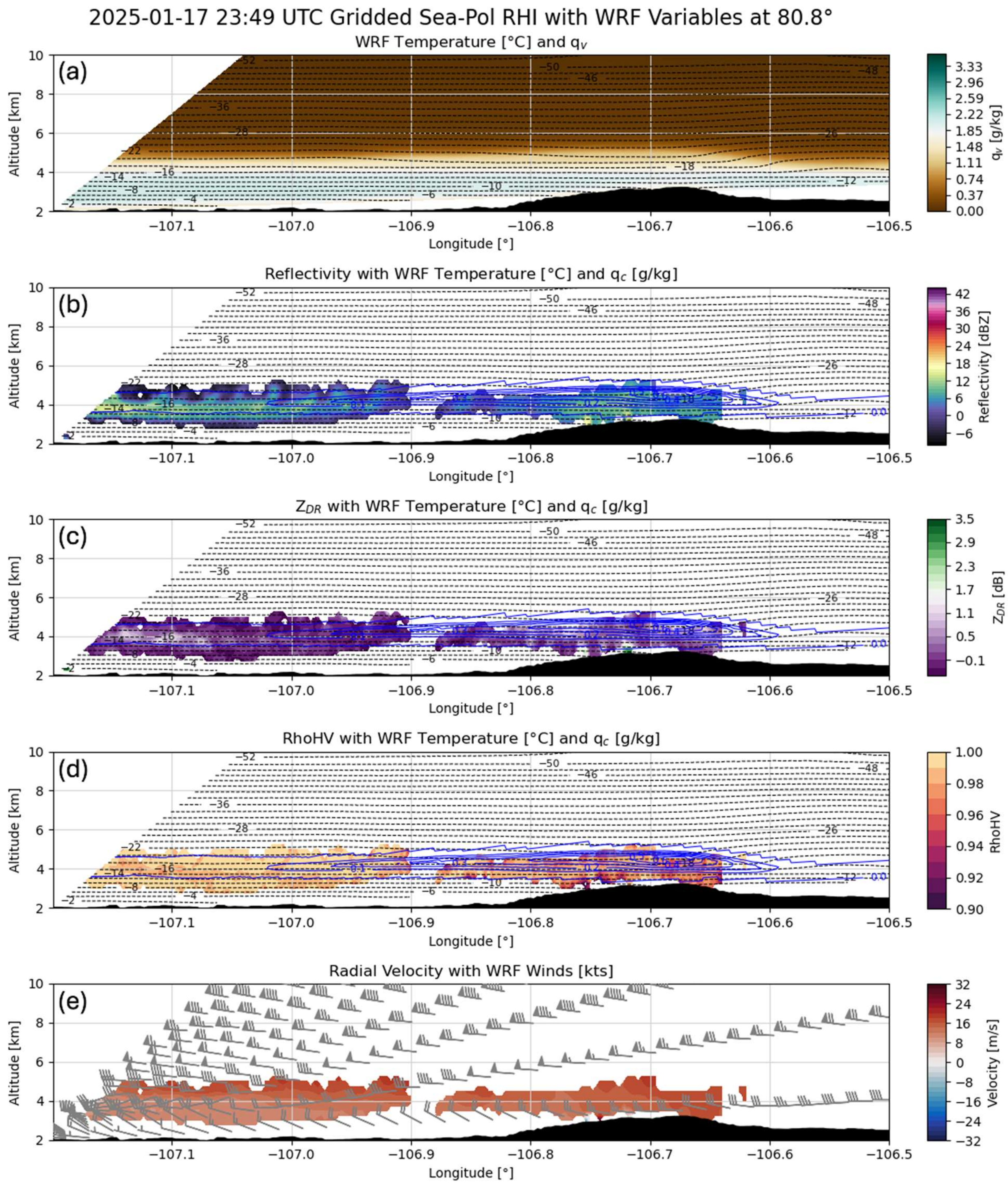

Figure 4.10: As in Figure 4.5, but for 2349 UTC 17 January 2025 and an 80.8° RHI scan.

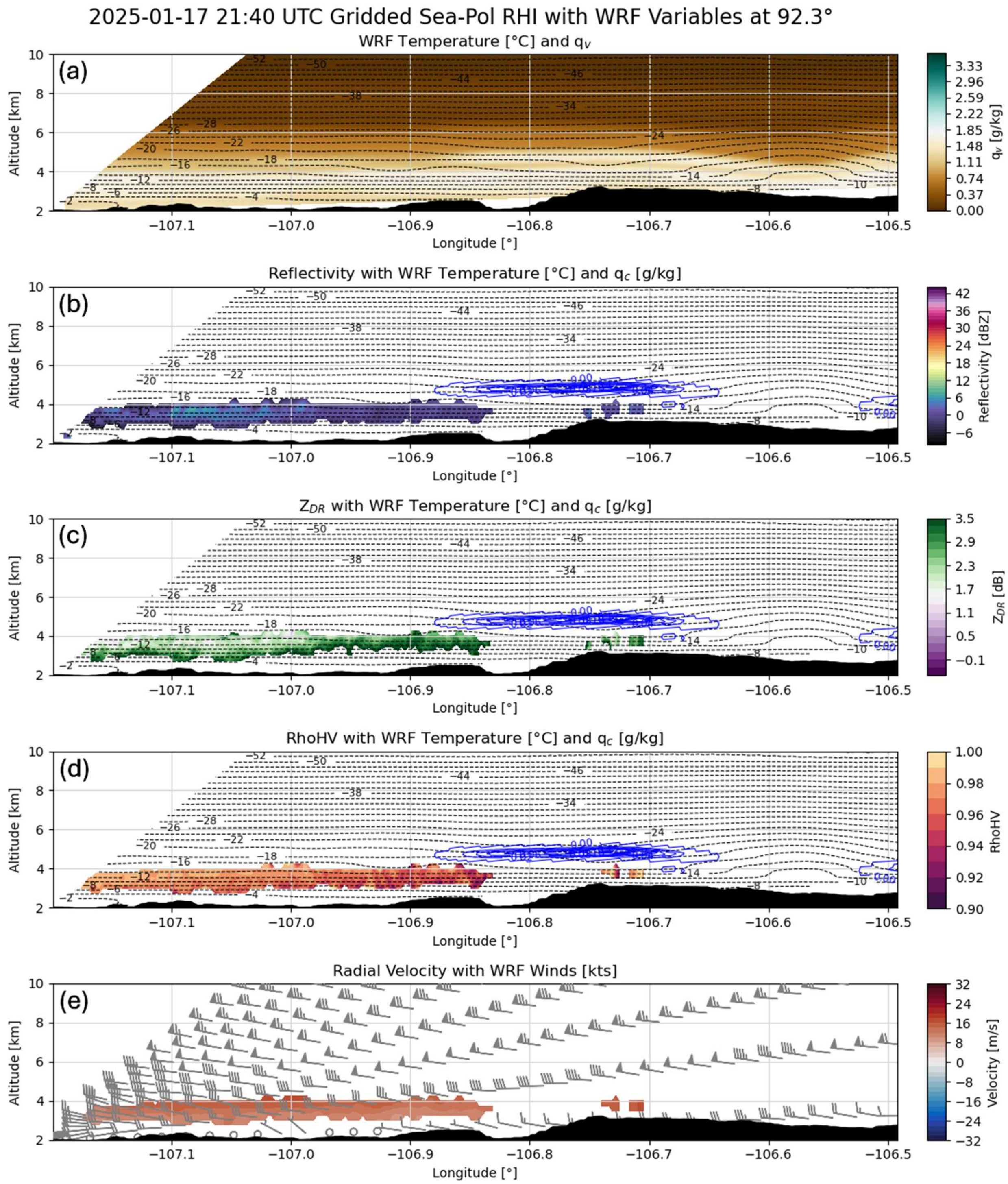

Figure 4.11: As in Figure 4.5, but for 2140 UTC 17 January 2025 and a 92.3° RHI scan.

Chapter 5

Discussion

During the S^2noCliME field campaign, two snowfall events associated with different local wind patterns and magnitudes of moisture transport were observed. IOP3 was associated with the passage of an upper-level shortwave and moderate IVT that was often north-westerly oriented. On the local scale, IOP3 was associated with multiple peaks in on-mountain liquid water and water vapor, most commonly during periods of north-westerly flow at SPL, as well as substantial snow accumulations both on mountain summits around SPL and at low elevations near Steamboat Springs. IOP4 was associated with weaker large-scale forcing, and substantially less, consistently westerly, IVT compared to IOP3. Locally, IOP4 was associated with peaks in on-mountain liquid water and water vapor, where the greatest relative peaks were associated with westerly flow at SPL, as well as less substantial snow accumulations that were concentrated on summits near and south of SPL. Despite these greater differences, considerable variability in snowfall processes and precipitation intensity were observed within the IOPs and for a given local flow regime.

While overall more IVT led to more overall snowfall in IOP3 than IOP4, the considerable variability within IOPs and for specific flow regimes across IOPs revealed in this analysis emphasize a more nuanced relationship between moisture and snow growth processes. A variety of distinct precipitation patterns were observed throughout IOP3 and IOP4, some of which appear to correspond to shifts in local moisture availability, flow direction, and wind speeds (Fig. 5.1; Fig. 5.2). For example, the transient feature of enhanced Z_{DR} at cloud top located within temperatures around -15 °C with inferred snow growth by aggregation beneath, noted in Figure 4.7, is associated with a substantial local increase in moisture during north-westerly flow at mountain top (Fig. 5.1c) with a corresponding increase in wind speeds from 11 to 17 kts (Fig. 5.1e). A large amount of available moisture could enhance the growth of complicated pristine crystals, such as dendrites, which is maximized around -15 °C and associated with highly positive Z_{DR} like that noted at cloud top in Figure 4.7 (e.g., Straka et al. 2000). As inferred in this analysis, the enhanced growth of dendrites has been observed to result in enhanced aggregation beneath (Karrer et al. 2020; Schrom et al. 2015). Furthermore, the noted signature could be indicative of enhanced stratiform precipitation resulting from weak upward motion that is noted to occur during times of strong, upslope flow unblocked by terrain (Schrom et al. 2015), which aligns with the strengthening north-westerly winds that are cross-barrier to the terrain near SPL, where the RHI scan depicted in Figure 4.7 is towards (Fig. 2.1). In addition, isolated very pristine clouds were observed during north-westerly flow at angles facing SPL in IOP4 (e.g., Fig. 4.11), which supports previous observations that pristine crystals with Z_{DR} values near or above 3.5 dB are associated with low-level upslope flow (e.g., Schrom et al. 2015).

Inferences of riming were possible through local observed integrated liquid water measurements and liquid water mass from WRF. In IOP3, early in the event, moments of enhanced reflectivity indicating potential riming near terrain (e.g., Fig. 4.5) are associated with low local moisture availability (Fig. 5.1c). Later in the event, similar inferences of riming (e.g., Fig. 4.8) are associated with a range of magnitudes of local moisture availability (Fig. 5.1c) but occur most consistently during northwesterly flow before 0300 UTC 12 January 2025 (Fig. 5.1a). In IOP4, however, the pattern of enhanced reflectivity near terrain, such as noted in Fig. 4.9, does not appear to be associated with a notable shift in local moisture availability or flow (Fig. 5.2), indicating the lack of a clear relationship between flow, local moisture content, and riming inferences.

A source of SLW generation and subsequent riming signatures observed during both IOPs are generating cells. In IOP3, the onset of generating cells, like those noted in Figure 4.6, are associated with a shift to westerly flow (Fig. 5.1d), an increase in wind speed at SPL (Fig. 5.1e), and a moderate relative peak in liquid water and water vapor (Fig. 5.1c). In IOP4, generating cells were noted to be associated with conditionally unstable conditions (Fig. 3.8), which supports previous observations of these features during winter precipitation in mountainous environments (e.g., Kumjian et al. 2014, Tessendorf et al. 2024). Generating cells in IOP4, such as those noted in Fig. 4.10, appear to be more associated with changes in local wind speed than local wind direction (Fig. 5.2d, e). The tilt of generating cells in IOP4 where there is a prominent shear layer (4.10), and lack of tilt visible in the IOP3 example (4.6), also support the hypothesis that windshear is a factor in the formation of some (tilted) generating cells, but not others (Kumjian et al. 2014). Furthermore, generating cells have been noted to be a source of precipitation production (e.g., Tessendorf et al. 2024, Zaremba et al. 2025), which could explain subsequent depth of precipitating cloud and intensity of precipitation in IOP4 depicted in Figure 4.9. However, there may be a timing offset in the occurrence of generating cells and surface precipitation associated with them, and quantifying their direct impacts on precipitation is challenging. S^{2}noCliME presents a unique opportunity as an expansive dataset to explore the characteristics of generating cells, the conditions under which they occur, and their connection to snowfall.

What is clear from this analysis is that large-scale moisture availability and large-scale and local wind patterns do not directly result in the same precipitation patterns and microphysical characteristics. The discrepancies between the extent by which changes in local flow impact precipitation patterns (e.g., Fig. 5.1 versus Fig. 5.2) or characteristics (Fig. 4.2) between IOP3 and IOP4 could be connected to greater differences in the environments of the two IOPs – potentially including the noted conditional instability in IOP4 (Fig. 3.8) and the less substantial shifts in local wind direction (Fig. 5.2d). It is hypothesized that the common neutral, or slightly conditionally unstable, conditions during IOP4 may have contributed to the relatively constant presence of enhanced precipitation near terrain as suggested by McMurdie et al. (2018). Orographically-modified snow growth enhanced by atmospheric instability could partially explain why the most consistent maximum reflectivity values across all studied SEA-POL RHI angles in both IOPs, as seen in Figure 5.1a and Figure

5.2a, do not appear to correspond to notable shifts in local moisture availability, wind speed, or direction.

To initially explore this orographic influence on inferred processes, the 2D histograms of reflectivity and Z_{DR} from Section 3 are further subdivided into low and high elevation groups within each flow regime. The high elevation group is defined as all points along an RHI past the first point from the radar that is associated with an elevation of a certain height; the low elevation group encompasses all points along the RHI from the radar up until the first point in which the elevation threshold is reached. SRTM elevation data is utilized for this purpose, with an elevation threshold of 2670 m chosen to fully encompass the separation between the valley and the main terrain barrier, as depicted in Figure 2.1. Figure 5.3 shows the results of this subdivision for north-westerly and westerly flow in both IOPs and depicts reflectivity values > 5 dBZ reaching greater depths closer to the terrain, as well as greater Z_{DR} above 4 to 4.5 km AMSL closer to the terrain for both IOPs and flow regimes. Near-0 dB and slightly negative Z_{DR} values from 3 to 4.5 km AMSL are also most frequent near the terrain barrier (Fig. 5.3), which could indicate a greater frequency of riming over the terrain. These results are fairly consistent regardless of IOP or flow regime, although north-westerly flow does appear to vary more above 4 km AMSL (Fig. 5.3).

Overall, orographically-enhanced precipitation with riming occurred during both IOPs and within a variety of moisture conditions and flow regimes. It was noted that enhancements in IOP3 seem to be more prominent during north-westerly flow at SPL, and that enhancements in IOP4 are less tied to a flow regime, but may be connected to the consistently strong winds, as measured at SPL, and the noted conditionally unstable conditions. In both IOPs, orographic enhancements were observed when water vapor was concentrated in low altitudes below the terrain barrier. Regardless of IOP or flow regime, precipitation over the local terrain barrier was noted to be consistently strong, with a greater depth of high reflectivity values (near and greater than 10 dBZ) and elevated positive Z_{DR}, compared to what was observed at lower elevations nearby. Overall, though, a more thorough investigation of orographic influences warrants comparison against westward RHIs over the valley and further analysis of the model output to consider mechanisms supporting the potential localized orographic enhancement in context of winds and stability.

In addition to the link between terrain and environmental conditions, of continued interest for precipitation enhancement are specific observed precipitation patterns. One such pattern is the seeder-feeder mechanism. Seeder-feeder mechanisms may be present throughout the two cases, particularly at angles facing down-valley (e.g., Fig. 4.5, 5.3) as well as during lingering precipitation in northwesterly flow (e.g., Fig. 5.3). Such as noted in Ramelli et al. (2021) and Lowenthal et al. (2011), this mechanism can enhance riming over a local terrain barrier, but in IOP3, inferred seeder-feeder was also associated with enhanced pristine signatures aloft over terrain. While not exactly associated with a defined flow regime, seeder-feeder clouds similar to those observed in IOP3 (e.g., Fig. 4.5) were a feature of IOP4 (Fig. 5.5). As evident in Figure 5.5, strips of fast-moving cloud with maximum reflectivity values of around 6 to 15 dBZ and associated with relatively low Z_{DR} magnitudes, around 0.5

dB, are located at about 4 km AMSL. Below 4 km AMSL, near the local terrain barrier, reflectivity reaches greater values, up to 20 dBZ, below enhanced Z_{DR} near 0.7 dB and in the presence of SLW as indicated in the WRF output (Fig. 5.5). The cloud with enhanced reflectivity near terrain is also slow-moving and associated with relatively low ρ_{HV} (Fig 5.5d, e). Like in the IOP3 example (Fig. 4.5), this pattern is associated with q_v concentrated at low levels, below the top of the terrain barrier, and in temperatures warmer than -14 °C (Fig. 5.5a).

All precipitation patterns observed during IOP3 (Fig. 5.1a, c) and IOP4 (Fig. 5.2a, c), regardless of whether they were associated with precipitation enhancement over the terrain, are of interest to better understand mechanisms supporting snowfall in this region. It would be worthwhile to further explore methods of quantifying these patterns to assess their frequency of occurrence and associated microphysical imprints throughout the S^{2}noCliME campaign, including in the context of environmental conditions such as flow regime. While many of these patterns were observed in the studied westerly and north-westerly flow regimes, similarly distinct patterns were also noted during periods of south-westerly flow during IOP3 (Fig. 5.1a, c). These patterns include widespread patterns (e.g., sheared convection) and those tied to terrain. IOP3 south-westerly flow is also associated with substantial moisture towards the beginning of the event, and relative peaks in moisture observed towards the end past 0300 UTC 12 January 2025 (Fig. 5.1c).

Because of the flow regime's potential link to moisture availability and specific precipitation patterns, it was of interest to explore whether the relationships between inferred reflectivity and Z_{DR} patterns differ during south-westerly flow from that in westerly or north-westerly flow for IOP3, noting this south-westerly flow regime was infrequent during IOP4. Ultimately, reflectivity and Z_{DR} distributions for south-westerly flow in IOP3 (Fig. 5.4) did suggest different snowfall characteristics than that during westerly and north-westerly flow. For one, there are high Z_{DR} values, reaching up to 3 dB, at temperatures warmer than -12 °C, corresponding to reflectivity values largely below 10 dBZ, which suggests some frequency of small, pristine crystals reaching the ground (Fig. 5.4b) not observed during the other flow regimes in either IOP. Furthermore, there is minimal change in reflectivity, and thus snow growth, between 4 and 5 km AMSL (Fig. 5.4a) and -15 to -24 °C (Fig. 5.4b), which is unique to this regime.

While south-westerly flow was not the most common regime in either IOP3 or IOP4, and is not the dominant wind direction observed at SPL in general, it is not infrequent (Hallar et al. 2025). *South-westerly* winds, as defined in this analysis, may contribute to around 18% of the winds observed at SPL year-round (Hallar et al. 2025). Although the frequency of south-westerly winds at SPL could be impacted by terrain blocking of large-scale south-westerly flow due to the Flat Top mountain range located south-west of the lab (Lowenthal et al. 2019), the regime is worth exploring in other S^{2}noCliME IOPs.

5.1 Figures

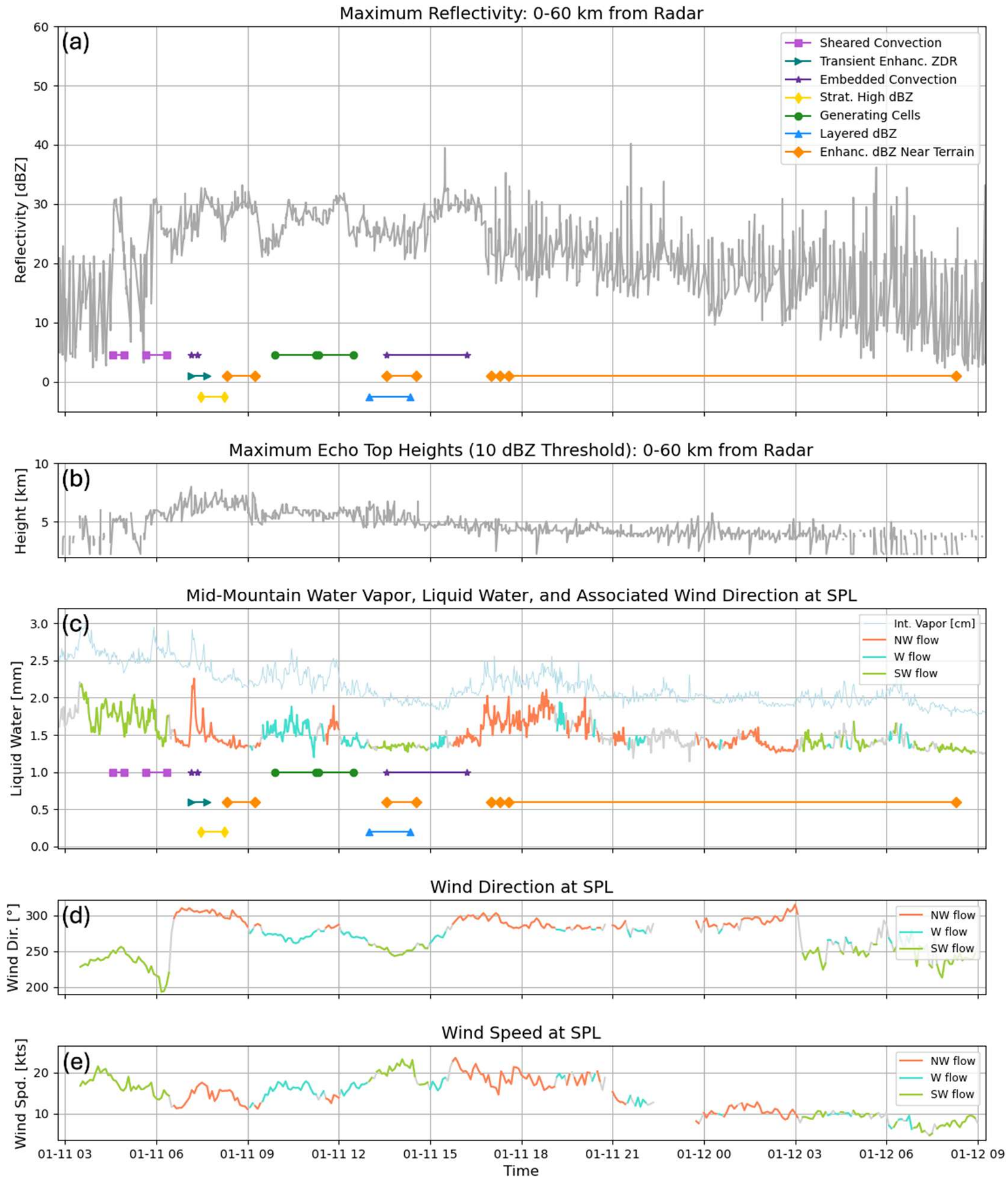

Figure 5.1: Time series of (a) maximum reflectivity values in dBZ observed in SEA-POL RHIs, (b) echo-top heights in km from SEA-POL RHIs at a 10 dBZ threshold, (c) liquid water path and precipitable water vapor as in Figure 3.8, (d) wind direction observed at SPL, and (e) wind speeds in kts observed at SPL for 0330 UTC 11 January 2025 through 0900 UTC 12 January 2025. Colored horizontal lines on panels (a) and (c) indicate time ranges of notable precipitation patterns. Colors overlaid on gray lines in (c), (d), and (e) indicate time ranges corresponding to *north-westerly*, *westerly*, and *south-westerly* winds at SPL as defined in Section 2.3.1.

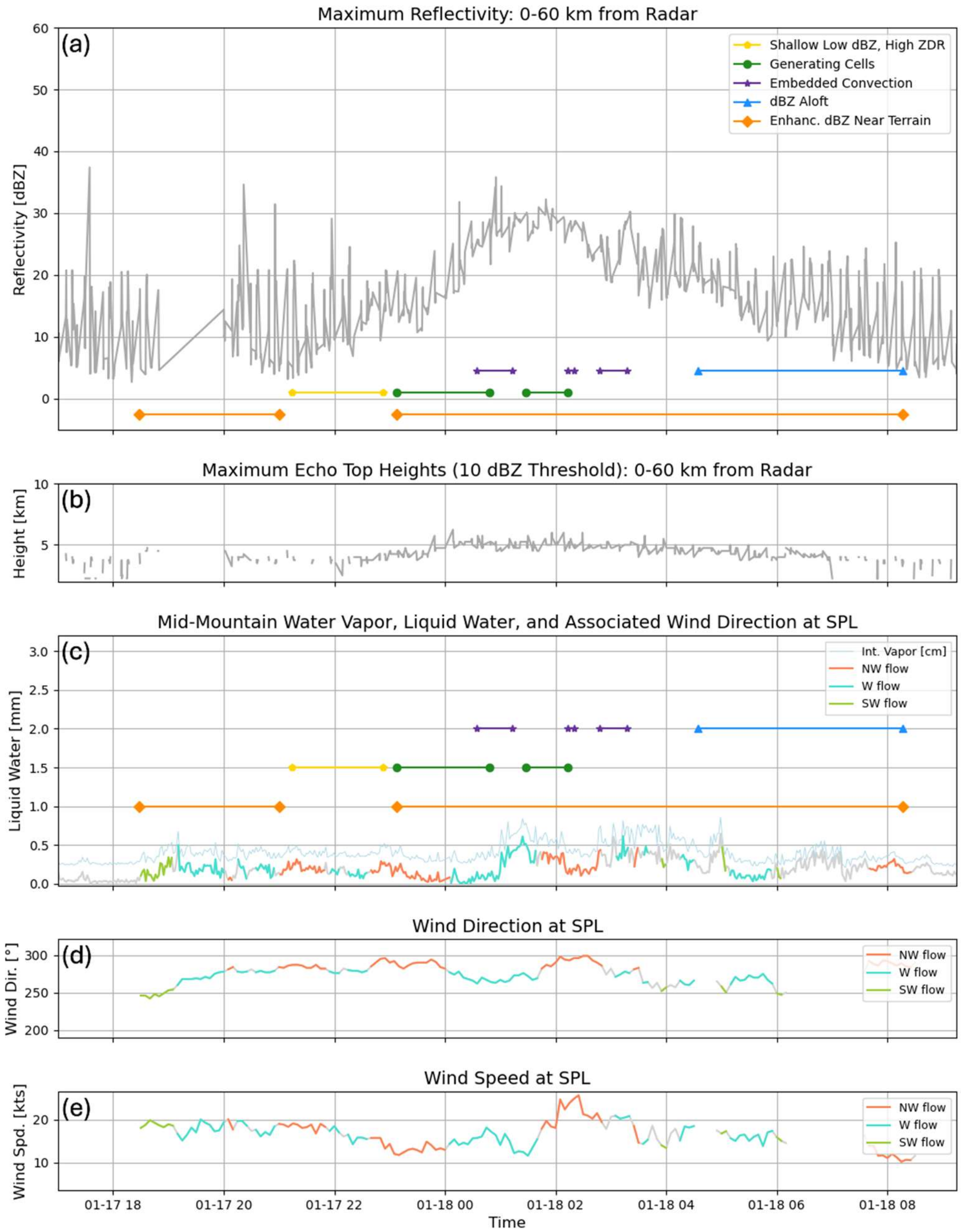

Figure 5.2: As in Figure 5.1 but for 1830 UTC 17 January 2025 through 0830 UTC 18 January 2025.

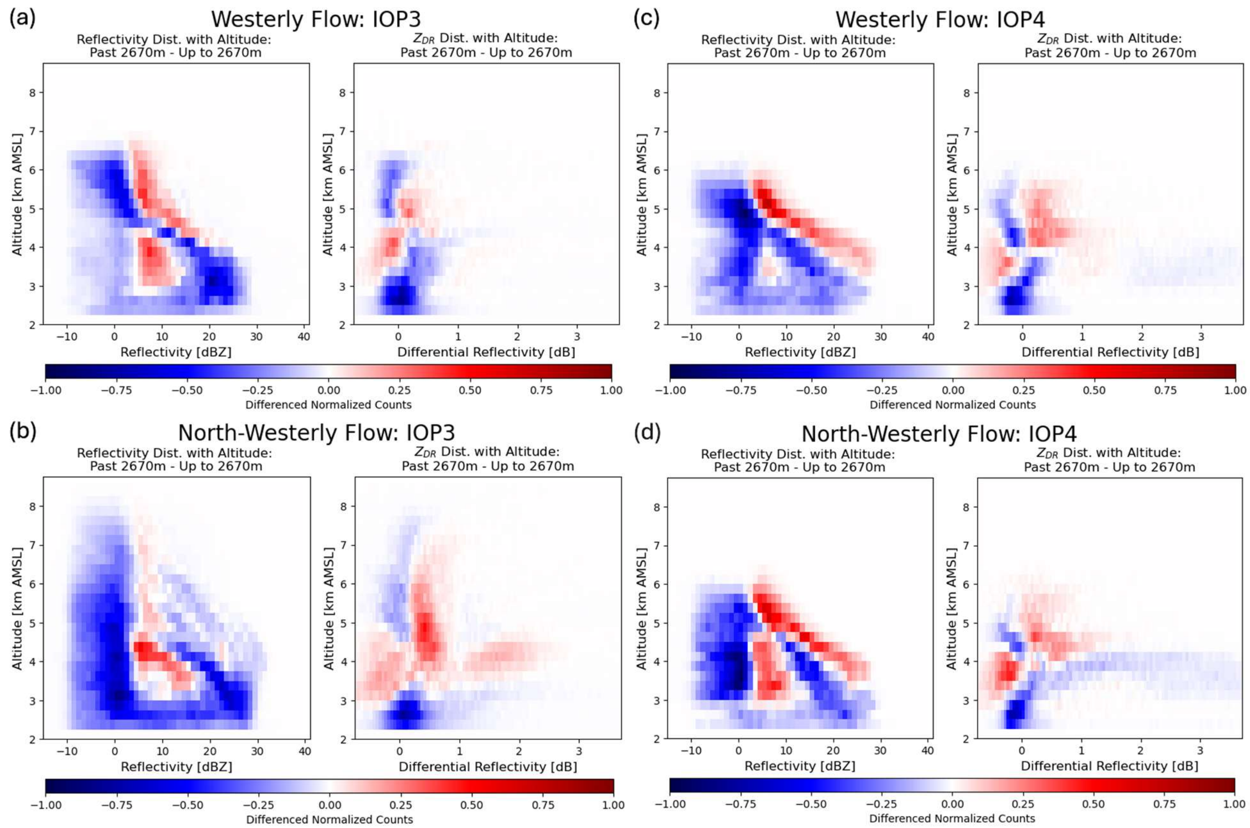

Figure 5.3: 2D histograms depicting the difference in the normalized distribution of reflectivity in dBZ (left columns) and Z_{DR} in dB (right columns) with altitude in km AMSL from SEA-POL 60-120° RHIs between data associated with elevations past 2670 m and data associated with elevations before the altitude of 2670 m is first reached, during time ranges corresponding to *westerly* flow at SPL in (a) IOP3 and (c) IOP4, and during time ranges corresponding to *north-westerly* flow at SPL in (b) IOP3 and (d) IOP4, as the flow regimes are defined in Section 2.3.1. Red coloring indicates greater normalized counts past 2670 m; blue coloring indicates greater normalized counts up to 2670 m.

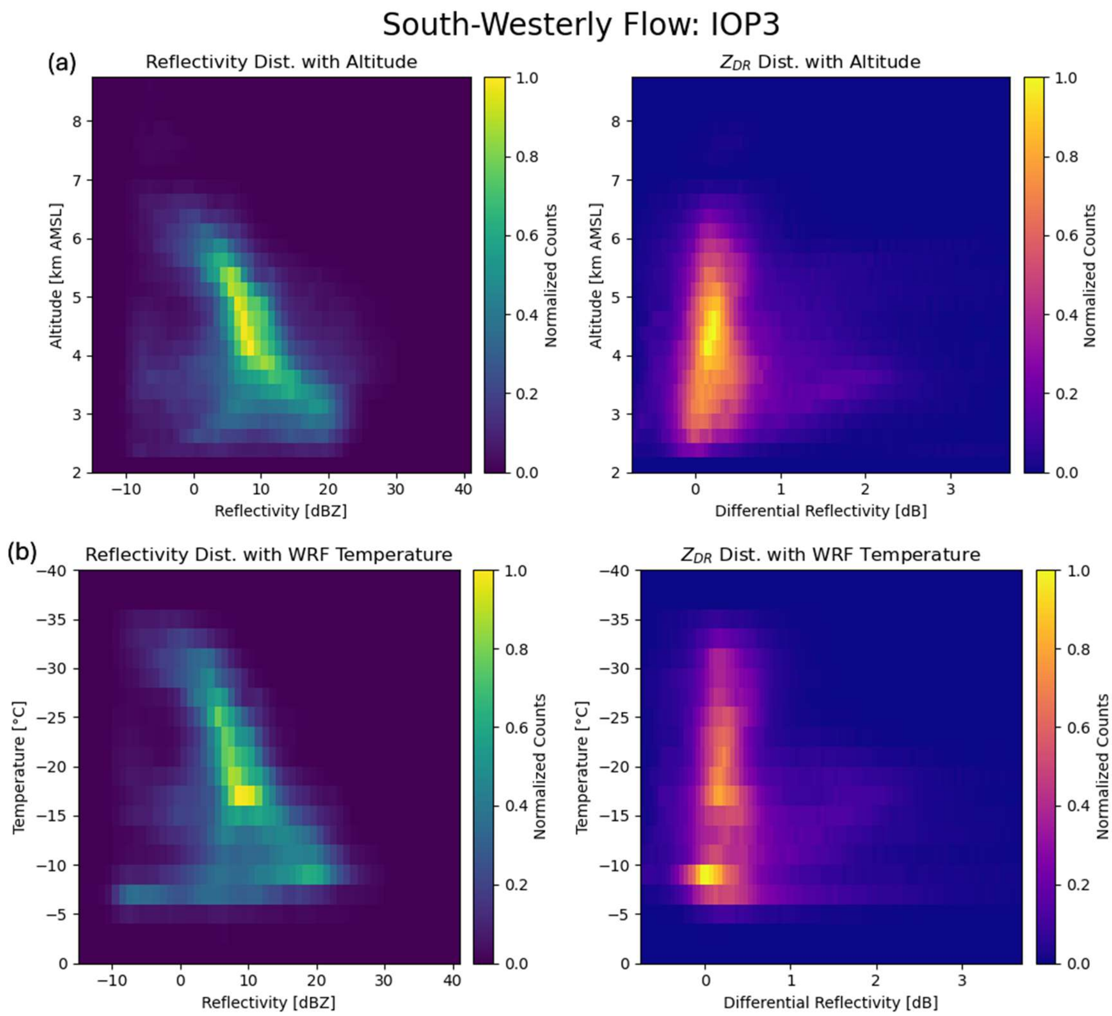

Figure 5.4: 2D histograms of reflectivity in dBZ (left columns) and Z_{DR} in dB (right columns) with (a) altitude in km AMSL and (b) temperature in °C from WRF for SEA-POL 60-120° RHIs during time ranges corresponding to *south-westerly* flow in IOP3 as the flow regime is defined in Section 2.3.1. Histograms are normalized by maximum count in any bin.

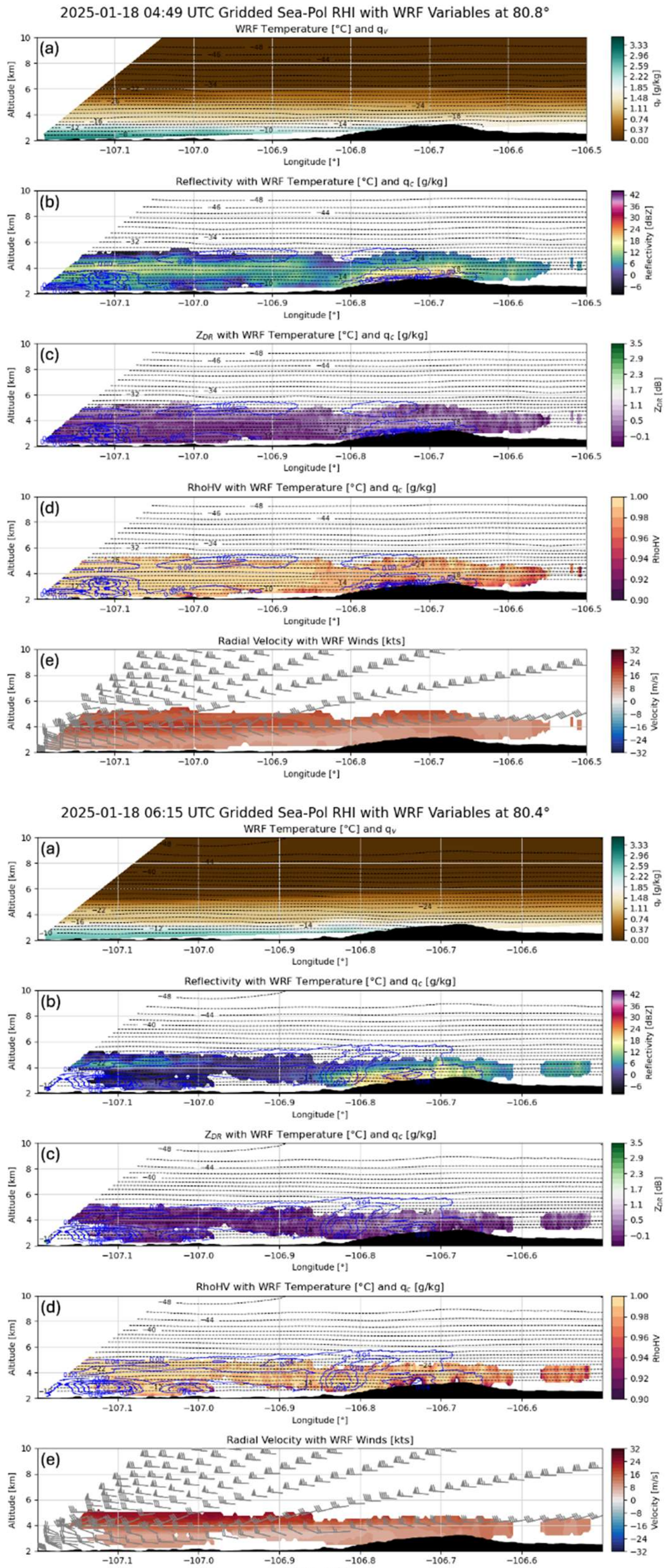

Figure 5.5: As in Figure 4.5, but for 0449 UTC 18 January 2025 at an 80.8° azimuth (top) and 0615 UTC 18 January 2025 at an 80.4° azimuth (bottom).

Chapter 6

Summary and Future Work

6.1 Summary

The goal of this analysis was to use the unique observations collected during the S^{2}noCliME campaign to investigate how the local transport, magnitude, and distribution of moisture lead to different snowfall characteristics. Within this goal, attention was focused on the extent by which the total magnitude of moisture and integrated moisture transport (IVT) determined snow characteristics during two S^{2}noCliME IOPs with differing large-scale moisture patterns: IOP3 and IOP4, where IOP3 was associated with greater and more north-westerly oriented IVT than IOP4. Through analyzing coincident data from a dual-polarization radar, a microwave radiometer, winds from a mountain-top surface station, rawinsondes, and a high-resolution model, it was found that:

1. The primary direction of IVT for each IOP roughly translated to peaks in on-mountain moisture associated with corresponding wind direction at SPL, suggesting that IVT magnitude and direction did correspond to local moisture availability.
2. Precipitating cloud depths reached higher maximum and average altitudes during IOP3, suggesting that the magnitude of large-scale moisture transport

had some influence on the vertical extent of precipitating clouds and thus observed snowfall.

3. Periods of similarly large reflectivity values were observed with both IOPs, along with substantial variety in inferred patterns of snow growth, suggesting that IVT does not exhibit complete control on local precipitation characteristics.

The implications of subtle variations in the direction of local flow were also a point of focus for this analysis, finding that:

1. Precipitating cloud depth was similar across westerly and north-westerly flow in IOP4, reaching slightly higher maximum depth during north-westerly flow, despite the westerly-oriented IVT and presence of greater local moisture availability during westerly flow. This result suggests that flow direction might be a factor in snowfall independent of the total magnitude of moisture or moisture transport.
2. Dominant snow processes and characteristics differed between north-westerly and westerly flow in both IOPs, suggesting the direction of local flow was influencing snow growth processes. However, the changes in characteristics between flow regimes were not the same for both IOPs, further suggesting that dominant snow and snowfall characteristics are sensitive to the moisture (total magnitude and distribution relative to temperature or terrain) and larger-scale conditions (forcings, instability) associated with each individual IOP.

3. Greater variation in snow characteristics was observed near the top of terrain (around 3 km AMSL), and through approximately 2 km above, during northwesterly flow in both IOPs. Some of this variation was connected to spatial variability in inferred snow characteristics that were a manifestation of terrain enhancement or terrain-modified snow-growth processes.
4. Regardless of flow regime, notably enhanced precipitation near terrain associated with riming was most observed when water vapor was concentrated in temperatures warmer than -14 °C at altitudes below 3 km AMSL. Widespread aggregation was associated with more evenly distributed water vapor from the surface through -16 to -18 °C, generally reaching altitudes above 3 km AMSL. The most intense precipitation resulting from either aggregation or riming was located below a region of enhanced depositional growth, but which occurred at colder temperatures (e.g., < -16 °C) during instances of enhanced precipitation through riming over terrain.

Ultimately, vapor deposition, aggregation, and riming were all observed during IOP3 and IOP4. A large variety of patterns of occurrence of these processes were seen throughout the IOPs, some of which were tied to moisture distribution and subtleties in local flow direction. However, consideration of other variables such as instability and wind speed was found to be necessary. In particular, it was found that wind speed could hold influence over snow growth in the region, and that snow growth over terrain differed similarly from that at lower elevations regardless of the wind direction. Limitations remain in the breadth of observations and extent of datasets used in this analysis, particularly in the lack of verification to combined radar and model inferences. Further exploration into specific patterns of snow growth processes, and different methods of SLW generation to support riming, would be better explored through incorporating data from other IOPs (including those with in-situ measurements not available during the analyzed times), incorporating other S^{2}noCliME datasets, and extending usage of the WRF model.

6.2 Avenues for Future Work

The analysis presented emphasizes the importance of considering the influence of local flow as well as the local distribution of moisture when assessing snowfall variability in S^{2}noCliME cases. The results also emphasize the importance of fully understanding snow growth at low levels to accurately predict the amount, and water content, of snowfall that accumulates in a mountainous environment, along with the subtle variations in environmental flow and moisture tied to this snow growth. These subtle variations, within IOPs and within local flow regimes, set the stage for further analysis across the 20 additional IOPs observed during S^{2}noCliME. Through incorporating analysis of additional IOPs, the frequency of occurrence of distinct precipitation patterns, their microphysical inferences, and their relationship to local environmental parameters can be explored, including understanding the links to southwesterly flow, conditional instability, and shifts in wind speed, which were underexplored in this study owing to their relative infrequency in observations.

Additionally, motivated by the need to diminish ambiguity in riming and aggregation signatures, other SEA-POL radar variables, such as K_{DP}, could be used with upcoming versions of the dataset to reduce ambiguity, as well as incorporating fall speed estimates from the vertically-pointing MRRs in combination with data from KASPR (e.g., Figure 1.4, Oue et al. 2021). Importantly, while the SPL probe data was unavailable for IOP3 and IOP4 for quantitative assessments during times of precipitation, the CIP and PIP will be invaluable for later IOPs in connecting to radar-inferred microphysical processes and distinguishing ambiguities. Furthermore, exploring the differences in orographic enhancement within flow regimes between angles of SEA-POL RHIs, in these cases and beyond, could assess the sensitivity of subtle variations in terrain geometry to the direction of incoming flow. While these observations are valuable, the WRF model can also be further validated and used to separate out specific processes inferred from the measurements. Specifically, orographic influences may continue to be investigated using the WRF model to carry out terrain-sensitivity experiments or additional study of the time evolution of vertical motion across the IOPs. Ultimately, the work initiated by this comparison between IOP3 and IOP4 sets the stage for further analysis of S^{2}noCliME data, including understanding variations in and controls on snow growth processes – all of which hold considerable influence over snowpack SWE and water availability in surrounding communities.

Bibliography

Bailey, M., and J. Hallett, 2004: Growth Rates and Habits of Ice Crystals between −20° and −70°C. *J. Atmos. Sci.*, **61**, 514–544, DOI: 10.1175/1520-0469(2004)061 <0514:GRAHOI>2.0.CO;2.

Barros, A. P., 2013: Orographic Precipitation, Freshwater Resources, and Climate Vulnerabilities in Mountainous Regions. *Climate Vulnerability*, Elsevier, 57–78, DOI: 10.1016/B978-0-12-384703-4.00504-9.

Bergeron, T., 1935: On the physics of clouds and precipitation. *Proces Verbaux de l'Association de Météorologie,* International Union of Geodesy and Geophysics, 156–178.

Borys, R. D., and M. A. Wetzel, 1997: Storm Peak Laboratory: A Research, Teaching, and Service Facility for the Atmospheric Sciences. *Bull. Amer. Meteor. Soc.*, **78**, 2115–2123, DOI: 10.1175/15200477(1997)078%253C2115:SPLART%2 53E2.0.CO;2.

Borys, R. D., D. H. Lowenthal, S. A. Cohn, and W. O. J. Brown, 2003: Mountaintop and radar measurements of anthropogenic aerosol effects on snow growth and snowfall rate. *Geophysical Research Letters*, **30**, DOI: 10.1029/2002GL0 16855.

Brandes, E. A., K. Ikeda, G. Thompson, and M. Schönhuber, 2008: Aggregate Terminal Velocity/Temperature Relations. *Journal of Applied Meteorology and Climatology*, **47**, 2729–2736, DOI: 10.1175/2008JAMC1869.1.

Bytheway, J. L., W. R. Currier, M. R. Abel, K. Mahoney, and R. Cifelli, 2024: Evaluation of Wintertime Precipitation Estimates and Forecasts in the Mountains of Colorado. *Journal of Hydrometeorology*, **25**, 565–579, DOI: 10.1175/JH M-D-23-0158.1.

Cann, M. D., and A. B. White, 2021: Controls on Wintertime Nonbrightband Rain Rate and Frequency in California's Northern Coast Ranges. *Journal of Hydrometeorology*, DOI: 10.1175/JHM-D-20-0046.1.

Connolly, P. J., C. Emersic, and P. R. Field, 2012: A laboratory investigation into the aggregation efficiency of small ice crystals. *Atmos. Chem. Phys.*, **12**, 2055–2076, DOI: 10.5194/acp-12-2055-2012.

Cordeira, J. M., F. M. Ralph, A. Martin, N. Gaggini, J. R. Spackman, P. J. Neiman, J. J. Rutz, and R. Pierce, 2017: Forecasting Atmospheric Rivers during CalWater 2015. *Bulletin of the American Meteorological Society*, **98**, 449–459, DOI: 10.1175/BAMS-D-15-00245.1.

De Boer, G., and Coauthors, 2023: Supporting Advancement in Weather and Water Prediction in the Upper Colorado River Basin: The SPLASH Campaign. *Bulletin of the American Meteorological Society*, **104**, E1853–E1874, DOI: 10 .1175/BAMS-D-22-0147.1.

DeLaFrance, A., L. McMurdie, and A. Rowe, 2021: Orographically Modified Ice-Phase Precipitation Processes During the Olympic Mountains Experiment (OLYMPEX). *Journal of the Atmospheric Sciences*, DOI: 10.1175/JAS-D-21 0091.1.

Findeisen, W., 1938: Kolloid-meteorologische Vorgänge bei Neiderschlags-bildung.

Meteor. Z., **55**, 121–133.

Feldman, D. R., and Coauthors, 2023: The Surface Atmosphere Integrated Field Laboratory (SAIL) Campaign. *Bulletin of the American Meteorological Society*, **104**, E2192–E2222, DOI: 10.1175/BAMS-D-22-0049.1.

Grasmick, C., B. Geerts, J. R. French, S. Haimov, and R. M. Rauber, 2022: Estimating Microphysics Properties in Ice-Dominated Clouds from Airborne Ka–W-band Dual-Wavelength Ratio Reflectivity Factor in Close Proximity to In Situ Probes. *Journal of Atmospheric and Oceanic Technology*, **39**, 1815–1833, DOI: 10.1175/JTECH-D-21-0147.1.

Hallar, A. G., and Coauthors, 2025: Storm Peak Laboratory: A Research and Training Facility for the Atmospheric Sciences. *Bulletin of the American Meteorological Society*, **106**, E1130–E1148, DOI: 10.1175/BAMS-D-24-0043.1.

Hamlet, A. F., P. W. Mote, M. P. Clark, and D. P. Lettenmaier, 2005: Effects of Temperature and Precipitation Variability on Snowpack Trends in the Western United States*. *Journal of Climate*, **18**, 4545–4561, DOI: 10.1175/JC LI3538.1.

Han, M., S. A. Braun, T. Lang, M. L. W. Mclinden, G. M. Heymsfield, L. Li, and K. L. Thornhill, 2025: Supercooled Liquid Water at the Top of a Snow-Producing Nimbostratus Cloud and Its Association With Gravity Wave Breaking and Turbulence: An IMPACTS Case Study. *JGR Atmospheres*, **130**, DOI: 10.1029/202 4JD0 41795.

Harris, C. R., and Coauthors, 2020: Array programming with NumPy. *Nature*, **585**, 357–362, DOI: 10.1038/s41586-020-2649-2.

Hill, K. M., 2026: Record-low snowpack tests Colorado's recreation economy. *CU Boulder Today*, Accessed 5 June 2026, URL: https://www.colorado.edu/today /2026/03/11/record-low-snowpack-tests-colo rados-recreation-economy.

Houze, R. A., 2012: Orographic effects on precipitating clouds. *Reviews of Geophysics*, **50**, DOI: 10.1029/2011RG000365.

Houze, R. A.Jr., and S. Medina (2005), Turbulence as a mechanism for orographic precipitation enhancement, *J. Atmos. Sci.*, **62**, 3599–3623, DOI: 10.1175/JAS35 55.1.

Hueholt, D. M., S. E. Yuter, and M. A. Miller, 2022: Revisiting Diagrams of Ice Growth Environments. *Bulletin of the American Meteorological Society*, **103**, E2584–E2603, DOI: 10.1175/BAMS-D-21-0271.1.

Hunter, J. D., 2007: Matplotlib: A 2D Graphics Environment. *Comput. Sci. Eng.*, **9**, 90–95, DOI: 10.1109/MCSE.2007.55.

Karrer, M., A. Seifert, C. Siewert, D. Ori, A. Von Lerber, and S. Kneifel, 2020: Ice Particle Properties Inferred From Aggregation Modelling. *J Adv Model Earth Syst*, **12**, DOI: 10.1029/2020MS002066.

Kennedy, P. C., and S. A. Rutledge, 2011: S-Band Dual-Polarization Radar Observations of Winter Storms. *Journal of Applied Meteorology and Climatology*, **50**, 844–858, DOI: 10.1175/2010JAMC2558.1.

Kingsmill, D. E., P. O. G. Persson, S. Haimov, and M. D. Shupe, 2016: Mountain waves and orographic precipitation in a northern Colorado winter storm. *Quart J Royal Meteoro Soc*, **142**, 836–853, DOI: 10.1002/qj.2685.

Kneifel, S., and D. Moisseev, 2020: Long-Term Statistics of Riming in Nonconvective Clouds Derived from Ground-Based Doppler Cloud Radar Observations. *Journal of the Atmospheric Sciences*, **77**, 3495–3508, DOI: 10.1175/JAS-D-20-00 07.1.

Kneifel, S., A. Von Lerber, J. Tiira, D. Moisseev, P. Kollias, and J. Leinonen, 2015: Observed relations between snowfall microphysics and triple-frequency radar measurements. *JGR Atmospheres*, **120**, 6034–6055, DOI: 10.1002/2015JD0231 56.

Korolev, A., 2007: Limitations of the Wegener–Bergeron–Findeisen Mechanism in the Evolution of Mixed-Phase Clouds. *Journal of the Atmospheric Sciences*, **64**, 3372–3375, DOI: 10.1175/JAS4035.1.

Korolev, A., and Coauthors, 2017: Mixed-Phase Clouds: Progress and Challenges. *Meteorological Monographs*, **58**, 5.1-5.50, DOI: 10.1175/AMSMONOGRAP HS-D-17 0001.1.

Kumjian, M. R., S. A. Rutledge, R. M. Rasmussen, P. C. Kennedy, and M. Dixon, 2014: High-Resolution Polarimetric Radar Observations of Snow-Generating Cells. *Journal of Applied Meteorology and Climatology*, **53**, 1636–1658, DOI: 10.1175/J AMC-D-13-0312.1.

Kumjian, M. R., O. P. Prat, K. J. Reimel, M. Van Lier-Walqui, and H. C. Morrison, 2022: Dual-Polarization Radar Fingerprints of Precipitation Physics: A Review. *Remote Sensing*, **14**, 3706, DOI: 10.3390/rs14153706.

Li, D., M. L. Wrzesien, M. Durand, J. Adam, and D. P. Lettenmaier, 2017: How much runoff originates as snow in the western United States, and how will that change in the future? *Geophysical Research Letters*, **44**, 6163–6172, DOI: 10.1002/2017GL073551.

Lowenthal, D., and Coauthors, 2016: Isotopic Fractionation in Wintertime Orographic Clouds. *Journal of Atmospheric and Oceanic Technology*, **33**, 2663–2678, DOI: 10.1175/JTECH-D-15-0233.1.

Lowenthal, D. H., R. D. Borys, W. Cotton, S. Saleeby, S. A. Cohn, and W. O. J. Brown, 2011: The altitude of snow growth by riming and vapor deposition in mixed-phase orographic clouds. *Atmospheric Environment*, **45**, 519–522, DOI: 10.1 016/j.atmosenv.2010.09.061.

Lowenthal, D. H., A. G. Hallar, R. O. David, I. B. McCubbin, R. D. Borys, and G. G. Mace, 2019: Mixed-phase orographic cloud microphysics during StormVEx and IFRACS. *Atmos. Chem. Phys.*, **19**, 5387–5401, DOI: 10.5194/acp-19-5387-2019.

Lundquist, J., M. R. Abel, E. Gutmann, and S. Kapnick, 2019: Our Skill in Modeling Mountain Rain and Snow is Bypassing the Skill of Our Observational Networks. *Bulletin of the American Meteorological Society*, **100**, 2473–2490, DOI: 10.1175/BAMS-D-19-0001.1.

Lundquist, J. D., and Coauthors, 2024: Sublimation of Snow. *Bulletin of the American Meteorological Society*, **105**, E975–E990, DOI: 10.1175/BAMS-D-23-0191.1.

Martinez, G., A. K. Rowe, K. M. Núñez Ocasio, Z. L. Moon, and B. D. Rodenkirch, 2025: Evaluating Environmental Moisture Relative to Tropical Deep Convective Growth Using CPEX-CV Airborne and Satellite Observations. *JGR Atmospheres*, **130**, DOI: 10.1029/2025JD043877.

Mason, S. L., C. J. Chiu, R. J. Hogan, D. Moisseev, and S. Kneifel, 2018: Retrievals of Riming and Snow Density From Vertically Pointing Doppler Radars. *JGR Atmospheres*, **123**, DOI: 10.1029/2018JD028603.

Mastin, M. C., K. J. Chase, and R. W. Dudley, 2011: Changes in Spring Snowpack for Selected Basins in the United States for Different Climate-Change Scenarios. *Earth Interactions*, **15**, 1–18, DOI: 10.1175/2010EI368.1.

Mateling, M. E., C. Pettersen, M. S. Kulie, K. S. Mattingly, S. A. Henderson, and T. S. L'Ecuyer, 2021: The Influence of Atmospheric Rivers on Cold-Season Precipitation in the Upper Great Lakes Region. *JGR Atmospheres*, **126**, DOI: 10.1029 /2021JD034754.

Matrosov, S. Y., M. Maahn, and G. De Boer, 2019: Observational and Modeling Study of Ice Hydrometeor Radar Dual-Wavelength Ratios. *Journal of Applied Meteorology and Climatology*, **58**, 2005–2017, DOI: 10.1175/JAMC-D-19-001 8.1.

Matrosov, S. Y., A. V. Ryzhkov, M. Maahn, and G. De Boer, 2020: Hydrometeor Shape Variability in Snowfall as Retrieved from Polarimetric Radar Measurements. *Journal of Applied Meteorology and Climatology*, **59**, 1503–1517, DOI: 10.1175/J AMC-D-20-0052.1.

May, R. M., and Coauthors, 2022: MetPy: A Meteorological Python Library for Data Analysis and Visualization. *Bulletin of the American Meteorological Society*, **103**, E2273–E2284, DOI: 10.1175/BAMS-D-21-0125.1.

Medina, S., and R. A. Houze Jr. (2003), Air motions and precipitation growth in alpine storms, *Q. J. R. Meteorol. Soc.*, **129**, 345–371, DOI: **10.1256/qj .02.13**.

McMurdie, L. A., A. K. Rowe, R. A. Houze, S. R. Brodzik, J. P. Zagrodnik, and T. M. Schuldt, 2018: Terrain-Enhanced Precipitation Processes Above the Melting Layer: Results From OLYMPEX. *JGR Atmospheres*, **123**, DOI: 10.1029/2018JD029161.

Moisseev, D., A. Von Lerber, and J. Tiira, 2017: Quantifying the effect of riming on snowfall using ground-based observations. *JGR Atmospheres*, **122**, 4019–4037, DOI: 10.1002/2016JD026272.

Moisseev, D. N., S. Lautaportti, J. Tyynela, and S. Lim, 2015: Dual-polarization radar signatures in snowstorms: Role of snowflake aggregation. *JGR Atmospheres*, **120**, 12644–12655, https://doi.org/10.1002/2015JD023884.

Morrison, H., and Coauthors, 2020: Confronting the Challenge of Modeling Cloud and Precipitation Microphysics. *J Adv Model Earth Syst*, **12**, DOI: 10.1029/2019MS001689.

Mote, P. W., A. F. Hamlet, M. P. Clark, and D. P. Lettenmaier, 2005: DECLINING MOUNTAIN SNOWPACK IN WESTERN NORTH AMERICA*. *Bull. Amer. Meteor. Soc.*, **86**, 39–50, DOI: 10.1175/BAMS-86-1-39.

NOAA, 2022: Product Description Document National Gridded Snowfall Analysis. URL: https://www.nohrsc.noaa.gov/technology/pdf/PDD_National_Gridded_Snowfall _ Analysis.pdf

Oue, M., P. Kollias, S. Y. Matrosov, A. Battaglia, and A. V. Ryzhkov, 2021: Analysis of the microphysical properties of snowfall using scanning polarimetric and vertically pointing multi-frequency Doppler radars. *Atmos. Meas. Tech.*, **14**, 4893–4913, DOI: 10.5194/amt-14-4893-2021.

Parthum, B., and P. Christensen, 2022: A market for snow: Modeling winter recreation patterns under current and future climate. *Journal of Environmental Economics and Management*, **113**, 102637, DOI: 10.1016/j.jeem.2022.102 637.

Ramelli, F., and Coauthors, 2021: Microphysical investigation of the seeder and feeder region of an Alpine mixed-phase cloud. *Atmos. Chem. Phys.*, **21**, 6681–6706, DOI: 10.5194/acp-21-6681-2021.

Rudisill, W. J., A. N. Flores, H. P. Marshall, E. Siirila-Woodburn, D. R. Feldman, A. M. Rhoades, Z. Xu, and A. Morales, 2024: Cold-Season Precipitation Sensitivity to Microphysical Parameterizations: Hydrologic Evaluations Leveraging Snow Lidar Datasets. *Journal of Hydrometeorology*, **25**, 143–160, DOI: 10.117 5/JHM-D-22-0217.1.

Rutz, J. J., W. J. Steenburgh, and F. M. Ralph, 2014: Climatological Characteristics of Atmospheric Rivers and Their Inland Penetration over the Western United States. *Monthly Weather Review*, **142**, 905–921, DOI: 10.1175/MWR-D-13-0016 8.1.

Saleeby, S.M., W. R. Cotton, R. D. Borys, D. Lowenthal, and M. A. Wetzel, 2007: Relative impacts of orographic forcing and pollution aersosols on mountain snowfall. Preprints, *12th Conf. on Mesoscale Processes,* Waterville Valley, NH, Amer. Meteor. Soc., 8.5. URL: http://ams.confex.com/ams/pdfpapers/126031.pdf.

Scalzitti, J., C. Strong, and A. Kochanski, 2016: Climate change impact on the roles of temperature and precipitation in western U.S. snowpack variability. *Geophysical Research Letters*, **43**, 5361–5369, DOI: 10.1002/2016GL068798.

Schrom, R. S., and M. R. Kumjian, 2016: Connecting Microphysical Processes in Colorado Winter Storms with Vertical Profiles of Radar Observations. *Journal of Applied Meteorology and Climatology*, **55**, 1771–1787, DOI: 10.1175/JAMC-D-15-0338.1.

Schrom, R. S., M. R. Kumjian, and Y. Lu, 2015: Polarimetric Radar Signatures of Dendritic Growth Zones within Colorado Winter Storms. *Journal of Applied Meteorology and Climatology*, **54**, 2365–2388, DOI: 10.1175/JAMC-D-15-0004.1.

Serreze, M. C., M. P. Clark, R. L. Armstrong, D. A. McGinnis, and R. S. Pulwarty, 1999: Characteristics of the western United States snowpack from snowpack telemetry (SNOTEL) data. *Water Resources Research*, **35**.

Solheim, F., J. R. Godwin, E. R. Westwater, Y. Han, S. J. Keihm, K. Marsh, and R. Ware, 1998: Radiometric profiling of temperature, water vapor and cloud liquid water using various inversion methods. *Radio Science*, **33**, 393–404, DOI: 10.1029/97RS03656.

Steamboat Ski and Resort Corp., 2025: 2025/26 Steamboat Press Kit. URL: https://www.steamboat.com/-/media/steamboat/media-center-folders/dnamictabs/press-kit2526.pdf?rev=38c22b334f434729954b1855dfa005bc&hash=0A55B2E0E27999634D7E0AE095144EB3.

Sterzinger, L. J., and A. L. Igel, 2021: The Effects of Ice Habit on Simulated Orographic Snowfall. *Journal of Hydrometeorology*, DOI: 10.1175/JHM-D-20-0253.1.

Straka, J. M., D. S. Zrnić, and A. V. Ryzhkov, 2000: Bulk Hydrometeor Classification and Quantification Using Polarimetric Radar Data: Synthesis of Relations. *J. Appl. Meteor.*, **39**, 1341–1372, DOI: 10.1175/1520-0450(2000)039%253C1341:BHCAQU%253E2.0.CO;2.

Tessendorf, S. A., and Coauthors, 2024: Characteristics of Generating Cells in Wintertime Orographic Clouds. *Journal of the Atmospheric Sciences*, **81**, 649–673, DOI: 10.1175/JAS-D-23-0029.1.

Thompson, E. J., S. A. Rutledge, B. Dolan, V. Chandrasekar, and B. L. Cheong, 2014: A Dual-Polarization Radar Hydrometeor Classification Algorithm for Winter Precipitation. *Journal of Atmospheric and Oceanic Technology*, **31**, 1457–1481, DOI: 10.1175/JTECH-D-13-00119.1.

Thompson, G., and T. Eidhammer, 2014: A Study of Aerosol Impacts on Clouds and Precipitation Development in a Large Winter Cyclone. *Journal of the Atmospheric Sciences*, **71**, 3636–3658, DOI: 10.1175/JAS-D-13-0305.1.

Von Terzi, L., J. Dias Neto, D. Ori, A. Myagkov, and S. Kneifel, 2022: Ice microphysical processes in the dendritic growth layer: a statistical analysis combining multi-frequency and polarimetric Doppler cloud radar observations. *Atmos. Chem. Phys.*, **22**, 11795–11821, DOI: 10.5194/acp-22-11795-2022.

Wegener, A., 1911: Thermodynamik der Atmosphäre. *Leipzig*, 331 pp.

Zaremba, T. J., R. M. Rauber, L. A. McMurdie, G. M. McFarquhar, J. E. Yorks, C.N.

Helms, and G. M. Heymsfield, 2025: The 3D Structure of a Shallow Generating Cell Driven Snowstorm over the Midwest and Its Microphysical Characteristics Determined Using Particle Aspect Ratio: A Case Study from IMPACTS. *Journal of the Atmospheric Sciences*, **82**, 2581–2609, DOI: 10.1175/JAS-D-25-0029.1.